論文 / 著書情報
Article / Book Information

題目(和文)	静止衛星画像の数値処理による都市域の海風フロント検出
Title(English)	Detection of Sea-breeze Inland Penetration over Coastal Urban Region using Geostationary Satellite Images
著者(和文)	FERDIANSYAH MuhammadRezza
Author(English)	Muhammad Rezza Ferdiansyah
出典(和文)	学位:博士(工学), 学位授与機関:東京工業大学, 報告番号:甲第11494号, 授与年月日:2020年3月26日, 学位の種別:課程博士, 審査員:神田 学,木内 豪,髙木 泰士,中村 恭志,稲垣 厚至
Citation(English)	Degree:Doctor (Engineering), Conferring organization: Tokyo Institute of Technology, Report number:甲第11494号, Conferred date:2020/3/26, Degree Type:Course doctor, Examiner:,,,,
学位種別(和文)	博士論文
Type(English)	Doctoral Thesis

Detection of Sea-breeze Inland Penetration over Coastal Urban Region using Geostationary Satellite Images

静止衛星画像の数値処理による都市域の海風フロント検出

東京工業大学
Tokyo Institute of Technology

A dissertation presented
by
Muhammad Rezza Ferdiansyah
to
The Department of Transdisciplinary Science and Engineering
Global Engineering for Development, Environment, and Society

In partial fulfillment of the requirements
for the degree of
Doctor of Engineering

Tokyo Institute of Technology
Tokyo, Japan
March, 2020

ADVISOR

PROFESSOR MANABU KANDA (神田　学)

CO-ADVISOR

DR. ATSUSHI INAGAKI (稲垣　厚至)

INTERNAL COMMITTEES

PROFESSOR TSUYOSHI KINOUCHI (木内　豪)

DR. HIROSHI TAKAGI (高木　泰士)

DR. TAKASHI NAKAMURA (中村　恭志)

"It is Allah who sends the winds. Then they raise a cloud, then He spreads it as He wishes in the sky, and forms it into fragments, whereat you see the rain issuing from its midst. Then, when He strikes with it whomever of His servants that He wishes, behold, they rejoice"
(Quran 30:48)

A very honour dedication to
My beloved parents Mr. Dede Ahmad Ghazali and Mrs. Rina Nurlaela,
My dearest wife Mrs. Ambiyah Abdullah,
My lovely daughters Ms. Takia Ayaka Ramadhani, Ms. Samia Haruka Rabbani and Ms. Nuraisha Hanahilwia,
and my supportive siblings Mrs. Rieska Oktavia and family, and Mr. Rifki Fuadi and family.

Acknowledgment

Alhamdulillah. First of all, I would like to express my gratitude to Alloh SWT for His kind blessing and guide so I am able to walk in the path and accomplish my doctoral program.

To my first supervisor, Prof. Manabu Kanda, thank you for your endless support, guidance and thrust to me. Your encouragement, to keep believing in myself, provides me such a great power to finish the race. With you I am always motivated to be a responsible problem solver, to come over any difficulties we may find.

To my second supervisor, Dr. Atsushi Inagaki, thank you for the patience for teaching complicated math equations and letting me to participate in a great experience of ground observation.

To Dr. Alvin Varquez and Dr. Meral Yucel, thank you for sharing the ideas that the research is fun.

To Kanda laboratory members, Ishibashi Yoji san, Xiaoqing He, Narita Yuuri san, thank you for your supports especially in my last year. I am glad can be a part of your group work team. Inoue Ryo san, Seki Hinana san, Yokouchi Hiroshi san, Yokoyama Saki san, Do Ngoc Khanh, Zihan Wang, Zuo He, Kiritani Sosuke san, Ito Soichiro san, Tada Kaho san, thank you for sharing the nice moments in laboratory activities and fun time of outdoors.

And thank you to Lab Secretary, Okamoto Yuko san, thank you for your great help during my study in Kanda laboratory.

To my friends of PPI Tokodai, for the wonderful times and helps.

To my family, to my father Dede Ahmad Ghazali, my mother Rina Nurlaela, my sister Rieska Oktavia and my brother Rifki Fuadi, for their prayers and cheers.

And to my lovely wife, Ambiyah Abdullah, daughters, Takia Ayaka Ramadhani, Samia Haruka Rabbani and Nuraisha Hanahilwia for their unlimited supports, cares and loves.

Detection of Sea-breeze Inland Penetration over Coastal Urban Region using Geostationary Satellite Images

Muhammad Rezza Ferdiansyah

Thesis Abstract

Sea breeze is closely related to the living environment in coastal-urban regions. Therefore, the framework for sea-breeze detection is crucial. We proposed a framework to derive a two-dimensional distribution of sea-breeze front (SBF) using geostationary satellite images. The framework includes the application of morphological snake algorithm into visible-band images for automated detection of the cumulus cloud-lines associated with SBF. The verification was undertaken by comparing the passage time of the cloud-line with the arrival time of the SBF estimated from ground observation. Considering that sea-breeze events with cloud-lines are frequently observed both in the tropics and mid-high latitude areas, the method can be applicable any coastal regions over the world.

抄録

静止衛星画像の数値処理による都市域の海風フロント検出

本論は「Detection of Sea-breeze Inland Penetration over Coastal Urban Region using Geostationary Satellite Images」と題し，全6章から構成されている．

第1章「Introduction」では，本研究背景および目的について記述した．大気境界層とは地表面から高度数km程度まで発達する，地表面の熱的および機械的直接作用が及ぶ層として定義され，その中で生活する人々の気象環境（温熱感や大気質など）から局地気象現象（局地的降水や突風災害など）に直接関与するため，その動態を包括的にモニタリングする技術は重要である．その中で臨海部に面した都市は，都市特有な気象場に加え，海と陸の温度コントラストで駆動される海風に通年影響を受けている．海風は密度流であり，その先端の空気の巻き上げにより積雲が形成され，それが海風フロント追跡のシグナルとして使える．これについて，衛星雲画像を用いた雲の追跡手法に関する既往の研究をレビューした．

第2章「Theoretical Background」では大気境界層の一般的な特徴について記述した．特に本研究に直接関係する海風およびヒートアイランド循環の特徴，熱対流と積雲形成のメカニズム，ミクロスケールから総観スケールの気象場の相互作用について記述した．本研究で用いた人工衛星に基づく雲画像および地表面輝度温度画像の測定手法について説明を記述した．また，衛星雲画像の分布から海風フロントを自動検出するためのエッジ検出アルゴリズムについてレビューした．以上より，衛星雲画像から海風フロントが検出できることの物理背景および，それを自動検出するための計算アルゴリズムについて記述した．

第3章「Typical Cloudiness Pattern during Sea-breeze Days」では，ジャカルタを対象とした海風侵入日時の抽出と，その時の気象場の特徴について記述した．地上観測に基づく海風フロント検出のための解析手法，衛星観測から海風フロントを捉えるための解析手法について説明し，現地のデータ解析を行った．地上観測における風向変化情報から海風が発生した日および通過時刻を特定し，さらにその時間前後で気温の低減と湿度の増加を見られた時刻のみを海風通過時刻と定義した．これとは独立して雲画像から海風フロント

のエッジ抽出を行い，そこで観測された日が，地上観測で海風が観測された日に全て包含されることを示した．

第4章「Inland Penetration Detection of Sea-breeze Front」では，ジャカルタ湾から侵入する海風フロントを対象とし，海風フロント検出アルゴリズムの妥当性および精度評価を行った．地上観測から得られた海風侵入時刻と，雲画像解析より推定された同地点の海風通過時刻を比較したところ，両者概ね一致が見られたが，後者のほうがやや遅い時刻になる傾向がみられた．その理由として，（1）海風フロントで形成された積雲が消滅するのにかかるタイムラグ，（2）同積雲が海風のリターンフローや総観場の風で押し流される，（3）強い熱的地表面強制力により海風通過後も積雲形成が持続する，（4）地表面棋院のエアロゾルが多寡な場合に積雲形成が持続する，可能性を指摘した．これに対して都市は強い熱源であり，また汚染物質の発生源であることから，上記の後者2つの影響を助長することが示唆される．

第5章「Application to another coastal urban region (Tokyo, Japan)」では，本研究で確立した衛星雲画像に基づく海風フロント特定アルゴリズム全球に展開することを見据え，日本の関東域に適用し精度評価を行った．関東域は東京湾，相模湾，鹿島灘の3方向から複雑に海風が侵入するため，関東域に2次元的に分布した地上観測点を用いて評価した結果，ジャカルタの事例と概ね同様の精度で計測できることを示した．また，東京湾からの海風侵入速度より相模湾からの侵入速度の方が速い傾向が示された．

第6章「Concluding remarks」では本研究成果及び，現時点で未解決の点を記述した.

List of Symbols

Symbol	Definition
λ	central wavelength
I_r	radiance
T_b	brightness temperature
T_e	effective brightness temperature
$u(s)$	level-set of snakes function
$g(I)$	gaussian function for smoothing image
I	image intensity
ν	curvature parameter of snakes

List of Acronyms

Acronym	Definition
ABL	Atmospheric boundary layer
AHI	Advanced himawari imager
AMeDAS	Automated meteorological data acquisition system
BPL	Observation site at BPLPH office
HCR	Horizontal convective roll
JMA	Japan meteorological agency
KKP	Observation site at KKP office
LCL	Lifting condensation level
PDE	Partial differential equation
SBD	Sea breeze day
SBF	Sea breeze front
UHI	Urban heat island
VIS	Visible band images
WMO	World meteorological organization

List of Figures

List of Tables

Contents

Chapter 1

Introduction

This chapter describes the background of the research problems, objective and importance of the study.

1.1 Motivation

Monitoring the atmospheric boundary layer (ABL) and understanding its behavior is crucial for mesoscale (from 20 km to 2000 km, Figure 1.1) weather forecasting. Many weather phenomena which have societal impacts occur within ABL. The most commonly observed of main mesoscale feature is the atmospheric fronts (a location of a confronting two air masses with different characteristics). The major fronts consist of warm, cold, stationary, and occluded front (mostly are observed in mid and high latitude regions). The monitoring of these type of fronts (particularly its propagation and time evolution) is commonly conducted using the remote sensing method e.g., by geostationary satellite measurement, due to its wide horizontal scale coverage (from 200 km to 2000 km, Figure 1.1) and capability to observe the time evolution of the cloudiness features associated with the fronts.

Moreover, as the lowest part of the atmosphere, the process within ABL involves scale interaction including impact from the surface beneath it. Such as thermal heating impact and mechanical roughness of the surface. In addition to above mentioned fronts, there is sea-breeze front (SBF) which is the cold front type and has smaller meso-scale (20 km to 200 km, Figure 1.1) and occurs in almost coastal region over the world. A sea breeze is caused by the horizontal pressure difference above sea and land surfaces attributed to the contrast of the thermal properties on both surfaces. Since most of the megacities (Figure 1.2) in the world are located near a coastal region (United-Nations, 2018), sea breeze event is closely related to their living environment as seen in several studies concerning urban thermal comfort (e.g., Sasaki et al., 2018; Wang et al., 2017; Ribeiro et al.,

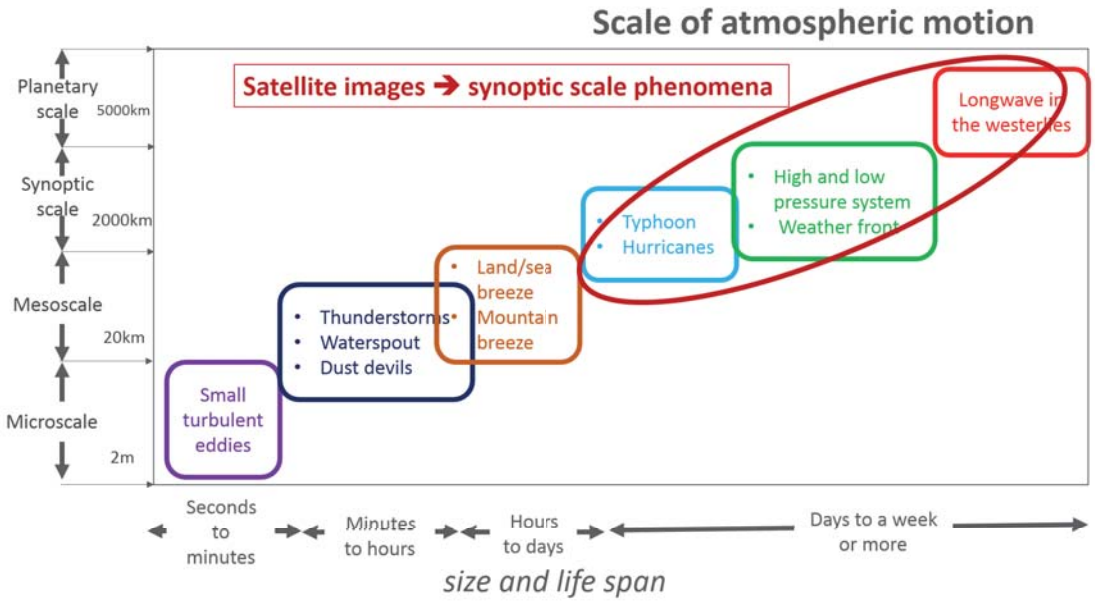

Figure 1.1: Various scale of atmospheric motions from micro-scale to synoptic scale. The synoptic features, such as typhoon and weather fronts are commonly observed from cloudiness characteristic from satellite images.

2018; Hu and Xue, 2016), urban rainfall (e.g., Simpson et al., 2007; Shepherd and Burian, 2003; Dixon and Mote, 2003; Planchon and Cautenet, 1997), and urban pollution (e.g., Igel et al., 2018; Thompson et al., 2007). Despite its importance, to obtain a full measurement of the temporal, horizontal and vertical structure of sea breeze circulation remains a challenging task (Stephan et al., 1999).

The sea-breeze arrival time depends not only on the distance from the nearest coastline, but also on the spatial variations in topographies (e.g., Naor et al., 2017), land surface properties (e.g., Hughes and Veron, 2018), and synoptic weather conditions (e.g., Hughes and Veron, 2018; Azorin-Molina et al., 2009a). These processes non-linearly interact with each other. For the sake of a precise evaluation of the near-surface atmospheric environment, it requires monitoring of the horizontal two-dimensional characteristics of the sea-breeze penetration.

While penetrating inland, the low-level convergence formed in the vicinity of the sea-breeze front (SBF) will induce the updraft air-motion. Under sufficient humidity circumstances, this updraft can lead to the formation of a low-level cumulus cloud-line (Stull, 2012; Miller et al., 2003). This cloud-line exhibits a distinct boundary between cloudy and cloud-free areas and it is potential to be used as the proxy for the location of SBF (e.g., Ferdiansyah et al., 2017). One of the detectable features from satellite images is the cumulus cloudiness associated with SBF (e.g.,

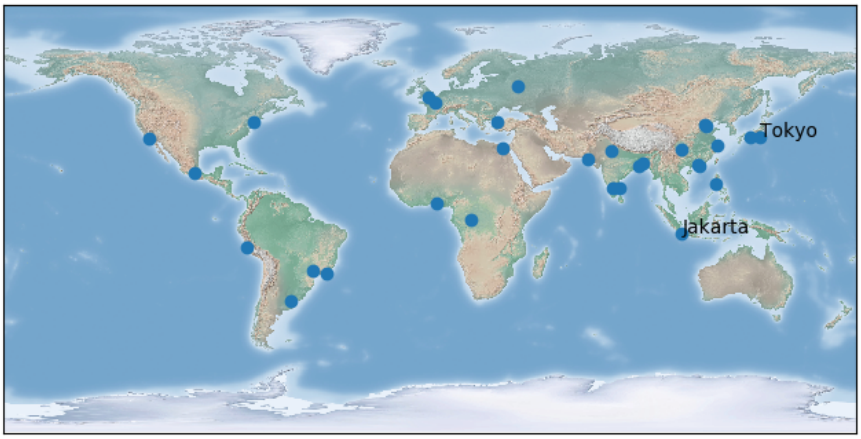

Figure 1.2: Most of the high populated cities (megacities) in the world are located in coastal regions.

Ferdiansyah et al., 2017). The spatial distribution of SBF then can be retrieved by remote sensing approaches such as satellite observation. The focus was put on the identification performance, in previous satellite-based studies, the detection of the cloud-lines using polar and geostationary satellite images was based on manual on-screen digitizing (Damato et al., 2003; Planchon et al., 2006; Anjos and Lopes, 2018).

Some major challenges in cloud-line detection mentioned above, using geostationary satellite images can be given as following (see Table 1.1 for the related existing works):

1. **Automated detection.** The first, with the advancing of spatial-temporal resolution of a geostationary satellite, to detect the SBF using a large number of images, the automated method would give more advantage. Motivated by the edge detection in computer vision, the active contour or snake algorithm is widely used for detecting an edge in textured images automatically (Blake and Isard, 2012). In the snake algorithm, the contour evolution is conducted by a level-set approach (Kass et al., 1988; Osher and Sethian, 1988). The level-set is defined so that the snake can detect the border of the edge. The intensity of the image is usually treated as the level-set (e.g., by using Gaussian function) to where the edge should be approached.

2. **Multi-layer clouds.** The second issue is the contamination of the non-cumulus cloud in the images. From the perspective of image-processing, when we want to apply the snake algorithm, we have to deal with the cloudiness feature on satellite images as a two-dimensional feature. When the

cloud-line is contaminated by the high-level cloud, such as cirrus, it would make the edge detection very challenging.

3. **Computation.** The third one is the computation issue. Fast and stable calculation is expected. In the main snake algorithm, the equations are usually solved numerically using a differential operator, so it requires high computation skills to perform a fast calculation.

The study by (Corpetti and Planchon, 2011) addressed the first and second issues. They applied the snake algorithm to geostationary satellite images for automated detection of the cloud-line. And by combination with wavelet decomposition, they also solved the transparency issue when the image is contaminated by the high-level cloud such as the cirrus cloud. However, despite their accuracy, in their study, the snake equations were solved analytically (still used differential operator). It still has computational issues for implementation in the near-real-time (for monitoring or operational purpose) and analysis with a large number of images. Moreover, no comparison yet with ground observation data in their study. It is necessary to verify using ground observation to examine how representative the detected cloud-lines to be used as the proxy of SBF lines for analyzing the penetration distance and speed of SBF.

In improving the computation issue of the snake algorithm, (Marquez-Neila et al., 2014) proposed the morphological-snake algorithm. In their method, the snake equations are solved by a morphological operator (dilation and erosion) which does not require complicated numerical computation. The algorithm is more straightforward in dealing with the binary images in multi-dimension. Also, the re-initialization of the level-set is not required. Therefore, the simple and fast detection process might be possible. To the best of our knowledge, this method has not been applied yet into geo-referenced meteorological satellite images such as for detecting the cloud-lines associated with SBF.

1.2 Objective and importance of the study

In recent years, the meteorological agencies of several countries who operate the meteorological satellite launched their new generation of geostationary satellites (e.g., Himawari-8, Japan; Fengyun-4, China; GEOS-R, USA; MTG, Europe). Hiwawari-8 which covers Asia-Pacific region is the new generation of the previous Japanese Geostationary satellite, MTSAT2, and is operated by Japan Meteorological Agency (JMA). For full-disk image, the Himawari-8 satellite has higher spatial and temporal resolution than its predecessor, from 1 km to 0.5 km and from hourly to every 10-min, respectively. This is very potential to be explored for observing ABL scale phenomena such as sea breeze.

Table 1.1: Existing works related to cloud-line detection using geostationary images

Study	**Method**	**Validation with arrival time of SBF**
Damato et.al., 2003; Planchon et.al., 2016; Anjos and Lopes, 2018	Manual on-screen digitizing	
Corpetti and Planchon, 2011	Automated, Snakes Algorithm	No
This study	Automated, Morphological Snakes Algorithm (Marquez-Neila et al., 2014)	Yes

The sea breeze study by using the geostationary satellite images is essential. Thus, it is important to construct a framework for deriving the spatial information of inland penetration of sea breeze by using the geostationary satellite image. Which include the validation of the cumulus cloudline that representative to be proxy of the SBF and automated detectection of this cloudline using time-sequential of geostationary satellite images. And for that, the simple, fast and stable calculation is necessary especially for operational purpose which deals with huge images with near-real time processing procedures. Moreover, the global applicability of the proposed framework is also expected in order to be able to be used for sea breeze studies at any coastal regions in the world using various geostationary satellite currently available.

Against the above background, this study aims to construct a framework for investigating the spatial characteristic of the SBF inland-penetration distance and speed over coastal urban regions. The SBF is identified by the cumulus cloud-line which is detected from the visible band images of the Himawari-8 geostationary satellite. The framework includes the application of morphological snakes algorithm for automated detection of the cloud-line. And to examine the representatives of the cloud-lines as the SBF proxy, the validation was undertaken using the arrival time of SBF which is obtained from ground observation data.

1.3 Scopes of the study

Chapter 1: Introduction. Chapter 1 presents the background, objective and importance of the study.

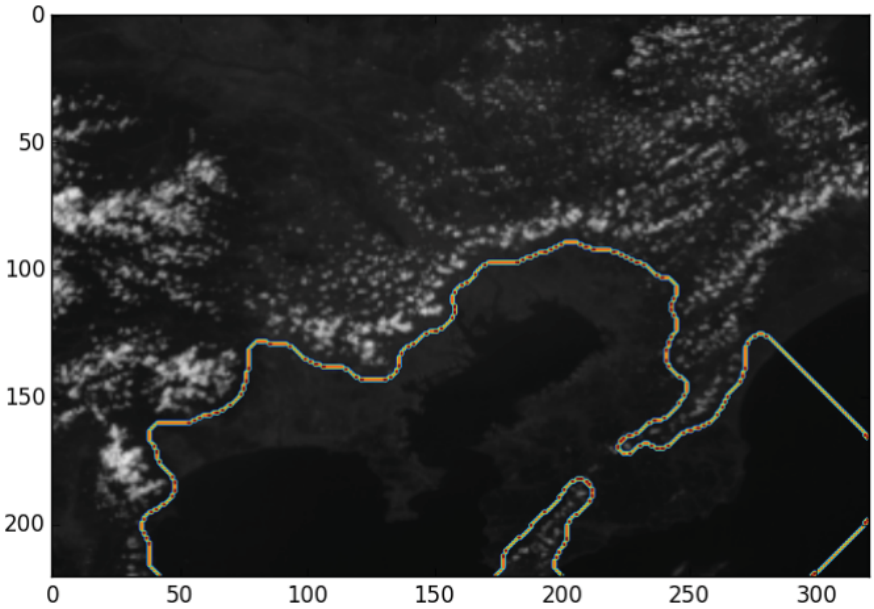

Figure 1.3: Cloud-line appearance associated with sea-breeze front in the VIS band (B03) of Himari-8 satellite image

Chapter 2: Theoretical background. Chapter 2 includes the theoretical background regarding atmospheric urban environment, meteorological satellite measurement and fundamentals of major edge-detection approaches in computer vision.

Chapter 3: Typical cloudiness pattern during sea-breeze days. Chapter 3 provides the first step of the study. This chapter focuses on evaluation and screening of sea-breeze days and cloud-line cases.

Chapter 4: Inland Penetration Detection of Sea-breeze Front. Chapter 4 describes the implementation of morphological snakes algorithm for automated detection of cumulus cloud-line in the VIS band of satellite images. In this second step, the penetration distance and speed of the SBF are validated using the ground observation data.

Chapter 5: Application for another coastal urban. After applying for Jakarta City, in chapter 5, the application of the proposed framework to Tokyo City is described.

Chapter 6: Concluding remarks. The summary of all previous chapters is summarized in Chapter 6. The limitation of the study and future works are also included in this chapter.

1.4 Summary

This chapter comprehends the background of the research problems, objective and importance of the study. This chapter also emphasizes the need to derive spatial distribution of inland penetration of the SBF over coastal urban by using the geostationary satellite measurement, especially for regions with limited ground meteorological observation.

Chapter 2

Theoretical background

This chapter presents the theoretical background related to the scope and objective of this study.

2.1 Atmospheric-boundary layer

Atmospheric-Boundary Layer (ABL) is the lowest part of our atmosphere that exhibits as the boundary between earth surface and free-atmosphere. The depth of the ABL has diurnal cycle and varies between 300 m - 3 km Stull, 2012. In the daytime, ABL consist of surface layer (about 10 percent of the total ABL depth) and mixed-layer (also called as convective boundary layer). At the top of the ABL there is an inversion layer that functions like the cap of the ABL. And between the inversion layer and mixed layer, there is an entertainment zone, the zone where the cloud formation usually occurs (Figure 2.1).

The fair-weather cumulus cloud or shallow cumulus cloud are usually formed at the top of ABL. Their cloud base (usually near the lifting condensation level or LCL) could represent the ABL height. The ABL height over the land varies and it depends on some factors, e.g. topography, surface roughness and thermal property of the land surface. The ABL height for tropical region (such as Jakarta, Indonesia) is higher than the ABL height at the mid-latitude region (such as Tokyo, Japan). Thus, it corresponds to cumulus cloud height at both region (Stull, 2012).

ABL involves several mechanisms and processes including their interactions such as weather, air pollution, rainfall and thermal related phenomena. One of the representative ABL phenomena that influences the weather at coastal region is sea-breeze (Miller et al., 2003). Sea breeze is triggered by the different thermal gradient between land and sea. According to United-Nations, 2018 most of the high populated and industrialized urban areas or megacities are located in coastal region. The cooling effect and ventilation function of sea breeze are expected

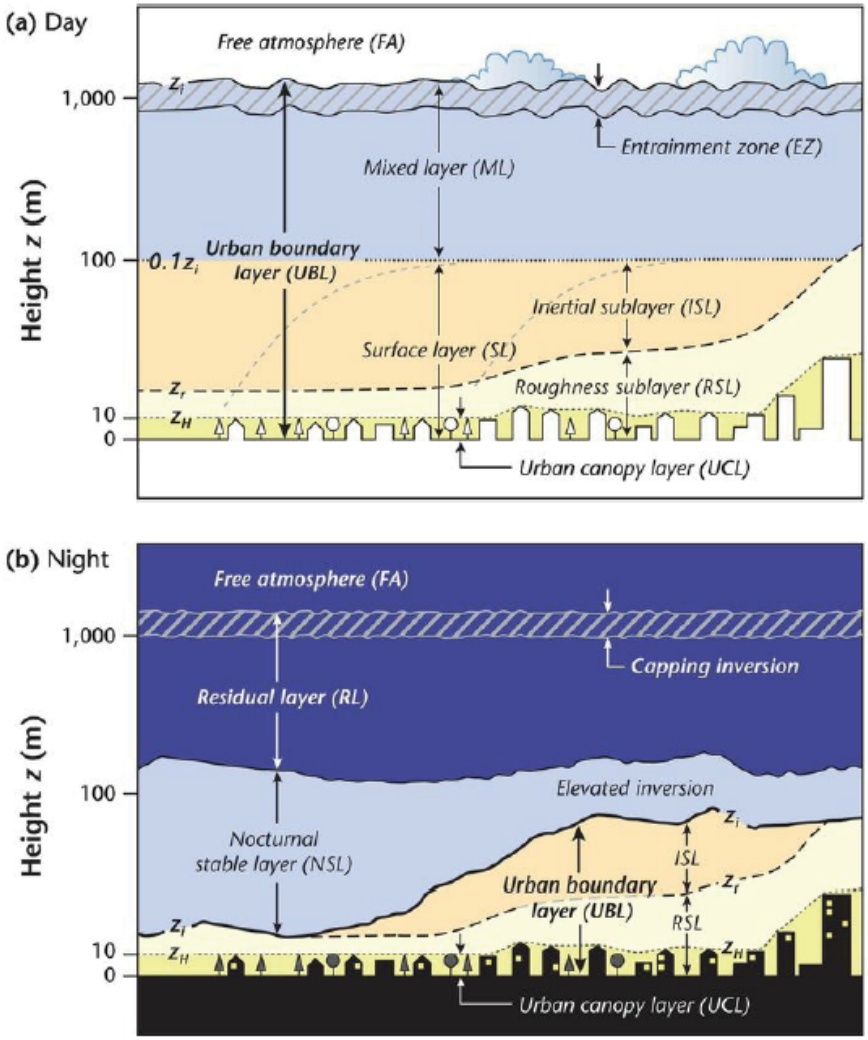

Figure 2.1: Atmospheric-Boundary Layer over urban.(a) Day (b) Night (Source: Oke, et al 2017)

for urban-heat-island (UHI) mitigation and pollution dispersion over the coastal urban regions (Adelaide: (Zhou et al., 2019); New York: (Thompson et al., 2007); Greece: (Papanastasiou et al., 2010); Athene: (Clappier et al., 2000); Yokohama: (Sasaki et al., 2018); Tokyo: (Oda and Kanda, 2009)). Thus, ABL measurement is necessary to further understand the condition of the ABL both vertically and horizontally.

For 1-D vertical-profile measurement using satellite, currently the polar orbit satellite is commonly utilized for ABL probing. It can retrieve the vertical profile of temperature and moisture to probe the condition of ABL using multispectral approach. However, this type of satellite only observed 2-3 times per day and not be able to observe the time evolution of certain ABL phenomena such as sea breeze. So it has limitation for temporal and wide spatial coverage. On the other hand, the geostationary satellite is able to observe continously with wide spatial coverage but has limitation in measuring the vertical profile. Nevertheles, with the improvement of temporal resolution from an hour to every 10-min, it enable us to observe the time evolution of the ABL phenomena by tracing the cloudiness pattern that associated with activity of that related process.

For 2-D horizontal measurement, we mostly still rely on the ground observation. As consequence, to obtain the sufficient information of spatial distribution, we need to deploy many points of ground measurements. Satellite observation, due to its wide spatial coverage can provide some benefit to fill this gap. Therefore, exploring the utilization of geostationary satellite to monitor and observe the time evolution of sea breeze event using its time sequential images.

2.1.1 Sea-Breeze Circulation

Sea breeze circulation is a local circulation and a kind of meso-scale cold-front type. The relationship of sea breeze and off-shore synoptic scale flow is that sea breeze mainly occurs in the weak synoptic condition, clear skies and intense solar radiation Miller et al., 2003. However, sea breeze can also trigger the cloud formation at the sea breeze convergence zone (SBCZ) Miller et al., 2003; Azorin-Molina et al., 2009b. This such discontinuity that is formed at the convergence zone between the sea-breeze flow and the off-shore synoptic wind, it is called also the sea-breeze front (SBF). One of the typical features is the formation of cumulus cloud-line in parallel to the coastline. This can exhibit the location of the SBF (Figure 2.2).

By tracing time evolution of the inland penetration of SBF, we can explore something related cooling and pollutant dispersion, for instance, how far is the affected area by cooling and also how the ventilation function for pollutant dispersion (Sasaki et al., 2018).

To our knowledge, studies that concern about sea breeze detection using the satellite observation particularly the geostationary satellite are still limited (e.g.,

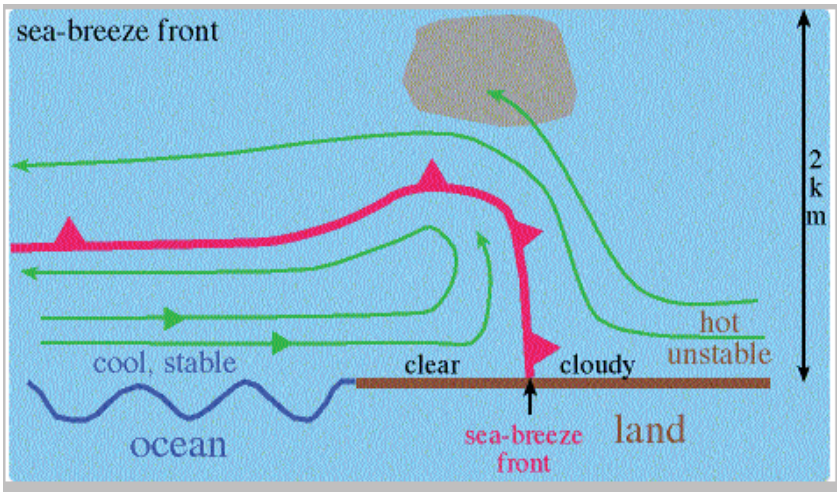

Figure 2.2: Schematic of cumulus-cloud formation in the vicinity of sea-breeze front. (Source: apollo.lsc.vsc.edu)

Damato et al., 2003; Planchon et al., 2006; Anjos and Lopes, 2018). Further exploration of the cloud features observed by current new generation satellites, which has been improved in term of temporal and spatial resolution, has great potential for further examination and research.

2.1.2 Urban heat-island circulation

Urban heat island (UHI) is a phenomenon when the city or urban area experiences warmer temperature than the surrounding area (Oke, 1995). The intensity of the UHI will relate to the ability of the urban surface in absorbing and hold the heat of the solar radiation during day time. So it would be depend on the urban surface roughness, concrete material used of the houses and building, built up areas, street canyon and also the antrophogenic-heat emission released. Since the heat capacity of the urban surface is larger than surrounding rural areas, it releases the heat during nighttime, resulting the larger nocturnal temperature different (i.e., reduces the maximum air temperature different at daytime and increases the minimum air temperature different at night).

The UHI circulation is initiated by the temperature increasing of urban surface due to daytime solar heating. Relatively low pressure will be form in the urban areas, resulting the convergence flow from the surrounding rural toward the urban. Related to the synoptic condition, wind speed and cloud cover are some of the parameters that can influence the intensity of the UHI circulation.

Regarding the relationship with sea-breeze circulation and UHI circulation. The numerical study by Freitas et al. (2007) reported that the UHI accelerates the

penetration speed of SBF due to the enhanced convection in the city center. While arrive at city center, the SBF will be stagnant for about 2 hours and then penetrate beyond the city with the decreased speed. Similar finding was also reported in a laboratory study by Cenedese and Monti, 2003. Other sea-breeze studies that relate with the surface roughness influence to the UHI intensity such as Thompson et al., 2007; Varquez et al., 2015; Liu et al., 2009; Ng et al., 2011; Hai et al., 2018 can be given.

2.1.3 Thermal convection and cloudiness

A study by (Azorin-Molina et al., 2009b) reported the climatology of the cloudiness associated with sea breeze based on surface cloud observation. Based on their finding, the sea breeze can increase the formation of stratus and cumulus cloud in the convective internal boundary layer and also can induce the formation of thunderstorm clouds in the sea-breeze convergence zone.

We can see the mechanism of the sea-breeze front and its associated cumulus cloud-line formation in the micro-scale, mesoscale and synoptic perspectives. The individual cumulus-cloud cycle is the micro-scale persepective. The cumulus cloud associated with SBF propagation will have a cycle such as following (e.g., Azorin-Molina et al., 2009b; Miller et al., 2003): (1) the convection to enhance in vicinity of the front area, (2) cumulus-clouds to form, (3) the convection to reduce due to the sea breeze intrusion (cooling impact), and (4) cumulus-cloud to dissipate. As a visible feature (such as in the satellite image), the cloud-line exhibits the distinct boundary between clear area (behind SBF) and cloudy area (in front of SBF).

In mesoscale perspective, that cloud dissipation may take longer time (long-lasting cloud). And for that, two possible reasons can be given as: (1) due to the enhanced convection and UHI (Kanda et al., 2001; Varquez et al., 2015) and (2) due to polluted environment (Fan et al., 2016). The continues and consistent heating (for instance due to UHI circulation) is favorable for convection and updraft motion.

Regarding the vertical updraft mention above, cloudiness and the representative height of the cumulus cloud, Figure 2.3 and Figure 2.4 show the vertical structure of the sea breeze case on September 14, 2011 analyzed in Varquez et al. (2015). In this case the SBF was accompanied by the cumulus cloudline. The arrival of the SBF can be regarded as maximum vertical velocity and the passage of cloudline at the site. In this case, the arrival time can be estimated between 11∼11:30AM and 13∼13:30AM at Tokyo and Hachiouji, respectively. As can be seen also in those two figures, the height of the cloud was at around 850hPA level (about 2 km height or near the top of ABL).

The fair-weather cumulus cloud or shallow cumulus cloud are usually formed at the top of atmospheric boundary-layer (ABL). Their cloud base (usually near

the lifting condensation level or LCL) could represent the ABL height. The ABL height over the land varies and it depends on some factors, e.g. topography, surface roughness and thermal property of the land surface. The ABL height for tropical region such as Jakarta, Indonesia is higher than the ABL height at the mid-latitude region such as Tokyo, Japan. And this corresponds to cumulus cloud height (Stull, 2012).

Another micro-scale interaction also exists between cloud formation and the vertical motion (updraft), particularly with horizontal convective roll (HCR). According to numerical study by (Dailey and Fovell, 1999), due to interaction between SBF and HCR, there are post-frontal cumuli, frontal cumuli, and HCR cumuli. This SBF cloudiness is enhanced by two particular reasons: (1) the additional lifting of the HCR updraft;(2) the increase of the convective instability in the air inside the roll updraft (as the roll will lift the moist air from lowest level that will increase the convective instability and eventually will increase the frontal cumuli at the roll updraft intersection).

Based on above, the characteristic of the SBF cloudiness over different surface condition, e.g., between urban and non-urban area, can be different. Urban provide more additional sensible-heat release that will provide extra lifting of the roll updraft than non-urban surface (e.g., Inoue and Kimura, 2004; Theeuwes et al., 2019). Even though, forest area may provide more moisture than urban area (e.g., Teuling et al., 2017), the various roughness elements contributed by the high-rise buildings over urban area may cause frictional drag and induce more enhanced roll updraft.

2.1.4 Scale interaction

Even though the individual thermal convection (micro-scale) and the sea-breeze structure (mesoscale) are independent phenomena, there is possible interaction between them. As reported in a numerical study by Ogawa et al., 2003, that such scale interaction (between SBF and convective cell) can cause the variability of the propagation speed of SBF. The key factor that causes such interaction was considered as the spatial discontinuity of temperature and wind. Also, in a numerical study by Kanda et al., 2001, they studied the mechanism of the cloud-line formation along the convergence line in Tokyo. They reported that two conditions are required for such phenomena; (1) convergence between two sea breeze (large scale) and (2) heating from the surface (micro-scale).

Regarding the interaction of the sea breeze over the urbanized area (with complex building morphology), a numerical study by Varquez et al., 2015 found that the delayed penetration of the sea breeze due to the significant drag of the surface. This delay caused the less heat-advection to the downwind area, stronger mixing turbulent and the deeper boundary layer over the urbanized area. And a satellite

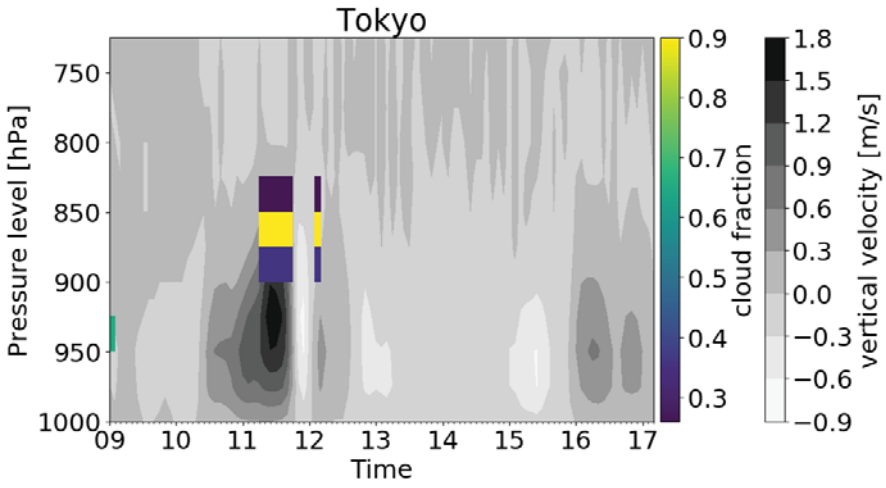

Figure 2.3: Vertical velocity and the cloud position at Tokyo. The enhanced of vertical wind and the location of the cumulus at the top of ABL indicated the arrival time of sea breeze front at Tokyo was between 11∼11:30AM. Time resolution is every 5 minutes. Data source: Varquez et al. (2015)

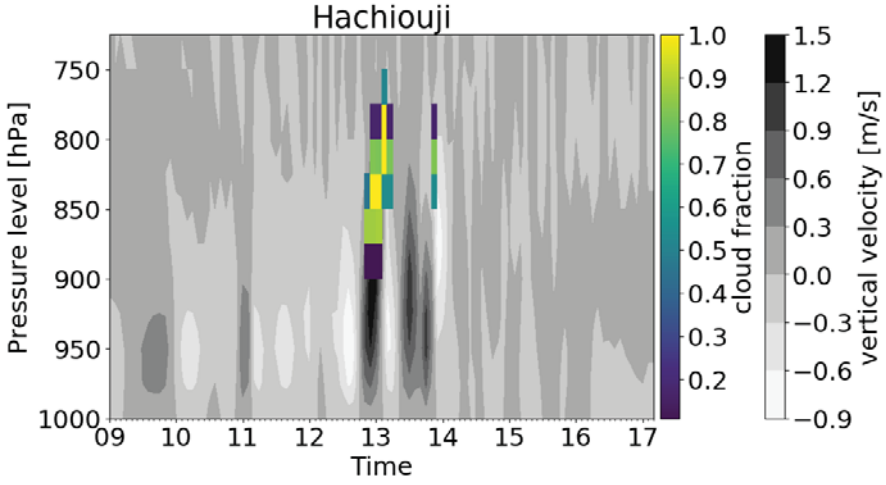

Figure 2.4: Vertical velocity and the cloud position at Hachiouji. The enhanced of vertical wind and the location of the cumulus at the top of ABL indicated the arrival time of sea breeze front at Hachiouji was between 13∼13:30AM. Time resolution is every 5 minutes. Data source: Varquez et al. (2015)

observation-based study by Inoue and Kimura, 2004 reported also that the urban areas are conducive for the formation of low-level clouds due to the following two mechanisms. (1) increasing of sensible heat flux over urban; (2) the heat contrast between urban and its adjacent areas which may induce local circulation (such as UHI circulation). Both mechanisms are also sensitive to the synoptic-scale wind and radiation.

How the influence of the synoptic-scale, we put focus on wind and radiation as the two synoptic meteorological variables. Since the low-level clouds such as cumulus propagate following the wind in ABL height level (Fujita et al., 1975; Ottenbacher et al., 1997), the stronger opposing wind will somehow influence the position and the formation of the clouds. For radiation, since we only selected for SBD which are accompanied by the cloud-line of fair-weather cumulus, the high intensity of solar radiation could increase more sensible heat flux, induce more updraft and convection and eventually make the ABL in well-mixed condition.

In the interaction with thermal convection, the mesoscale and synoptic wind can also influence in producing the wind shear that will define the organization of the cumulus clouds. Two types of them that most likely to occur are roll structure and fishnet formation (e.g., Grossman, 1982; Yagi et al., 2017). Roll structure is formed when the strong mean wind induces the wind shear to be more dominant than the thermal buoyant, so the cumulus cloud will be formed aligned in parallel with the wind direction. And the fishnet is formed when wind shear is weak and the thermal buoyant is dominant. Among these two types of formation, too parsed clouds and the cloud-line that formed parallel along the sea breeze direction is difficult to be delineated by snake algorithm (the appropriate smoothing is required). In this study, such cloud-line cases, as well as the irregular cloud-pattern, are excluded from the SBF cases.

2.2 Geostationary meteorological satellite

Based on their orbital types, the meteorological satellite can be divided into polar, low-earth-orbit, and geostationary orbit satellite. Active and passive sensors onboard the satellite usually transmit the microwave band and measure infrared band, respectively.

Himawari-8 (Figure 2.5) is the new generation of geostationary satellite operated by the Japan Meteorological Agency. It has been launched in October 2014 and used for operational purpose since July 2015. The geostationary position is 140.7 degree east and on about 36.000 km altitude. The Advanced Himawari Imager (AHI) sensor that onboard of the satellite has 16 channel bands (3 visible, 1 near-infrared, and 12 infrared bands, see Table 2.1 and Figure 2.6).

The satellite data used in this study is the Himawari Standard Data (.hsd)

Figure 2.5: Himawari-8 Geostationary satellite. (Source: Bessho et al., 2016)

Table 2.1: Advanced Himawari Imager (AHI) sensors

	Band	Central Wavelength (μm)	Res (km)	Usage
Visible	1	0.47	1	Aerosols
	2	0.51		Solar insolation
	3	0.64	0.5	Clouds
Near-infrared	4	0.86	2	Vegetation
Infrared	5	1.6	2	Snow and ice discrimination, cloud-top phase
	6	2.3		Cloud-particle size, snow, cloud phase
	7	3.9		Low fog and stratus, clouds, fires, atmospheric motion vectors, volcanic ash
	8	6.2		Upper-level water vapor
	9	6.9		Mid-level water vapor
	10	7.3		Lower-level water vapor
	11	8.6		Cloud-top phase, dust, SO_2
	12	9.6		Total-column ozone
	13	10.4		Clouds
	14	11.2		Clouds
	15	12.4		Clouds
	16	13.3		Air temperature, clouds

format with geostationary projection based on the World Geodetic System 1984 (WGS84) geographic coordinate system (coverage area is shown in Figure 2.7).

2.2.1 Radiance measurement

Conversion from counts to radiances is calculated as following Equation 2.1.

$$Radiance = Gain * Counts + Constant[mWm^{-2}sr^{-1}(cm^{-1})^{-1}] \tag{2.1}$$

Where Constant $[W/(m^2sr\mu m)]$ and Gain $[W/(m^2sr\mu mcount)]$ are the offset constant between the pixel count and the physical radiance and the linear-calibration coefficient, respectively. Both are extracted from the on-board calibration of the satellite.

For infrared bands (Band 04 to Band 16), this radiance values can be further converted to brightness temperature using the following Equation 2.2 and Equation 2.3.

$$T_e(\lambda, I_r) = \frac{hc}{k\lambda} \frac{1}{ln(\frac{2hc^2}{\lambda^5 I_r} + 1)} \tag{2.2}$$

$$T_b = c_0 + c_1 T_e + c_2 T_e^2 \tag{2.3}$$

Where T_e, T_b, I_r and λ are effective brightness temperature, brightness temperature, radiance and central wavelength, respectively.

And for the visible bands (Band 01 to Band 03), the conversion from radiance to albedo can be calculated more simple using the following Equation 2.4.

$$Albedo = c' I_r \tag{2.4}$$

Where c' and I_r are coefficient and radiance, respectively. All the constant values appeared in each equation can be read in the header section of the .hsd data.

2.3 Edge detection in computer vision

2.3.1 Level-set approach and Snake algorithm

As state-of-the-art for edge detection, the snake algorithm is widely used to extract the contours and detect the edges of the object in a computer vision field (Blake and Isard (2012)). In this algorithm, the evolution of snake contour is conducted by minimizing certain functional energy of the snake (E_{snake} in Equation 2.5) and usually performed implicitly using level-set approach (Kass et al. (1988); Osher and Sethian (1988)). The snake contour evolves within the given level-set until it approaches the target object (such as an edge or border).

$$E_{snake} = E_{internal} + E_{external} \tag{2.5}$$

Let the snake contour be parameterized in a binary level-set as $u(s)$, $u(s) = (x(s), y(s))$ and s $\in$ [0,1]. Equation 2.5 can be given as following.

$$E(u(s)) = \frac{1}{2}\int_0^1 \left(\alpha\frac{\partial u(s)}{\partial s} + \beta(s)\frac{\partial^2 u(s)}{\partial s^2}\right) ds + \int_0^1 I(u(s))ds \tag{2.6}$$

The internal energy in Equation 2.5 is the curvature property of the snake (smoothing element) which consists of first derivative (tension) and second derivative (elasticity) of $u(s)$. From Equation 2.6 we see that each of those curvature terms is controlled by parameter α and β respectively. The external energy can be given as the intensity I of the image itself which attracts the snake contour to approach the target object (Kass et al. (1988)).

To minimize that functional energy, there are two proposed models for time evolution of the snake contour and with the level-set $u(s)$ approach, Geodesic Active Contour (GAC, Equation 2.7) (Caselles et al. (1997)) and Active Contour Without Edge (ACWE, Equation 2.8) (Chan and Vese (2001)).

$$\frac{\partial u}{\partial t} = g(I)\cdot|\nabla u|\cdot div\left(\frac{\nabla u}{|\nabla u|}\right) + g(I)\cdot|\nabla u|\cdot\nu + \nabla g(I)\cdot\nabla u \tag{2.7}$$

$$\frac{\partial u}{\partial t} = |\nabla u|\left(\mu\cdot div\left(\frac{\nabla u}{|\nabla u|}\right) - \nu - \lambda_1(I-c_1)^2 + \lambda_2(I-c_2)^2\right) \tag{2.8}$$

The terms in Equation 2.7 and 2.8 correspond to elasticity term, curvature term with parameter ν and attraction term, respectively. In the GAC model, we need $g(I)$ as the edge detector to obtain boundary information of the target edge. All three terms in the GAC model depend on this $g(I)$. It is usually defined as a decreasing function constructed of array convolution between Gaussian filter and image intensity. In contrast with that, since the $g(I)$ does not appear in the ACWE model (Equation 2.8), contour evolution using ACWE would be less-dependent with the intensity of the image. In ACWE, the image intensity inside (c_1) and outside (c_2) the snake contour (weighted with parameter λ_1 and λ_2, respectively) are considered . So, the boundary information is not required in ACWE. However, both snake contour models contain a set of differential equations and they are usually solved by a differential operator such as finite-difference of a numerical scheme.

2.4 Summary

In this chapter we briefly introduce the sea-breeze as the representative ABL process that commonly occurs in coastal regions. Since the process within ABL is influenced by surface condition beneath it, the sea breeze can also involve and interact with a different scale of phenomena such as urban heat island (meso-scale) and thermal convection (local/micro-scale). In certain condition, the typical cloud-formation (e.g., cumulus cloud-line) becomes the proxy of such phenomena and this cloudiness characteristic (warm temperature and high albedo) become a detectable features in the satellite images. The snakes algorithm is a state-of-the-art for automated edge-detection of such cloud-line features appeared in the visible-band of geostationary satellite images.

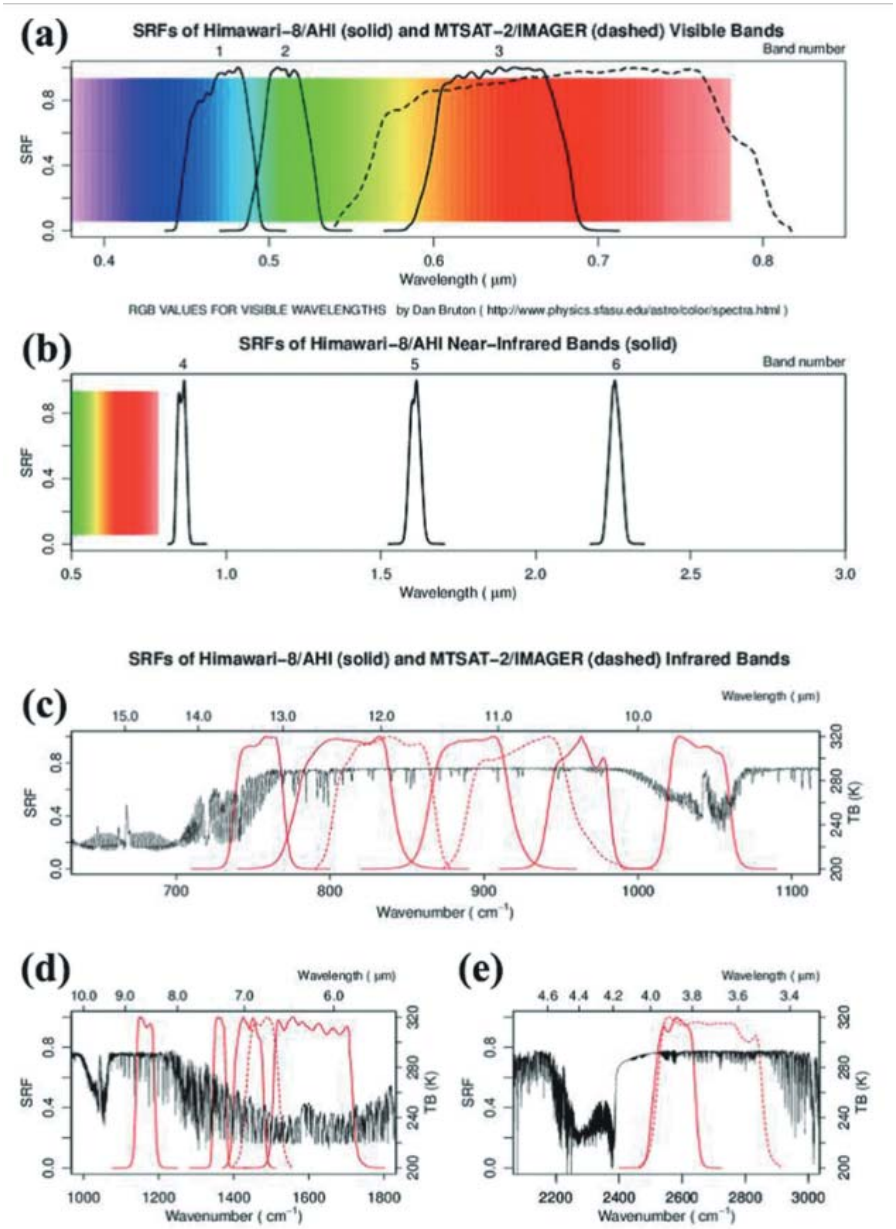

Figure 2.6: Signal response function of band channel of the AHI sensors onboard. (Source: Bessho et al., 2016)

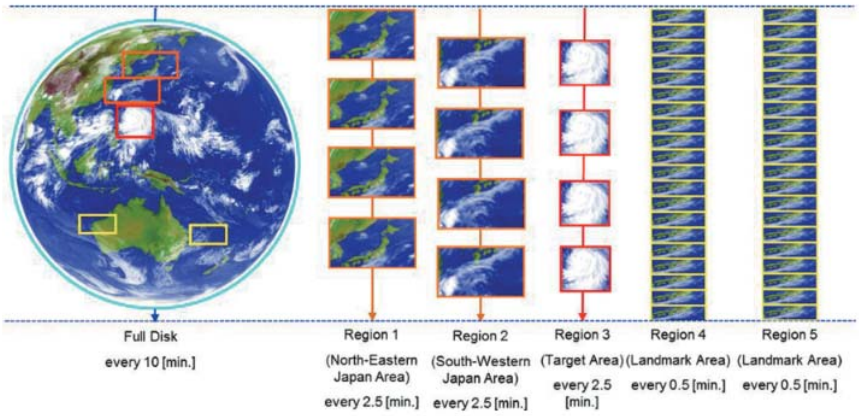

Figure 2.7: Time resolution for full-disk image and coverage area of Himawari-8. (Source: Bessho et al., 2016)

Chapter 3

Typical Cloudiness Pattern during Sea-breeze Days

3.1 Introduction

In this chapter we present the typical cloudiness pattern during sea-breeze day. Our study area Jakarta, the capital city of Indonesia, is one of the emerging megacities in Asia, with a population of more than 10 million people (United-Nations, 2018). Jakarta is located in the tropical coastal region and has a humid climate with a synoptic background of austral monsoon during the dry season. Also, urbanization is still increasing, especially in the western side of the region in recent years. As shown in figure 3.1, Jakarta city is located in a northwestern plain area of Java island in the Indonesian archipelago. The area is bounded by the Java-sea coastline on the north (oriented from west to east) and a mountainous area in the south and west. The elevation of the plain area reaches up to 50 m above sea level, and the base of the mountainous area is about 200 m, located about 50 km inland from the coast. The inland penetration of the sea breeze is somehow restricted by this region's varied topography. The prevailing wind in the dry season (May to October) is a dry air-mass brought by easterly winds blowing from the Australia continent. The northerly wind of local scale circulation in daytime exhibits a dominant flow-mode due to sea breeze circulation.

3.2 Data

3.2.1 Ground observation data

Figure 3.1 and table 3.1 show the location of six meteorological stations located within the study area (station: TJP, KMO, CGK, PBT, SRG, and DMG). These

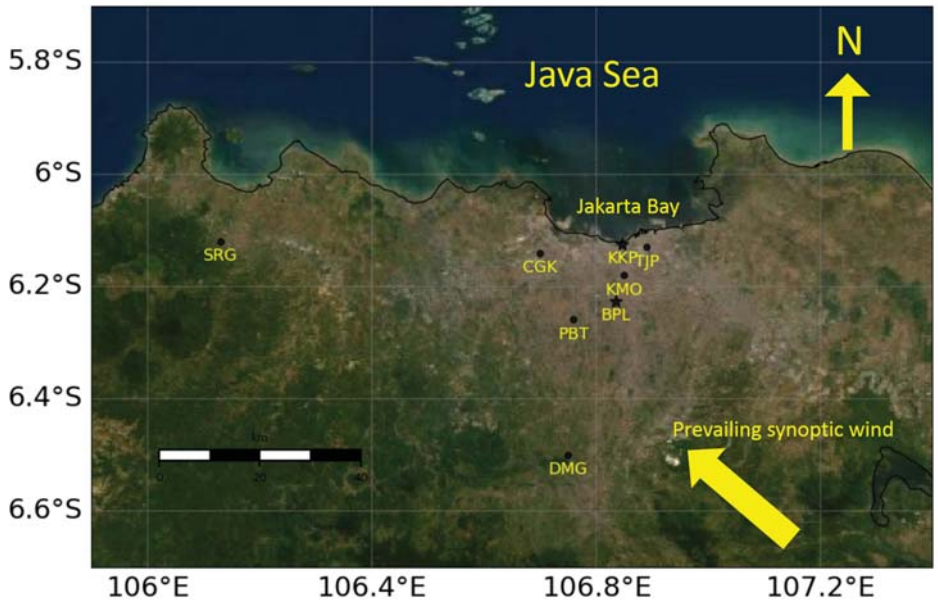

(a) Urbanized area around Jakarta City

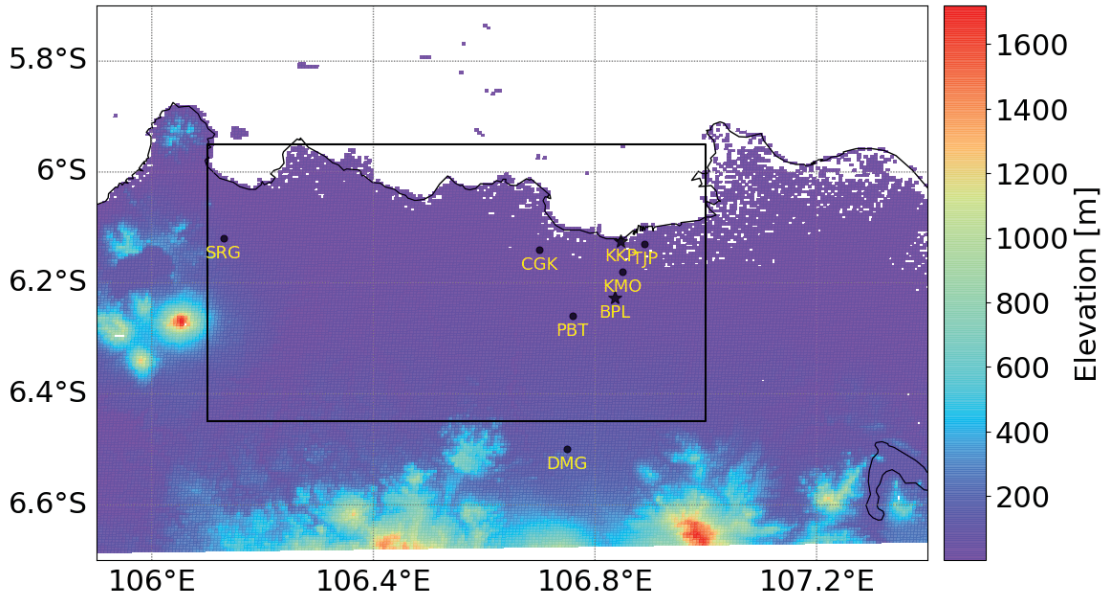

(b) Topography (unit in meter)

Figure 3.1: The study area. The square in topography map of 3.1b depicts the urbanized area around Jakarta city and the less-urbanized area (suburban) in its western side. (After Ferdiansyah et al., 2020)

stations are operated by the Indonesian Agency for Meteorology, Climatology, and Geophysics (BMKG). BMKG regularly provides daily weather information referred to as the synoptic meteorological report, which includes data on air pressure, air temperature, relative humidity, wind speed, and wind direction. The data cover three months: July-August-September in 2017 and 2018. These station data are mainly used to define the climatology around the Jakarta region.

Besides, we deployed two observation points also, which are located at the top of the research and development office building of the Ministry of Maritime and Fisheries Affair (KKP) and the Jakarta Environmental Services office building of the Indonesian State Minister for The Environment (BPL). The former is located near the coast and the latter is in the city center. The time interval of the data is every 10-minute. The observed parameter and data period are as same as the meteorological station. We used the ground observation data to select SBD based on the wind field information and to estimate the arrival time and speed of SBF.

Regarding the boundary layer measurement, the tower measurement that we deployed at KKP and BPL site was 18 m and 30 m, respectively. Since the average building height in the surrounding area is less than 5 m, we can assume that the measurement sites are above the roughness sub-layer. The wind observation at the sites somehow can represent the condition of the atmospheric-boundary layer (ABL). Since we attempt to connect between the cumulus cloud motion and the wind observation at the ground. We consider that the wind condition observed at the sites will depend on two parameters, the stability, and the ABL height.

Table 3.1: Meteorological station and observation point.

ID	Station	Longitude	Latitude	Distance from the coast (km)
A	KKP	106.846	-6.124	0.11
1	TJP	106.866	-6.1	2.64
2	CGK	106.65	-6.117	5.63
3	KMO	106.83	-6.18	6.26
4	SRG	106.13	-6.12	10.6
B	BPL	106.835	-6.226	11.48
5	PBT	106.759	-6.259	16.63
6	DMG	106.75	-6.5	42.59

3.2.2 Satellite data

Our study area, Jakarta, is at segment 6 among 10 segments of the full-disk images of Himawari-8 satellite. We used the visible images of the B03 band (center wavelength: 0.64 microns, also known as a red band) to obtain the cloudiness features.

B03 is the highest spatial resolution (500 m) among band channels of Himawari-8. The characteristic of fair-weather cumulus is parsed and textured, so the finer resolution B03 would be suitable to detect cumulus clouds in the daytime. We also used thermal infrared images of the B13 (center wavelength: 10.4 microns) to derive the surface temperature. B13 is the band that has the least absorbed radiance by the atmosphere (atmospheric window band) and the spatial resolution is 2 km. In radiative correction, the digital count number is converted to radiance and then radiance is converted into reflectivity (albedo) value and brightness temperature (Tb) for band B03 and B13, respectively. In geometric correction, each pixel of albedo and Tb is projected into a geostationary projection coordinate.

3.2.3 Additional data

The elevation data provided by the US Geological Survey is utilized for land-sea masking. We also used this data to construct the coastline dataset which has been adjusted to match the pixels of satellite images which were projected into geostationary projection. The dataset is used to define the distance of the sea-breeze front from the coastline. In addition to the above-mentioned data, we utilized also the wind profile of radiosonde observation at CGK and ERA-interim re-analysis data (Dee et al. (2011)) to obtain the synoptic condition for our particular case studies.

3.3 Method

3.3.1 Sea-breeze day selection

To ensure that the cloud-lines in the sea-breeze day (SBD) are associated with an SBF, we selected the candidates of SBD and defined the arrival time of SBF using the ground observation data. The change of wind direction became the key indicator, that there should be a clear transition of wind direction from seaward to landward (from offshore to onshore) (Borne et al. (1998)). We set the following criteria for selecting SBD: (1) the existence of wind change direction from land breeze to the sea-breeze mode and (2) the sea-breeze mode exists at least for two consecutive hours.

Sea breeze as a type of cold front is the moist and cold air-mass blowing from sea to inland due to different heating of the sea-land. Its arrival can be indicated by increasing moisture, a reduction in the increase rate of air temperature, and an increasing wind speed of stable wind direction. The arrival time of the SBF was estimated based on the time of the significant increase of the moisture. Since the specific humidity will not change by the change of air volume (due to rising

temperature), specific humidity was used to quantify the moisture rather than the relative humidity which will increase as a result of the rising air temperature. Therefore, the arrival time of SBF was estimated, based on the following parameter: temperature, wind speed, wind direction, and specific humidity.

Among the SBD candidates, we estimate the arrival time of SBF by the following procedure: (1) Find several peak times of the air temperature. (2) Around those, we search the time when there is a significant increase in both specific humidity and wind speed. (3) Next, we select the collocated time as the arrival time of SBF at that location. Since the estimation of arrival time using hourly data of meteorological station is not detailed enough, we used only 10-minute intervals data from two observation sites, KKP and BPL (Figure 3.1), to estimate the arrival time. If the arrival time at both locations cannot be confirmed, that candidate SBD will be rejected.

The measurement height (temperature, humidity and wind) of KKP and BPL site are 49.5 m and 27 m, respectively. And for the height of the weather stations of BMKG are following the WMO standard (2 m for air temperature and 10 m$\sim$ for wind). Regarding the height dependency of the SBF arrival time, previous studies (e.g., Chiba, 1993; Helmis et al., 1987; Arrillaga et al., 2016) reported that there is no significant vertical variation for air temperature and vertical velocity (w component) at the lower part of ABL, especially at surface layer (Figure 3.2. Thus, the height dependency of the measurement height can be considered small and no significant time different of sea breeze arrival even when we measured at different height.

3.3.2 Cloudiness

The reflectance of the cloud (albedo) depends on the solar position. Since we want to track the time evolution of cloud propagation, we need to normalize the albedo values to reduce the dependency with solar time. In the pre-processing process, after performing radiometric and geometric corrections, we normalized the albedo values of B03 images, following the method proposed by Zhuge et al. (2012). Their method is applicable for areas that have solar and satellite zenith angles than 60 degrees. The normalization factor is calculated by considering the zenith and azimuth angle based on sun and satellite positions.

The normalization of the albedo has two purposes; to enhance the lower value of albedo in the morning time (due to lower solar elevation) and to minimize the solar time dependency. When we test the algorithm to Jakarta region (Figure 3.8), we found that the relative frequency of the albedo less than 0.3 (ground albedo, which is mostly to be plant, sand, coast, sea, land, etc) is fluctuating by time. Therefore, the value of 0.3 is reasonable to be used to define the cloud object. And according to another reference, such as (Taniguchi et al., 2001), they used the value of 0.3 as

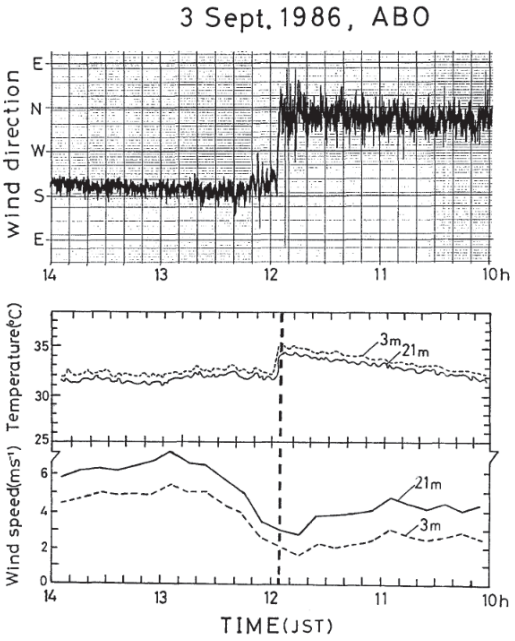

(a) Air temperature and wind

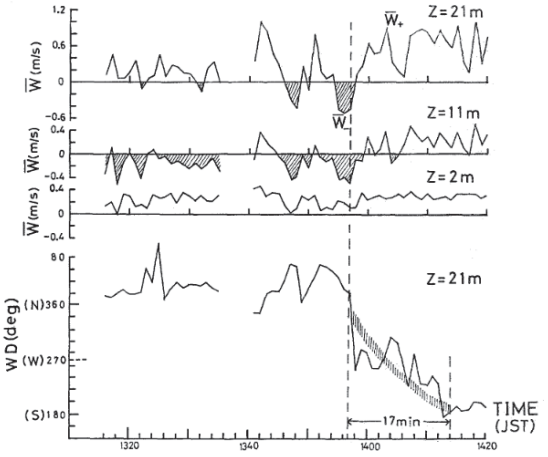

Fig. 5. Time-series of the vertical wind component ($\bar{w}$) at three heights (2,11 and 21 m) and wind direction at 21 m measured by SAT for the period 1316 to 1420 JST on 19 November, 1986. $\bar{W}_-$ and $\bar{W}_+$ refer to downdrafts and updrafts, respectively.

(b) Vertical velocity (w component)

Figure 3.2: The vertical profile from 50 m tower measurement. No significant vertical variation within 5 minute temporal resolution. Image source: Chiba (1993)

the threshold value to discriminate the ground albedo and cloud albedo (Figure 3.3). In this study, the albedo value of 0.3 was used as the threshold to define the cloud object (Zhuge et al. (2012); Taniguchi et al. (2001)). And to define the spatial cloudiness pattern over the study area, we calculated the frequency of cloud occurrence during SBD within periods of July-August-September from 2017 to 2018 (184 days). This period is the dry season in Jakarta and it is favorable for sea-breeze formation (Hadi et al. (2000, 2002)).

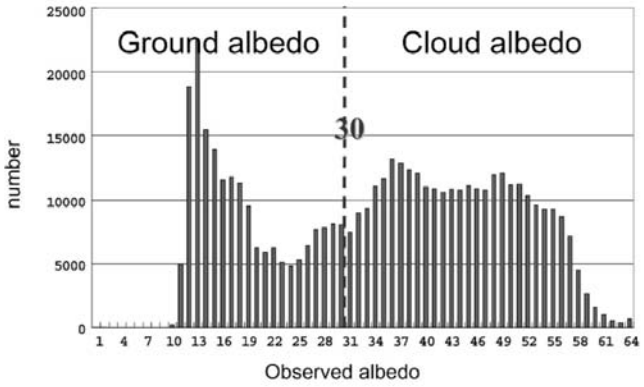

Fig. 3. The distribution of the observed cloud.

Figure 3.3: Albedo threshold for determining the cloud object. From Taniguchi et al. (2001)

3.4 Results and discussion

3.4.1 Sea-breeze Day Selection

To ensure the sea breeze related cloud line, we conducted SBD screening and estimation of SBF arrival using the ground observation data as mentioned in the method section. From 184 available datasets, we selected 102 SBD and 82 non-SBD cases. Among 102 SBD cases, 84 days were the cases that the SBF arrival time was able to be detected at both KKP and BPL (SBF cases). And among these 84, 53 days were the cases of SBF accompanied by cumulus cloud-line. The remaining 31 days were the SBF cases with irregular cloudiness, including the clear-sky cases.

One of the indicators of the SBD is the change of wind direction from the land breeze direction to the sea breeze mode. From the hourly mean of observation data, all stations except DMG and PBT showed a distinct counter-clockwise transition of wind direction (Figure 3.5). This is a typical pattern of sea breeze for coastal areas

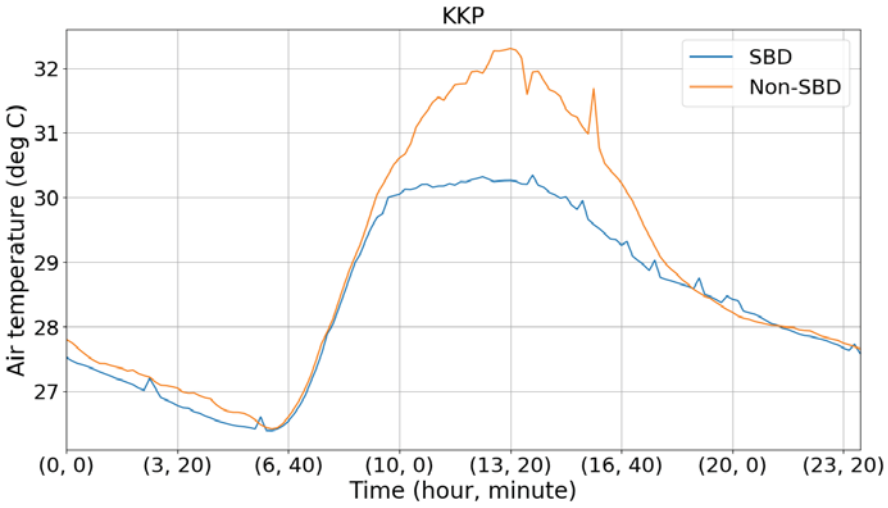

(a) KKP

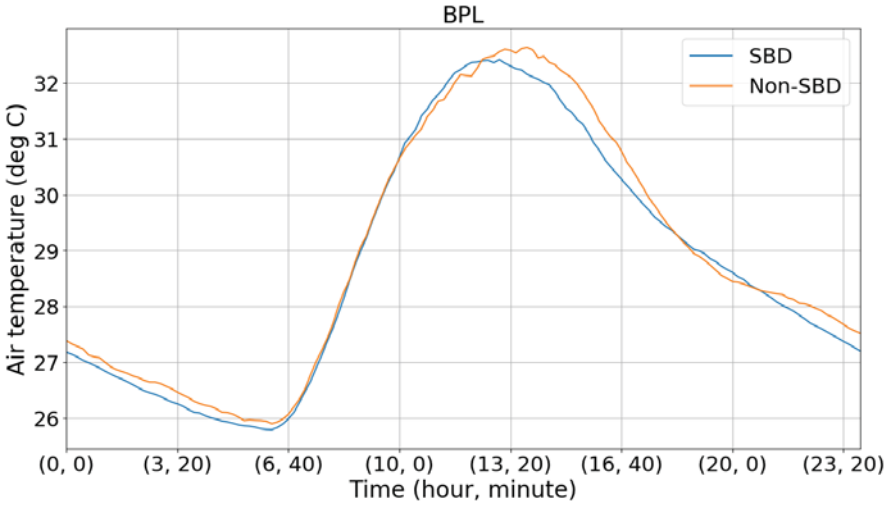

(b) BPL

Figure 3.4: Composite of air temperature during sea-breeze days and non-sea-breeze day. The x-axis is the time.

located in the southern hemisphere (Kusuda and Alpert, 1983) such as the Jakarta region. For DMG, the transition is clockwise and the topography is likely to influence. As reported by e.g., Shiraki (1986); Prtenjak et al. (2008) which pointed out the influence of topography for the transition wind at a mountainous area in the northern hemisphere. And for PBT, the obvious change of wind direction was not observed. The local wind-variation is likely to be dominant in this location. The maximum temperature of SBD cases for both KKP and BPL is lower than that during non-SBD (Figure 3.4). The difference between the maximum temperature during SBD and non-SBD is 2 and 0.5 deg for KKP and BPL, respectively. And the specific humidity increased by 1.2 - 1.5 g kg^{-1} for SBD cases. The results indicated that the air temperature decreasing and humidity increasing due to sea breeze events are observed in this region. The cooling effect is much larger at coastal than that at the city center.

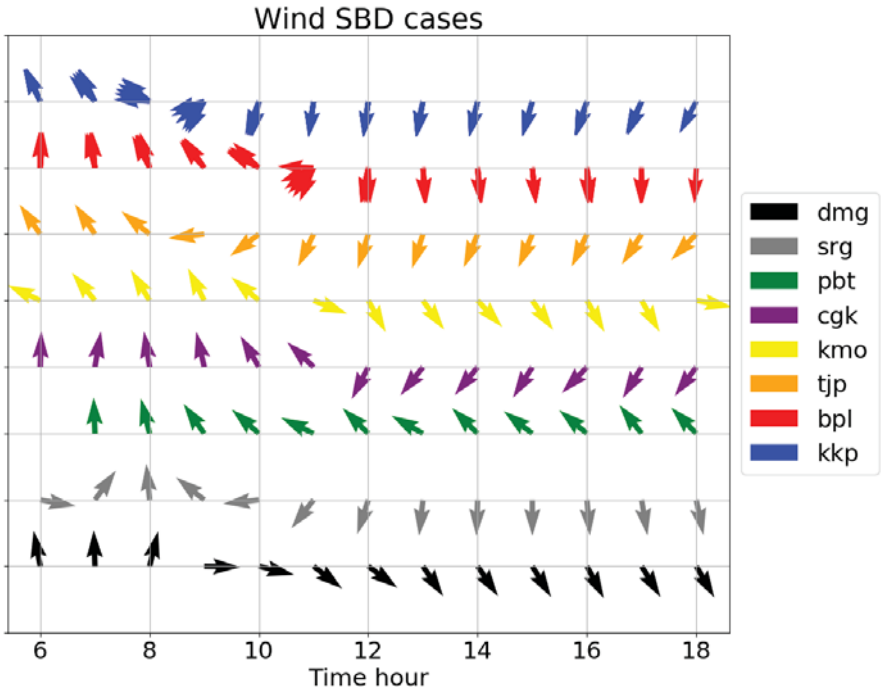

Figure 3.5: Composite of wind at daytime (from 6AM to 6PM) for SBD cases.

And to relate the SBF to the strength of convection, we used the stability z/L parameter measured at the BPL site. This parameter can represent the atmospheric boundary layer (ABL) condition (Stull, 2012). We composited the z/L of 84 SBD cases based on two hours before and after the arrival time of SBF at BPL (Figure 3.6). The condition before the arrival of SBF is more unstable than after arrival. During the day, the convection and ABL mixing process (updraft/down-

draft) actively occurs due to solar heating. When SBF arrives, it suppresses the increasing temperature and ABL becomes well-mixed after the arrival of SBF.

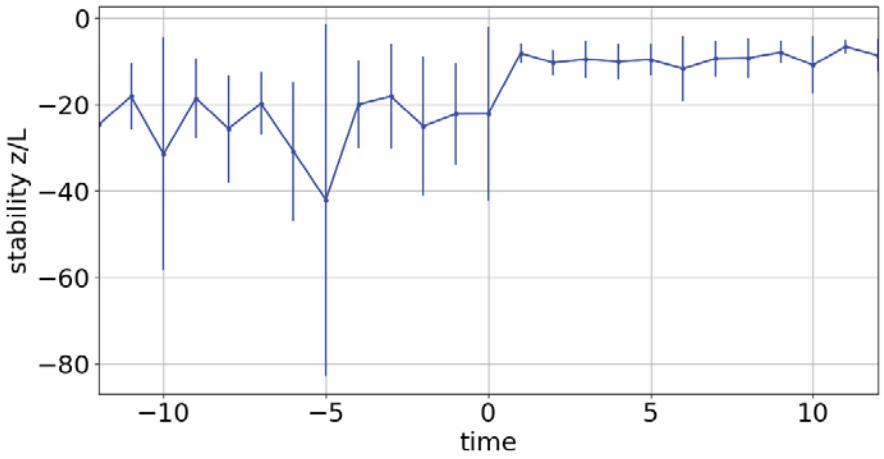

Figure 3.6: The composite of stability z/L parameter (non-dimensional) at 2 hours (120 minutes) before and after arrival of SBF. The x-axis is the time step t of 10-minutes. Time t=0 indicates the arrival time of SBF.

Figure 3.7 shows the composite based on arrival time of the SBF. The composite described the averaged air temperature, specific humidity and wind speed at 2 hours before and 2 hours after the arrival of the SBF. The decreasing of the air temperature at KKP after SBF arrival was larger than BPL. The specific humidity and wind speed increased significantly due to the arrival of the SBF with the larger increasing of wind at KKP was observed.

3.4.2 Cloudiness

Figure 3.9 shows the cloudiness pattern (described as the frequency of occurrence) during SBD (in JAS months, from 2017 to 2018) from 10 AM to 3 PM local time. The cloudy pixels which have an albedo value larger than 0.3 were averaged. The composite was calculated from 102 days of SBD cases. The synoptic condition during JAS months is not so variant for each month. The lower frequency of cloudiness over the sea indicates that most of the sea-breeze circulations formed are closed with the return flow formed aloft and descending flow over the sea about a few kilometers from the coastline.

The occurrence of more than 50 percent cloudiness appeared over the mountainous area and plain area. In the micro-scale perspective, the cloud formation over the mountainous area could be related to orographic effects. While cloudiness over the plain area is due to thermal-induced convection (Figure 3.10). In

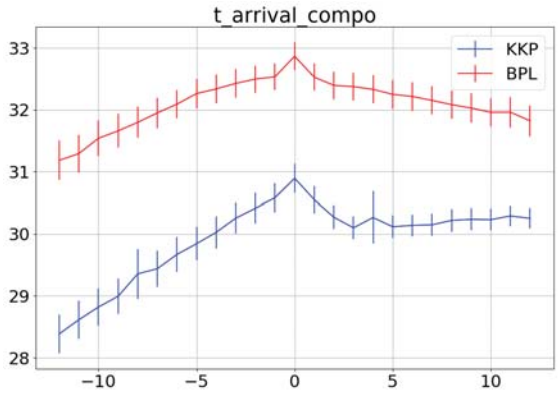

(a) Air temperature [deg C]

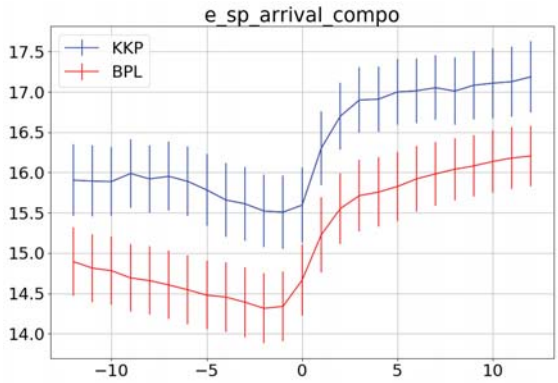

(b) Specific Humidity [g/kg]

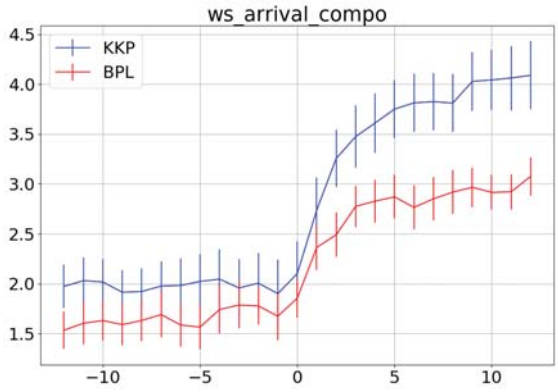

(c) Wind speed [m/s]

Figure 3.7: The composite of air temperature, humidity and wind speed at KKP and BPL site depicted by the blue and red, respectively. The composite time is two hours (120 minutes) before and after the arrival time of the SBF. The x-axis is the time step t of 10 minutes. Time t=0 indicates the arrival time of the SBF. The units of y axis are written in each panel.

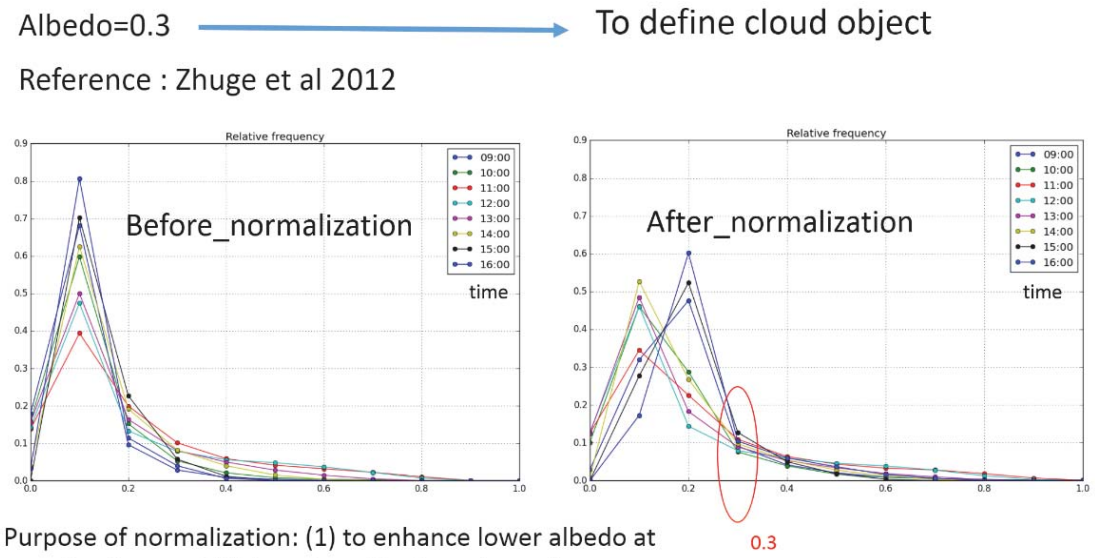

Figure 3.8: Albedo normalization

the western part of Jakarta (red square in Figure 3.10), it shows the spatial distribution of cloud which propagates southward inland. Whereas this movement also exhibits the propagation of SBF lines. Such southward motion did not clearly appear on the eastern side of Jakarta (blue square in Figure 3.10). The cloudiness that formed there was not associated with SBF but more likely to be influenced by Urban Heat Island (UHI, the phenomena due to heating at the urban surface) circulation. Also, the less cloud formation just at the coastline and less enhanced convection at the seaside near the coastline indicated that there was no coastal convergence (i.e., cloudiness that forms due to the slowdown of wind blowing when reaching the land surface, due to friction) occurred during the sea breeze events. There is a high possibility that the cumulus cloud-lines that were formed parallel to the coast over the plain area at the western side of Jakarta were associated with inland penetration of the SBF.

The cloudiness pattern is the composite one and indirectly showing the propagation of the individual cloud system. Which means that in that composite, the cloud systems that propagate and that do not might be composited together. And even though it was also the composite of SBF accompanied by cloud-line and without cloud-line, in mesoscale perspective, we can still see in general the propagation of the cloud system motion which is represented by the propagation of cloud-lines in this cloudiness pattern. Even though the cloud formation and SBF are independent of each other (i.e., the SBF is not necessary to be always followed

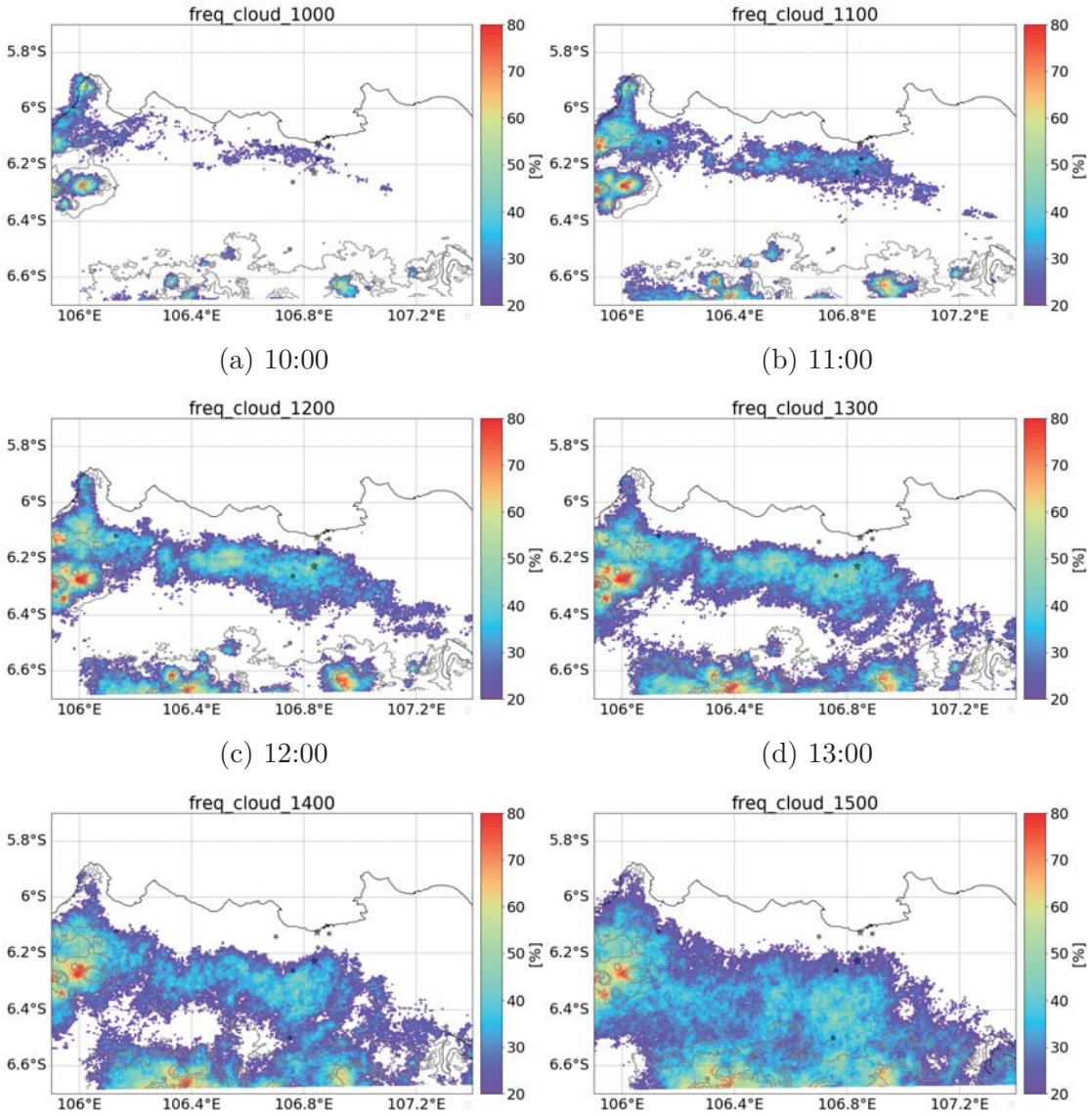

(a) 10:00 (b) 11:00

(c) 12:00 (d) 13:00

(e) 14:00 (f) 15:00

Figure 3.9: The frequency (in percentage) of cloudiness during daytime (10 AM to 3 PM local time) at around Jakarta region. The cloudy pixels are defined as the pixels which are larger than 0.3 of albedo value. The composite was calculated for 102 days of the screened SBDs. The occurrence of more than 50 percent cloudiness exhibits the southward propagation of sea-breeze front lines. The topography contours (grey line) are plotted at 200, 600 and 800 m. (After Ferdiansyah et al., 2020)

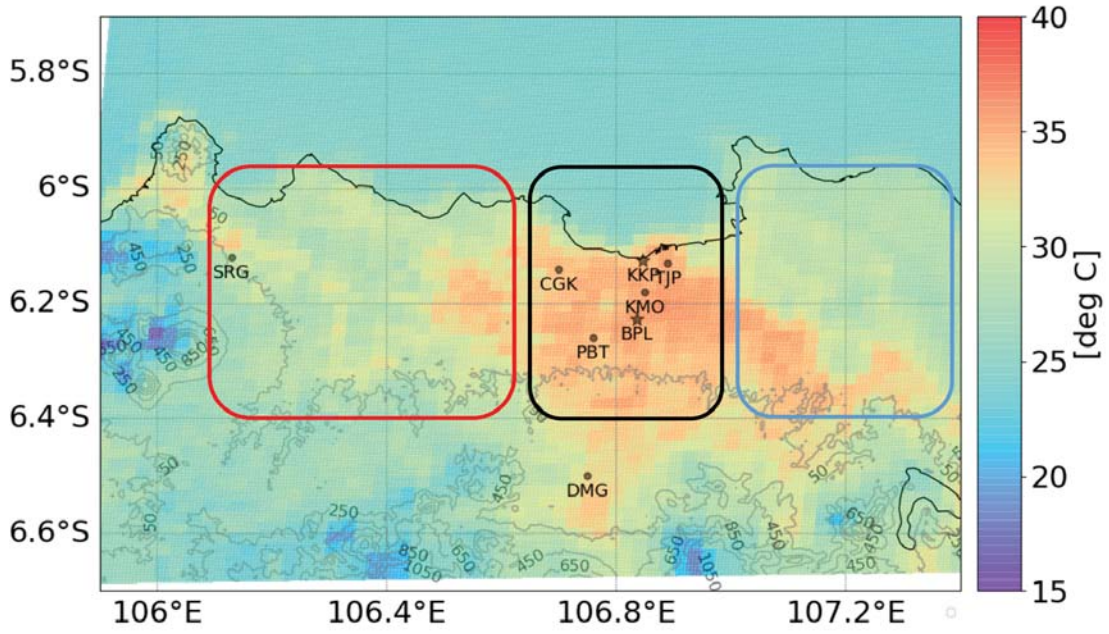

Figure 3.10: Spatial distribution of surface temperature (clear-sky brightness temperature, in degree Celsius) represented by a composite of B13 images at 12:00 local time. The topography contours (grey line) are plotted with a 200 m interval from 50 to 1050 m. Suburban, urban, and suburban where non-SBF-associated cloudiness are indicated by red, black and blue rectangles, respectively. (After Ferdiansyah et al., 2020)

by the cloud formation), we can confirm that cloud-lines propagation can be used as a proxy of the propagation of sea breeze front lines. Moreover, table 3.2 and 3.3 show the wind direction at six meteorological stations and two observation sites in the study area, during the daytime (from 9:00 to 15:00) and nighttime (from 21:00 to 03:00) in JAS months local time. The dominant wind in the entire region is northerly. The prevailing synoptic wind during this season is easterly. The sea breeze propagates almost from north to south even under the condition of easterly synoptic wind.

Table 3.2: Mean value of temperature (t), specific humidity (q), wind speed (ws) and direction (wd) during July-August-September (JAS) season, 2015 to 2018, calculated from meteorological station data.

station	**month**	**time**	**t** (^oC)	**q** (gkg^{-1})	**ws** (ms^{-1})	**wd**
TJP	7	day	31.06	16.62	2.34	NNE
		night	27.76	17.4	0.85	E
	8	day	30.93	16.62	2.86	NNE
		night	27.68	17.85	0.93	ESE
	9	day	31.6	17.11	3.16	NNE
		night	27.93	17.67	0.83	ESE
CGK	7	day	30.99	17.3	2.87	NE
		night	25.77	17.75	1.42	S
	8	day	31.04	16.5	3.71	NE
		night	26.18	17.2	1.74	SE
	9	day	31.35	16.65	3.8	NE
		night	25.76	16.94	1.58	S
KMO	7	day	31.09	17.69	2.35	NE
		night	27.46	18.15	0.26	SE
	8	day	30.93	17	2.55	NE
		night	27.52	17.8	0.38	ESE
	9	day	31.28	17.07	2.62	NNE
		night	27.49	17.59	0.29	SE
PBT	7	day	31.4	17.86	1.73	ESE
	8	day	31.57	17.15	1.81	ESE
	9	day	32.03	17.25	1.97	ESE
SRG	7	day	30.71	18.13	1.77	NNE
		night	25.15	18.01	0.08	S
	8	day	30.95	17.63	2.06	NNE
		night	25.37	17.79	0.06	SSE
	9	day	31.44	17.51	2.28	NNE

Continued on next page

Table 3.2 – *Continued from previous page*

station	**month**	**time**	**t** (^oC)	**q** (gkg^{-1})	**ws** (ms^{-1})	**wd**
		night	25.37	17.6	0.08	SSW
DMG	7	day	30.11	16.81	2.21	NNW
		night	24.59	17.16	0.27	NE
	8	day	30.21	16.36	2.51	NNW
		night	24.69	16.61	0.37	SE
	9	day	30.66	16.36	2.72	NNW
		night	24.63	16.97	0.56	SSE

Table 3.3: Mean value of temperature (t), specific humidity (q), wind speed (ws) and direction (wd) during July-August-September (JAS) season, 2016 to 2018, calculated from observation point data

station	month	time	t (^oC)	q (gkg^{-1})	ws (ms^{-1})	wd
KKP	7	day	30.13	16.76	2.72	NNE
		night	27.27	17.18	0.75	SE
	8	day	30.27	16.33	3.58	NNE
		night	27.32	17.08	1.13	ESE
	9	day	30.74	16.57	3.39	NE
		night	27.66	16.87	4.95	SE
BPL	7	day	31.3	15.25	0.76	NNE
		night	27.0	16.24	0.8	S
	8	day	31.53	14.89	1.13	NNE
		night	27.12	15.99	1.04	SSE
	9	day	31.95	15.13	1.26	NNE
		night	27.26	16.32	0.85	S

3.5 Summary

This chapter presents the result of screening procedure based on the defined criteria of sea-breeze day using the ground observation data at KKP and BPL site that be verified by analyzing the composite of the air temperature, specific humidity and wind on the sea-breeze day and non-sea-breeze day. The cooling effect of the sea breeze was more prominent at KKP due to closer location to the coastline. The spatial distribution of the typical cloudiness during the sea-breeze days is also discussed based the albedo composite. The results shows that there are two regions, one that exhibited the cloudiness pattern that was associated with sea-

breeze front activity and another one that exhibited more likely related to ordinary thermal convection and urban-heat island circulation

Chapter 4

Inland Penetration Detection of Sea-breeze Front

4.1 Introduction

In this chapter we present the procedure of inland penetration detection of the sea-breeze front (SBF) by using the visible band (band B03) of time-sequential Himawari-8 images. The spatial information of inland penetration is retrieved by tracing the time evolution of cumulus cloud-lines that formed in the vicinity of the sea-breeze front. The cloud-line provides the detectable feature for tracking the front propagation.

In the validation step, we evaluate the passage time of the detected cloud-line with the arrival time of SBF obtained from observation data at KKP and BPL site (Figure 4.1). And in the post-processing step, the results then further analyzed to estimate the penetration distance and speed of the SBF. We utilized the prevailing wind from ERA-Interim re-analysis data (Dee et al., 2011) and radiosonde observation at CGK airport (Figure 4.1) to consider the background synoptic-condition for each sea-breeze event in further analysis. And even though we use only two observation site for validation and analysis of inland propagation of SBF, from previous studies concerning about SBF propagation, the spatial pattern or horizontal structure of SBF does not really depend to the local effect of the surface beneath it but more to the mesoscale or synoptic influence.

The edge detection algorithm can be applied to textured feature such as cumulus cloud image. The parsed distribution of the cumulus-cloud appears as texture in 2 dimensional image. Too parsed distribution of the cumulus pixels in the image might be difficult to be delineated. But in that case, we can smooth the image using e.g., Gaussian function (Figure 4.2). The snakes algorithm is a state of the art method that widely applied in computer vision for edge detection. The evolution

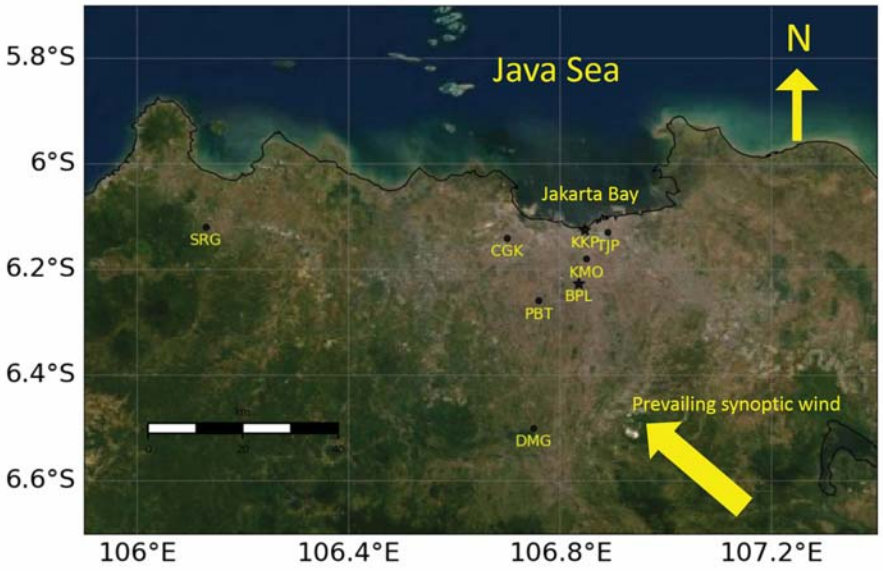

(a) Urbanized area around Jakarta City

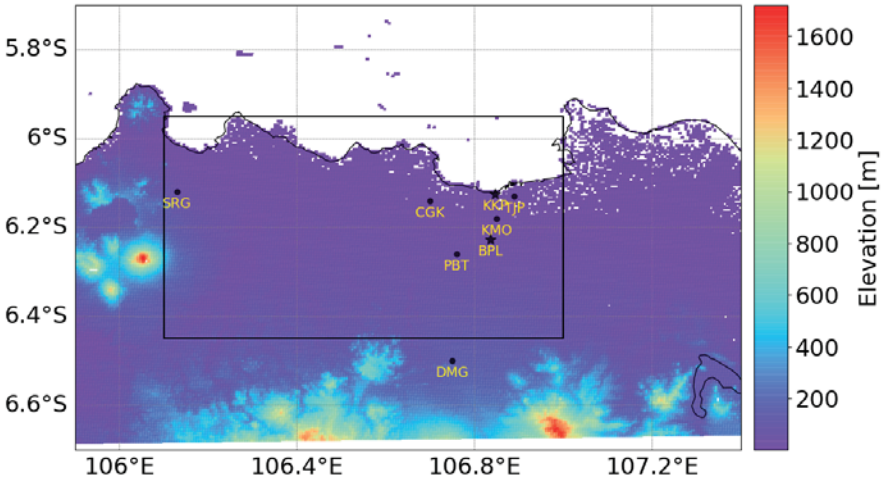

(b) Topography (unit in meter)

Figure 4.1: The study area. The square in topography map of 4.1b depicts the urbanized area around Jakarta City and the less-urbanized area (suburban) in its western side. (After Ferdiansyah et al., 2020)

of the conventional snake-models mostly contain the partial-differential equations (PDE). And this PDE approach is necessary to be solved mathematically, which somehow requires high computational issues.

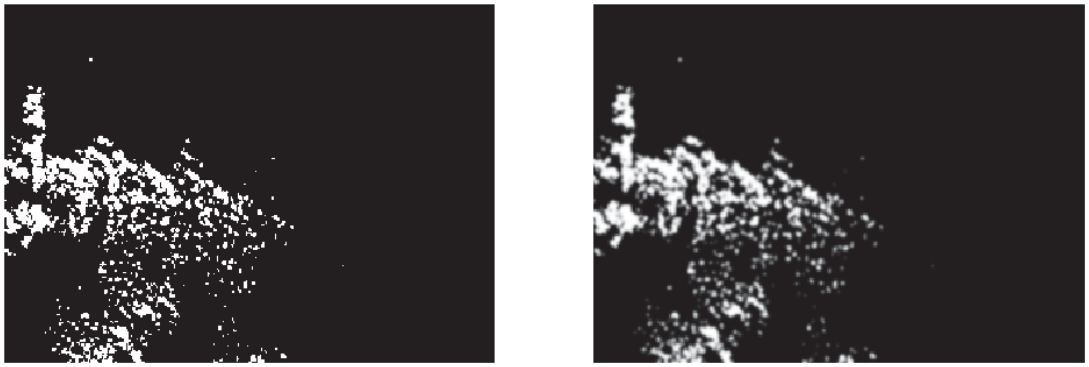

Figure 4.2: Binary image of Himawari-8 Band B03 image. White indicates the cumulus-cloud pixels. (Left) is the original image and (Right) is the smoothed image using Gaussian function.

In improving that computation issue of the snake algorithm Marquez-Neila et al. (2014) proposed the morphological-snake algorithm. In this method, the snake equations are solved by a morphological operator (dilation and erosion) which does not require complicated numerical computation. The algorithm is more straightforward in dealing with the binary images in multi-dimension. Also, the re-initialization of the level-set is not required. Therefore, the simple and fast detection process might be possible. To the best of our knowledge, this method has not been applied yet into geo-referenced meteorological satellite images such as for detecting the cloud-lines associated with SBF.

4.2 Morphological Snake Algorithm

In morphological snake (Marquez-Neila et al. (2014)), instead of using a differential operator, morphological operators are used to solving the differential equations. In this study, we used the ACWE functional version of the morphological snake.

As previously mentioned in Chapter 2, in ACWE model, it is not necessary to define the $g(I)$ parameter and the term with ν parameter is also optional. So, the parameter set up for ACWE is easier. Moreover, compared to GAC the energy function during iteration can decrease steadily with no oscillation (Marquez-Neila et al. (2014)).

The algorithm for morphological ACWE is as follows. The level-set u is defined and the time evolution for each n^{th} iteration can be performed by following three

steps:

$$u^{n+\frac{1}{3}}(x) = \begin{cases} (Du^n)(x), & \text{if } \nu > 0 \\ (Eu^n)(x), & \text{if } \nu < 0 \\ u^n(x), & \text{otherwise} \end{cases}$$

$$u^{n+\frac{2}{3}}(x) = \begin{cases} 1, & \text{if} |\nabla u^{n+\frac{1}{3}}|(\lambda_1(I-c_1)^2 - \lambda_2(I-c_2)^2)(x) < 0 \\ 0, & \text{if} |\nabla u^{n+\frac{1}{3}}|(\lambda_1(I-c_1)^2 - \lambda_2(I-c_2)^2)(x) > 0 \\ u^{n+\frac{1}{3}}, & \text{otherwise} \end{cases} \tag{4.1}$$

$$u^{n+1}(x) = \left((SI \circ IS)^{\mu} u^{n+\frac{2}{3}}\right)(x)$$

Where I is the image's pixel value; μ, ν, λ_1 and λ_2 are positive constants (the values we set are 1, 0, 1 and 1 respectively); (SI $\circ$ IS) is the discrete morphological operator-defined based on dilation (D) and erosion (E) operator; and c_1 and c_2 are the contours inside and outside the targeted object, respectively. The implementation of the morphological operators in Equation 4.1 is listed in Table 4.1.

Table 4.1: Morphological operator for 2-D array

Operator	Implementation
(1) Dilation, D	$u^{n+1}(i,j) = \max_{\Delta i, \Delta j \in \{-1,0,1\}} u^n(i+\Delta i, j+\Delta j)$
(2) Erosion, E	$u^{n+1}(i,j) = \min_{\Delta i, \Delta j \in \{-1,0,1\}} u^n(i+\Delta i, j+\Delta j)$
(3) Curvature, $SI \circ IS$	Composition, apply IS first and then SI
$\inf\sup, IS$	$\min_{P \in B} \max_{(\Delta i, \Delta j) \in B} u^n(i+\Delta i, j+\Delta j)$
$\sup\inf, SI$	$\max_{P \in B} \min_{(\Delta i, \Delta j) \in B} u^n(i+\Delta i, j+\Delta j)$
Gradient, ∇	(u_x, u_y)
first derivative, u_x	$u_x(i,j) = \frac{1}{2}(u(i+1,j) - u(i-1,j))$
u_y	$u_y(i,j) = \frac{1}{2}(u(i,j+1) - u(i,j-1))$

B-criteria used in $SI \circ IS$ operator is the structural element of the border. We use four P-positions of 3x3 array operator to define the border as depicted in red boxes of Figure 4.3. The SI operator will work on the 1-pixels (inside-contour) and the IS will work on the 0-pixels (outside-contour). When the array operators find the edge/border (indicated as red dashed line in Figure 4.3), the center pixels will keep their values, but if they do not find the border, the center pixels will be replaced into 0 for inside-contour and into 1 for outside-contour pixels.

The Snake algorithm calculated with morphological approach is about 9∼10 times faster than that with PDE approach (Figure 4.4). Table 4.2 shows the comparison of the estimated computation time for Jakarta (total image: 1476) and Tokyo (total image: 1188). The time showed is the time required for detection the cloud-line in the 320x220 grid pixel of satellite image.

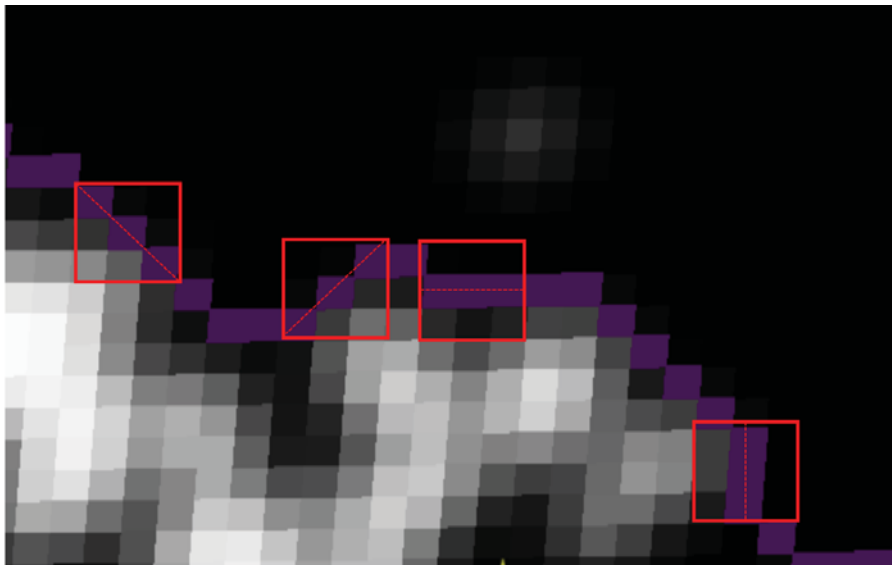

Figure 4.3: The border-criteria B used for implementation of $SI \circ IS$ operator (Table 4.1). Gray-scaled color pixels of the image are the clouds, purple color pixels indicate the detected cloud-line, the dashed red line in the red boxes (3x3 arrays) are representing the four positions P of structure element of B. (After Ferdiansyah et al., 2020)

Table 4.2: Required time to detect the cloud-line on the 320 x 220 pixel grid of satellite-image. Comparison between computation using PDE-snake (with wavelet as potential function of Corpetti and Planchon (2011) and Morphological-snake.

Algorithm	time per image	Jakarta analysis	Tokyo analysis
PDE-snake	170 s	∼69 hour	∼56 hour
Morph-snake	20 s	∼8 hour	∼7 hour

4.3 Results

In this study, the albedo more than 0.3 is set to be 1 (inside the snake contour) and 0 (outside the snake contour) for the other pixels to create the binary image for

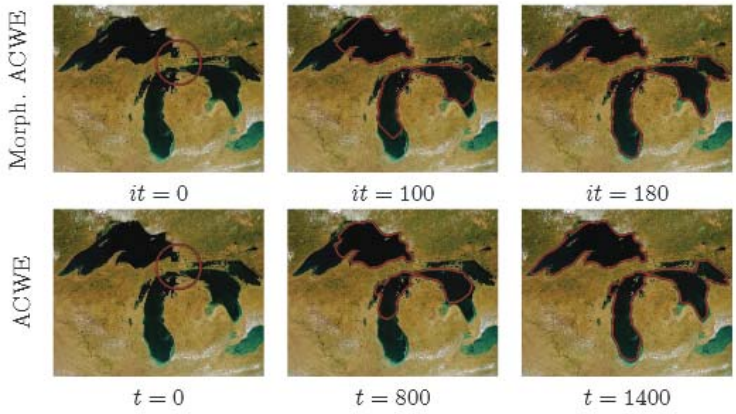

Figure 4.4: Comparison of computation time between PDE snake and morphological snake. Source: Marquez-Neila et al. (2014)

defining the level set. Selecting too high albedo value (such as 0.4∼) will lead to only extracting the mature and thick cumulus cloud. On the other hand, selecting too low value (such as ∼0.2) will lead to include the thin-cirrus and non-cloud object.

Despite this threshold selection, the snake ability of cloud-line detection is not strictly sensitive with this 0.3 threshold value. Figure 4.5 reveals the sensitivity tests with several threshold-values around the lower range of albedo for cloud-object determination, i.e., 0.25-0.35 (Taniguchi et al. (2001)). The standard deviation of the distance of the detected cloud-line to BPL site was about 0.5 km (1 pixel). This suggests that the albedo selection within the lower-range value (0.25-0.35) will not impact significantly the ability of the detection.

4.3.1 Cloud-line detection

Among 84 days of the SBF cases, 53 cases are the SBFs accompanied by cloud-lines. We then applied the morphological snake algorithm to these cases. Figure 4.6 shows an example of how the arrival time of SBF estimated from ground observation data (arrival time) and the passage time based on the detected cloud-line from satellite images (passage time). Based on the appearance of the cloud-line, it was confirmed that the onset time near the coast occurs between 9-10 AM. The cloud-line then started to form in a long structure parallel to the coastline and propagates southward. It is also important to note that in some cases, there were also some cases when the arrival time was not be able to be identified clearly (Figure 4.7 and Figure 4.8. For those cases, the nearest time of the timing of increasing humidity to the timing of decreasing temperature was taken as the

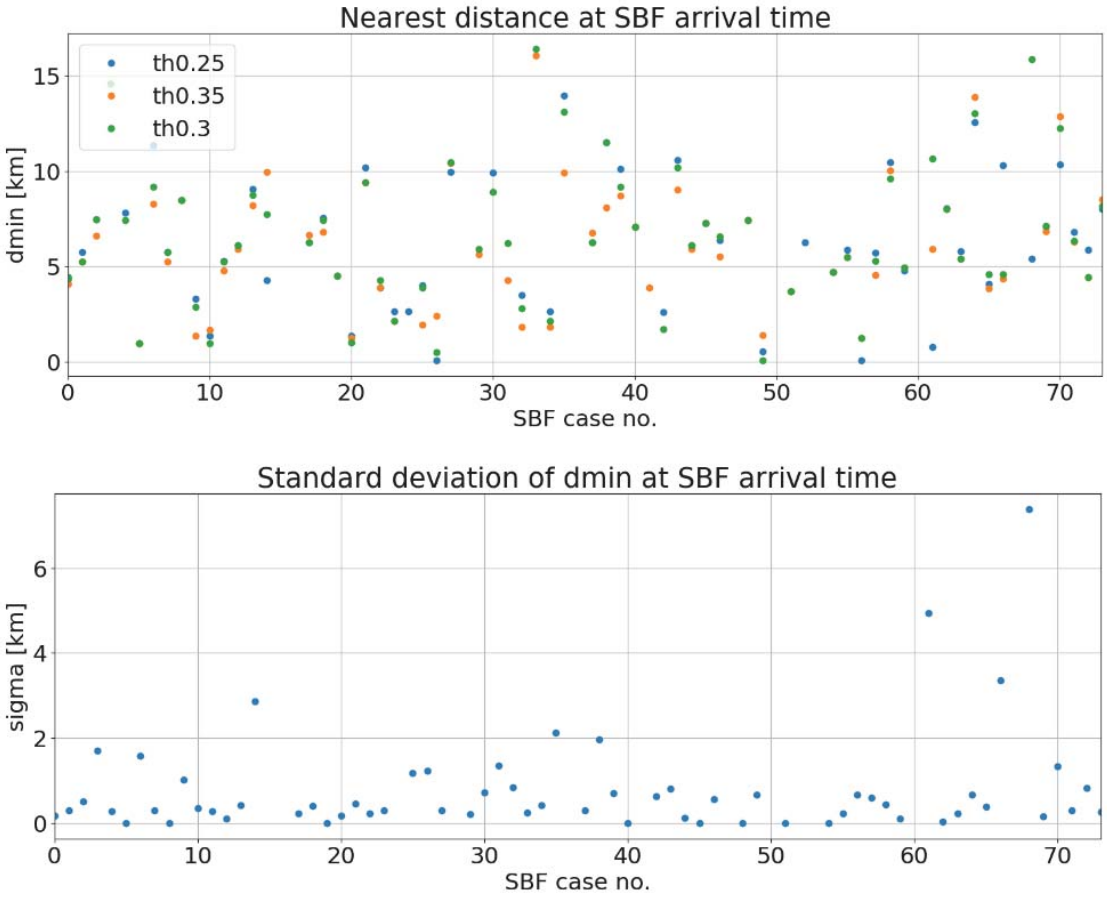

Figure 4.5: Sensitivity test for albedo-threshold selection against the cloudline distance to BPL site.

arrival time of the SBF and the satellite images at that timing was also visually judged.

The mean arrival time of SBF was 10:30 and 13:00 for KKP and BPL, respectively. We validated the passage time of the cloud-line with the arrival time of SBF. Figure 4.18 shows the composite of the cloud-line location based on the arrival time of SBF. For an arrival time at KKP, there are 13 days which were undetected (no cloudy pixels yet), and 40 days which were almost the same with the passage time (KKP "match"). The undetected cloud-lines at KKP are likely due to still not sufficient of the moisture so the cloud was not formed. Another reason is the cloud pixels still too parsed, so the snake algorithm did not delineate it yet as the edge. In that case, we confirmed also the distribution of the cloudy pixels at the original B03 image, whether the passage time can be estimated or not. For an arrival time at BPL, there are 4 days which were undetected (due to irregular cloudiness and higher-level cloud contamination), 24 days which are almost same passage (BPL "match"), and 25 days of the later passage than the arrival time of SBF (BPL "delay"). Since the delay was exhibited by the entire cloud-line spatially, the reason for this later passage is likely due to synoptic condition for both groups were different. It is important to analyze further what kind of synoptic condition between these two groups.

We composed the 00 UTC (7 AM local time) wind profile from radiosonde observation at CGK to know the synoptic condition for each "match" and "delay" group (grey arrows in Figure 4.18b and 4.18c). Since we focused on the cloud propagation, we compared the lower (100 - 1500 m) and the upper (1500 - 3000 m) level of the atmospheric boundary layer (ABL). For the "match" group, the wind at lower ABL was offshore and at upper ABL was an onshore direction. While both for the lower and upper ABL of the "delay" group are an offshore direction. Also, the offshore wind at an upper level of the "delay" is stronger than the onshore wind speed at the same level as the "match" group. Moreover, from the composite of the wind (black arrows in Figure 4.18b and 4.18c) using the 00 UTC of re-analysis data at level 700 hPa (3000 m), we confirmed that the opposing flow of the prevailing synoptic wind condition for the "delay" was stronger than that of the "match" group. This indicated that the opposing and stronger flow of upper-level synoptic wind prevents the propagation of the cloud-line in general, hence it causes the later passage time of cloud-line than the arrival time of SBF for the "delay" group.

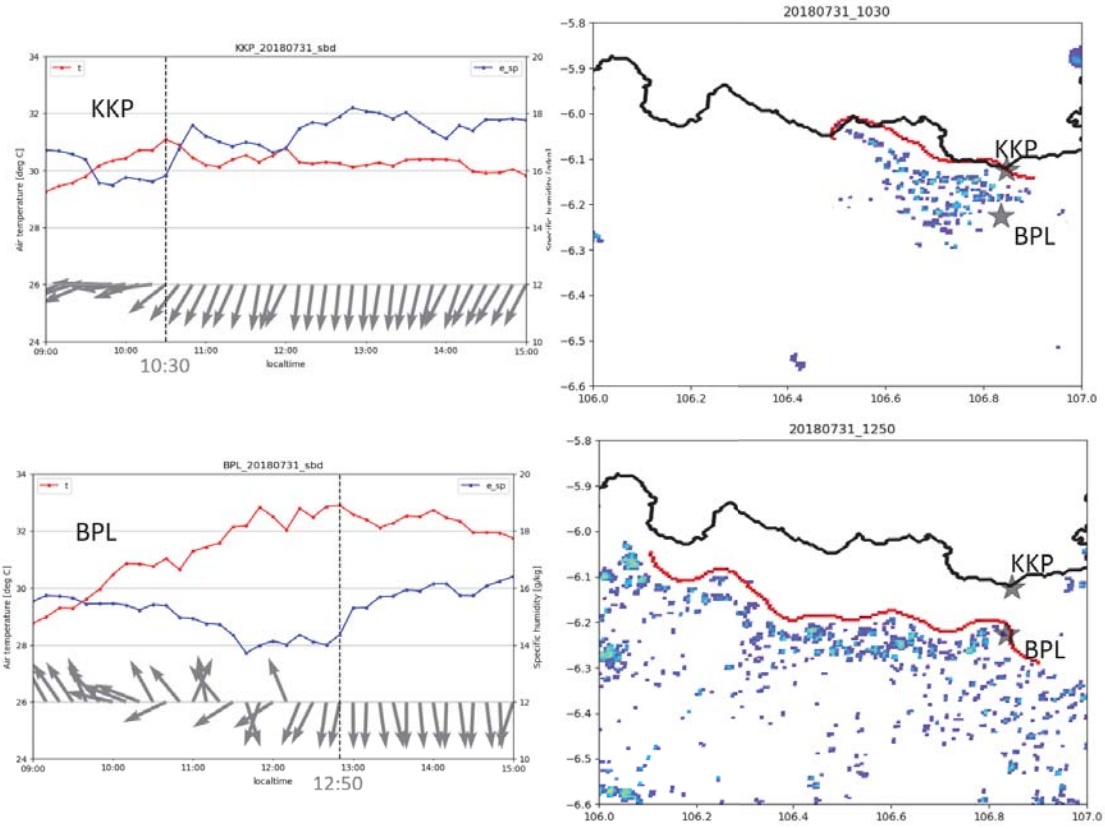

Figure 4.6: The arrival time of the sea-breeze front estimated from observation data (left panels, grey dot-line) and the passage time of cloud-lines from satellite images (right panels, red line). (After Ferdiansyah et al., 2020)

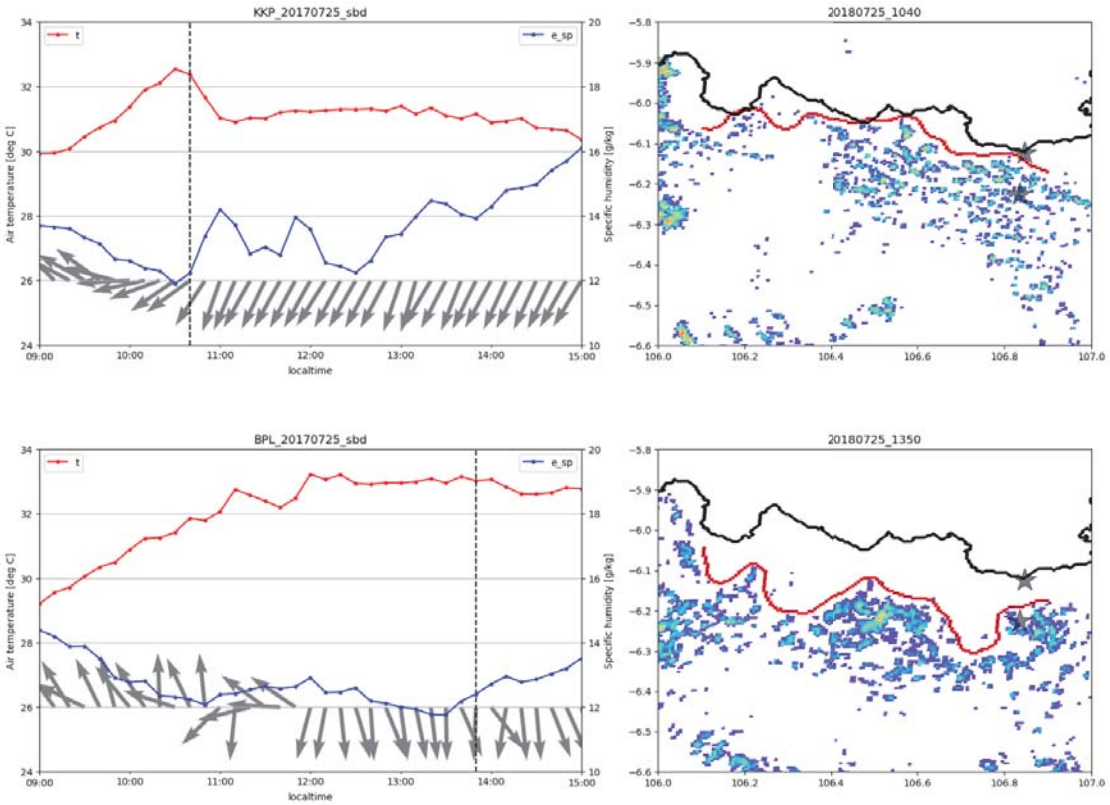

Figure 4.7: Example of case when the arrival time can be identified clearly at KKP but not at BPL.

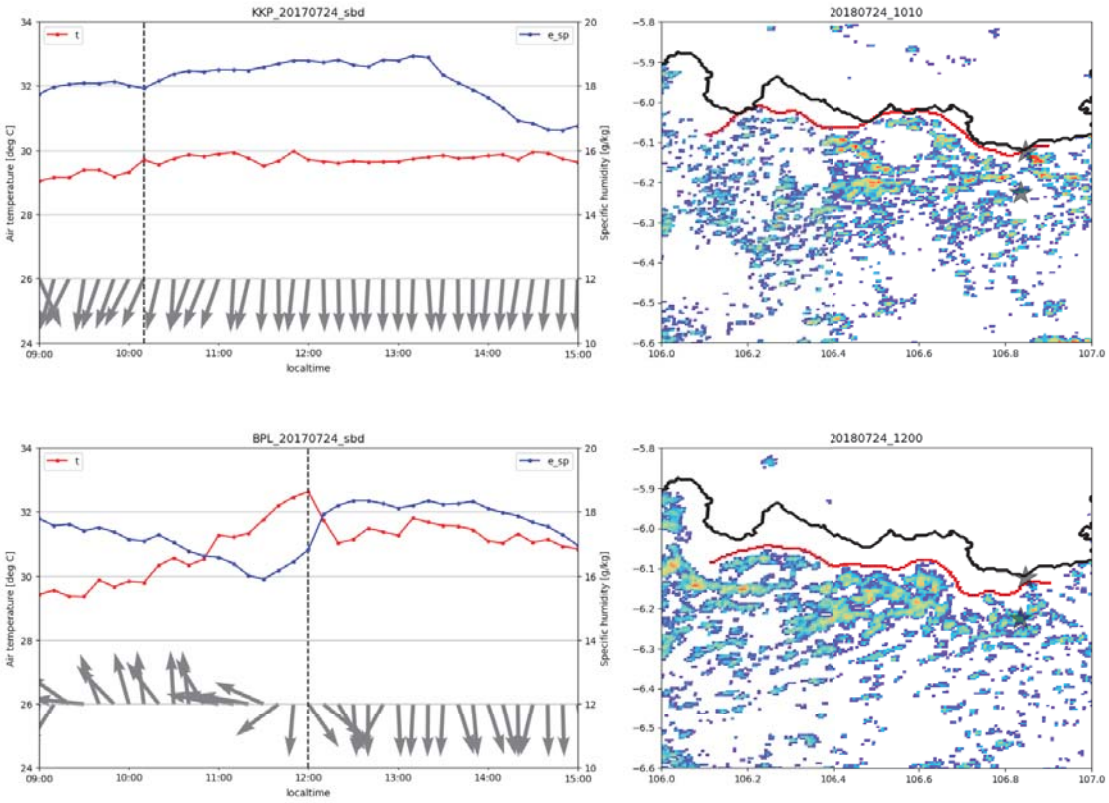

Figure 4.8: Example of case when the arrival time can be identified clearly at BPL but not at KKP.

4.3.2 Arrival time and penetration speed of the sea-breeze front

Figure 4.9a shows the scatter plot of the arrival time of the SBF and passage time of the cloud-line. In general, the arrival time agreed well with the passage time with the correlation coefficient of more than 0.7 for both arrivals at KKP and BPL. The bias time was about 20 minutes. The location of the cloud-line when the SBF arrived at BPL varied from 0 to 10 km. The mean distance range for the "match" group was less than 3 km, while that for the "delay" group was more than 5 km.

Based on the arrival time at KKP and BPL, when we assumed that the SBF reached the KKP and BPL, we can estimate the penetration speed of SBF. Figure 4.9b depicts the penetration speed estimated from observation data and the cloud-lines passage with the correlation coefficient of more than 0.6. The inland penetration speed was found to be in the range 1.2 to 2.4 ms^{-1} with the average speed of 1.5 ms^{-1}, and from the passage time of the cloud-line was 1.4 ms^{-1}, slightly slower than that estimated from the arrival time of SBF. The "delay" group indicated slower penetration speed than the speed estimated from the arrival time of SBF.

4.3.3 Sea breeze front speed and wind speed evaluation

Regarding the wind speed of sea breeze, Mathews (1982) proposed the forecast rule using the regression relationship between wind speed of sea breeze (U) and the land-sea temperature difference (ΔT):

$$|U| = \frac{1}{2}\sqrt{\Delta T} \tag{4.2}$$

Simpson (1969) adapted the above forecast into the atmospheric front and Simpson and Britter (1980) modified the equation into:

$$u_{front} \approx 0.87u_{SB} - 0.59u_g \tag{4.3}$$

As can be confirmed from Equation 4.3 that the SBF will penetrate faster when wind speed (see breeze) increases. And the opposing flow of the prevailing wind will slow the front penetration.

Figure 4.10 shows the scatter plot of the wind speed at BPL (the reference site selected as the affected area by sea breeze from Jakarta Bay) and the sea-breeze penetration speed derived from observation. The front speed and the wind speed have the positive relationship as predicted in the Eq. 4.3.

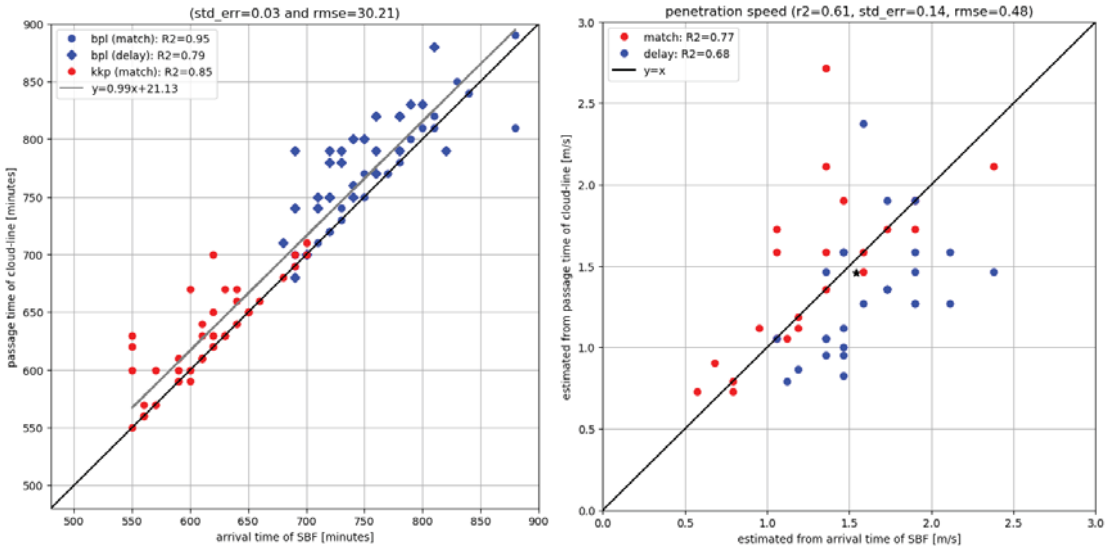

(a) Arrival time (b) Penetration speed

Figure 4.9: Comparison between arrival time of SBF and passage time of cloud-line. Red and blue dots in 4.9a indicate the arrival time at KKP and BPL, respectively. The grey solid line in 4.9a depicts the linear regression equation with interception is about 40 minutes. The black lines showing $y = x$ line are drawn in 4.9a and 4.9b and the black star in 4.9b depicts the mean penetration speed (in ms^{-1}). (After Ferdiansyah et al., 2020)

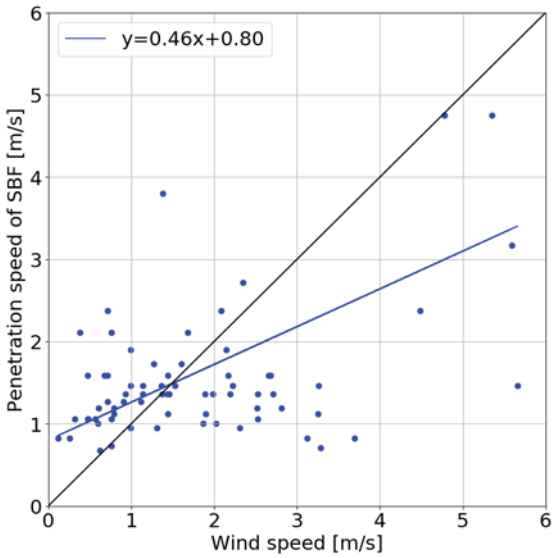

Figure 4.10: Comparison between SBF penetration speed and wind speed after sea breeze arrival at BPL site.

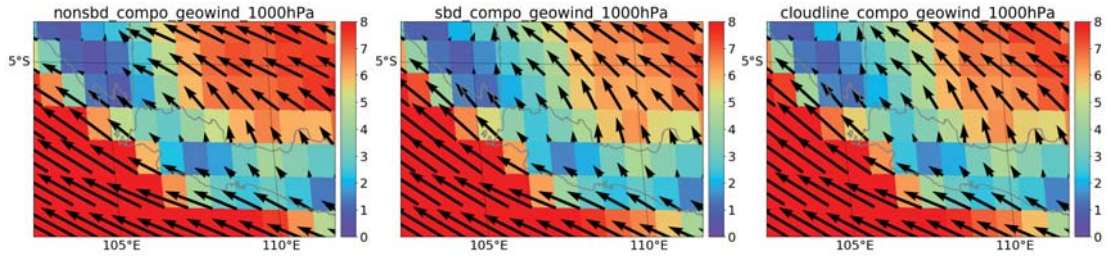

(a) Non SBD (b) SBD (c) Cloudline

Figure 4.11: Composite of the ERA-interim wind (1000 hPa level, 00 UTC). Shaded color depicts the wind speed in m/s.

4.3.4 Synoptic condition during sea-breeze days

Jakarta is located in tropics, the region where the synoptic prevailing wind mostly is influenced by the seasonal or monsoonal wind. The daily synoptic wind pattern does not vary day by day. This can be confirmed from the composite of ERA-interim wind at 1000hPa shown in Figure 4.11 and Figure 4.12. For both 00UTC (morning) and 06UTC (afternoon), no siginificant difference between the non-SBD, SBD and cloudline cases. However, as can be seen in Figure 4.13 that the zonal wind (u-component) for non-SBD cases was wider range (from -6 to 2 m/s) than SBD cases (from -4 to 2 m/s). And the meridional wind (v-component) for non-SBD cases was from 1 to 7 m/s and for SBD cases was from 1 to 5 m/s. The results indicated the slightly weaker prevailing for SBD cases than non-SBD cases which dominantly attributed by both zonal and meridional wind.

The vertical profile of the zonal and meridional wind are shon in Figure 4.14 to Figure 4.16. The figures show the vertical wind profile within ABL (from 1000hPa to 700hPa level) for non-SBD, SBD and cloudline cases. The average zonal wind within ABL was larger for non-SBD than SBD (and cloudline) cases (Figure 4.14). And for meridional wind, no direction change in the entire ABL for non-SBD cases (Figure 4.15), while there was a shift for SBD (and cloudline). The meridional wind in afternoon was negative (southward direction) in lower part of ABL and positive (northward direction) at upper part of ABL (Figure 4.15).

Next is how is the influence of the synoptic wind to the SBF penetration speed? As can be seen in Figure 4.9b and Figure 4.10 that the SBF penetration speed obtained from the result vary from 0.6 to 2.7 m/s. However, this variation could not be attributed to the speed of the prevailing synoptic wind, since no significant correlation between them (Figure 4.17). This indicated that the SBF penetration speed in Jakarta was more likely to be influenced by the local variation such as the temperature gradient between sea and land surface.

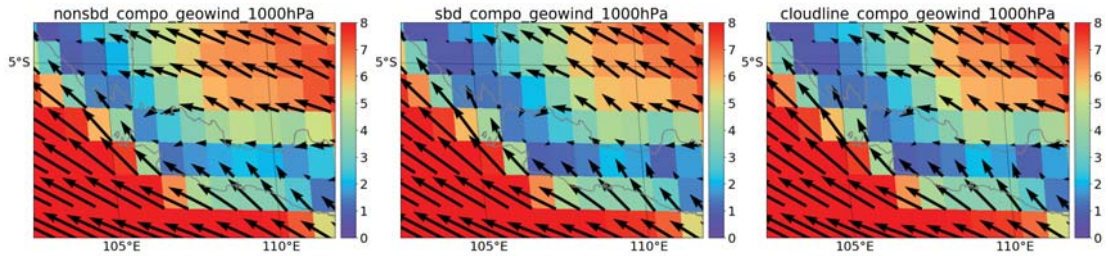

(a) Non SBD (b) SBD (c) Cloudline

Figure 4.12: As same as Figure 4.11 but for 06UTC (3PM).

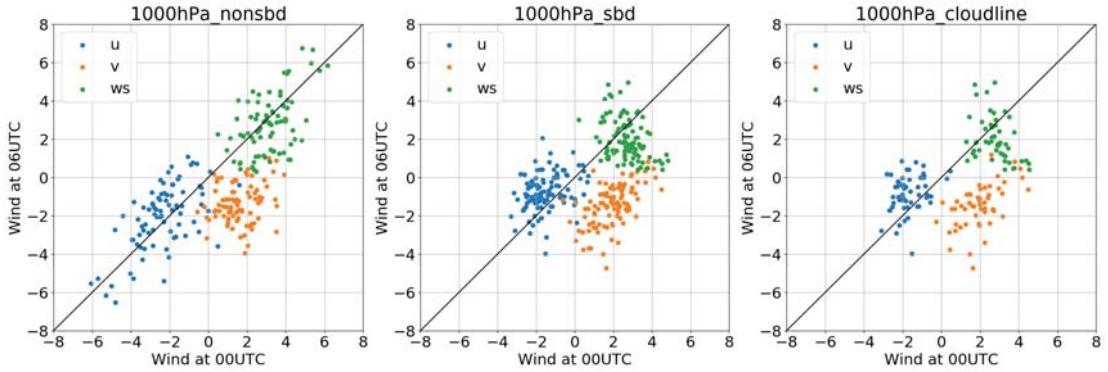

(a) Non SBD (b) SBD (c) Cloudline

Figure 4.13: Scatter plot of the ERA-interim wind at 1000hPa. The comparison between 00UTC (9AM) and 06UTC (3PM) wind.

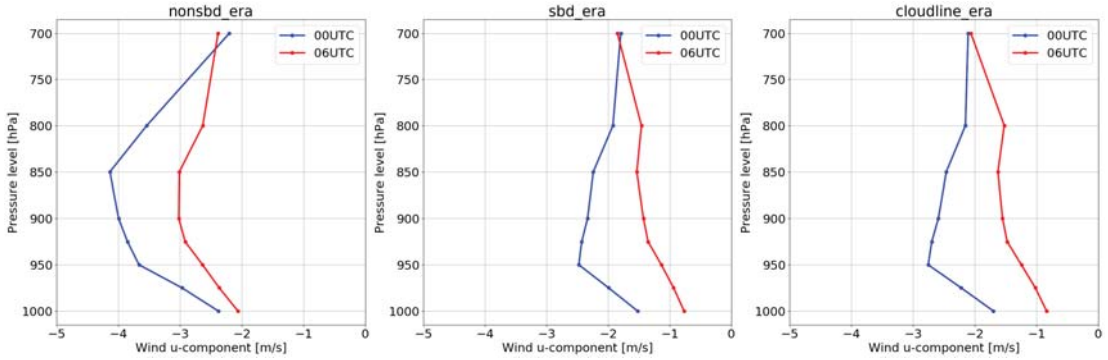

(a) Non SBD (b) SBD (c) Cloudline

Figure 4.14: The composite of Vertical profile of ERA-interim wind within ABL (from 1000hPa to 700hPA level) at 9AM and 3PM.

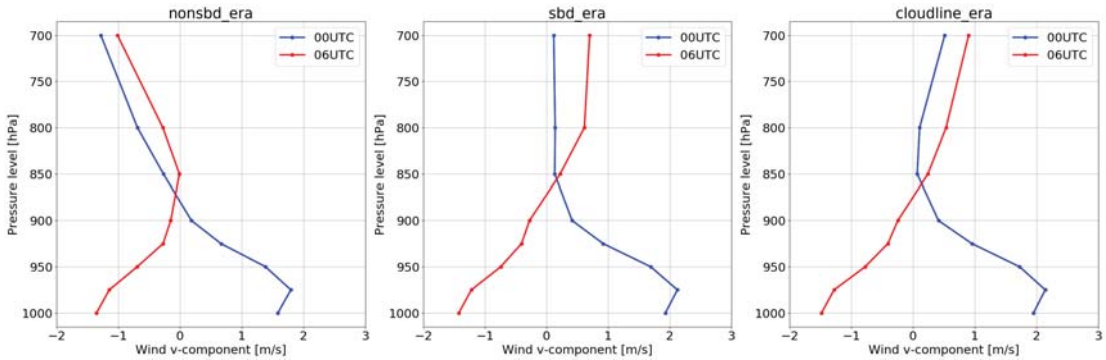

(a) Non SBD (b) SBD (c) Cloudline

Figure 4.15: As same as Figure 4.14 but for v-component

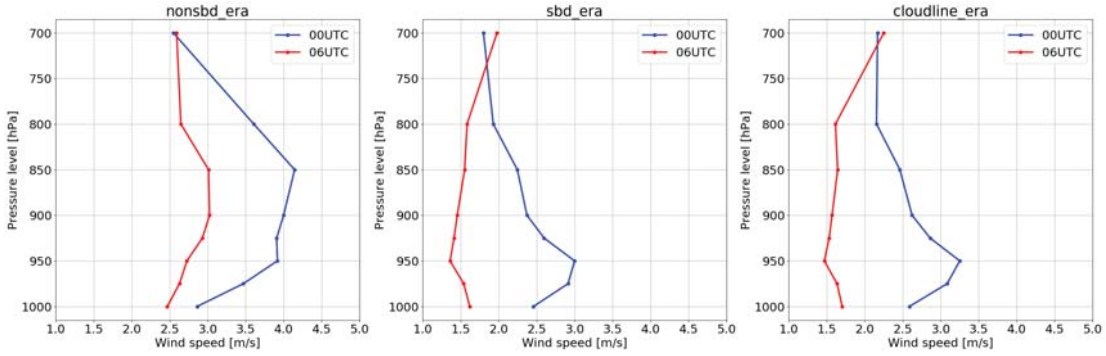

(a) Non SBD (b) SBD (c) Cloudline

Figure 4.16: As same as Figure 4.14 but for wind speed

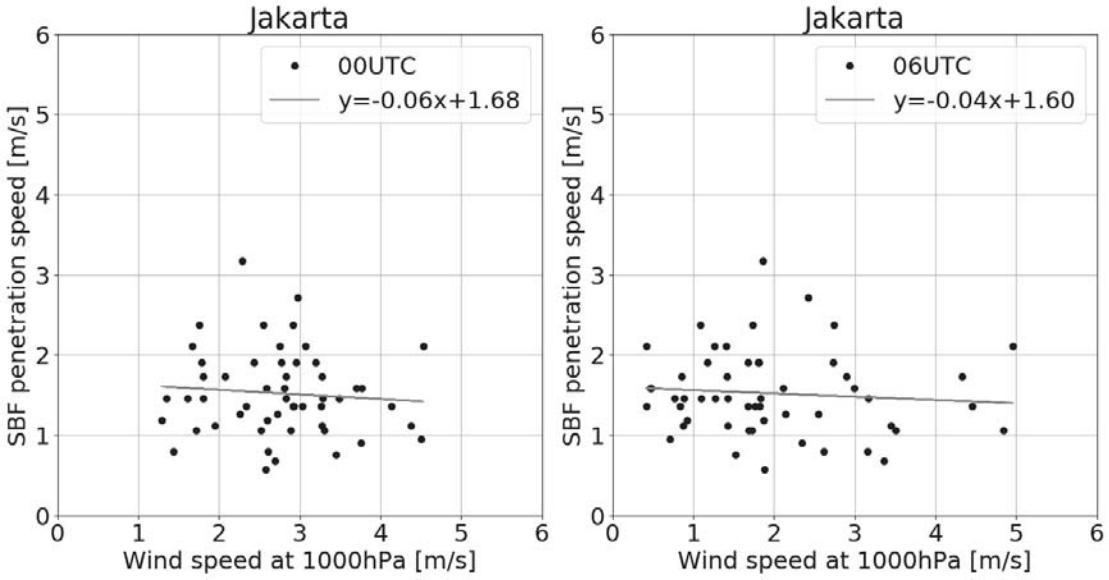

(a) ufront 00UTC (b) ufront 06UTC

Figure 4.17: The comparison between SBF penetration speed and the ERA-interim wind at 1000hPa level (Grid pixel location: BPL site).

4.3.5 Spatial distribution of inland penetration

Finally, from each cloud-lines, we then derive the spatial distribution for the hourly mean of sea-breeze front arrival time (Figure 4.19). All the time is presented in local time (Western Indonesia Standard Time). The map of sea-breeze arrival time shows the spatial distribution of penetration distance and speed. We can confirm that the arrival time of the SBF line is the same for SRG and KMO (arrival time at 12:00 and 13:00 for the "match" and the "delay" group, respectively). The distance from the coast is 10 km and 6 km, for SRG and KMO, respectively. This indicated that the sea-breeze front penetrated slower in the city. Also, Hadi et al. (2000) reported that the sea-breeze arrival time at Serpong (about 10 km to the west of PBT location) was found between 13:30 - 14:00, and it agreed with the arrival time map (for both "match" and "delay" group).

4.4 Discussion

4.4.1 The later passage of cloud-line

In general, the passage time of the cloud-line and the arrival time of SBF on which are detected at both KKP and BPL were the same within the distance range of

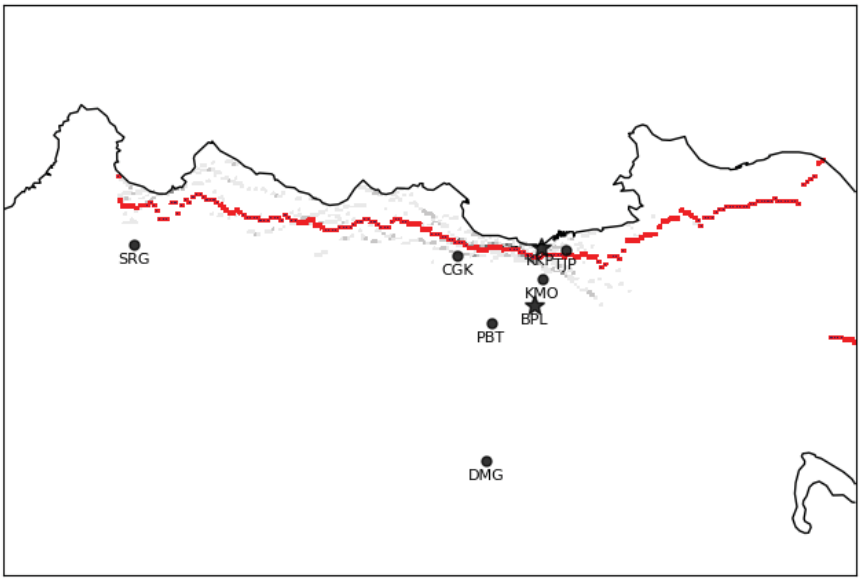

(a) KKP "match" arrival time (40 cases)

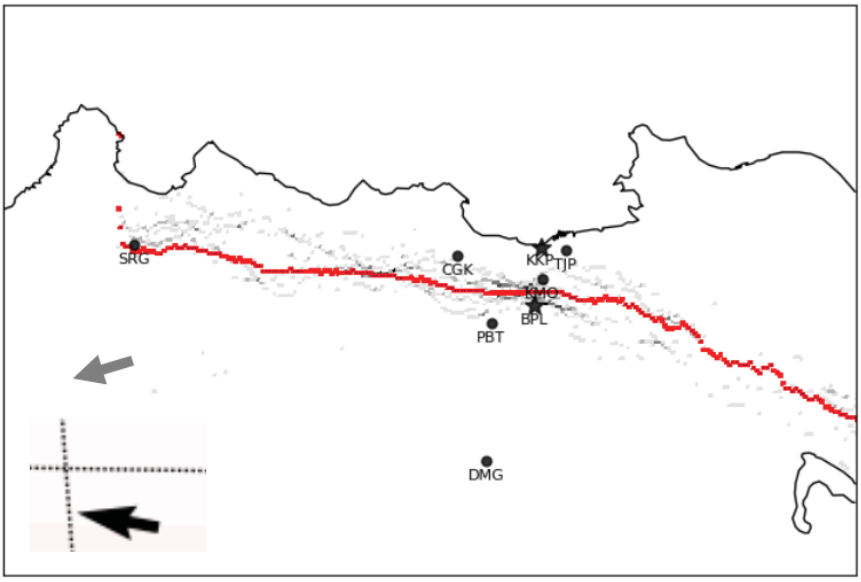

(b) BPL "match" arrival time (24 cases)

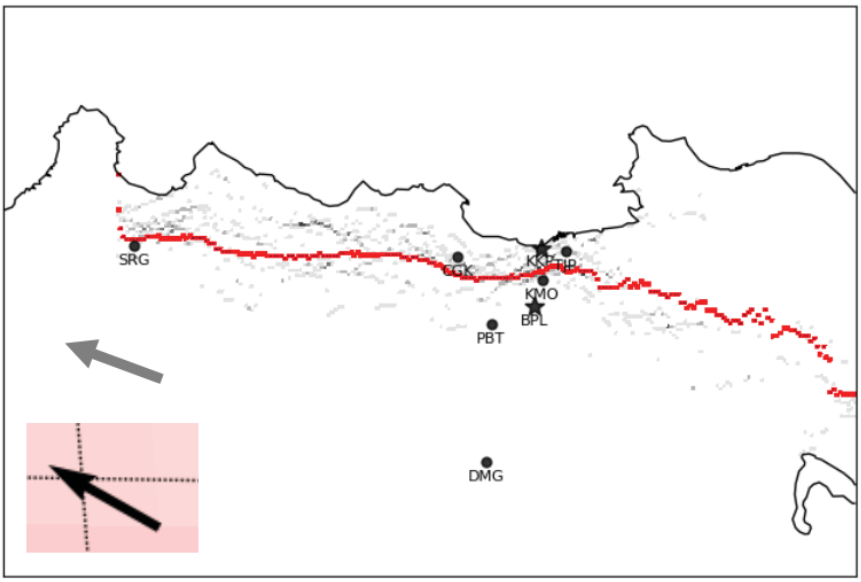

(c) BPL "later" arrival time (25 cases)

Figure 4.18: Spatial distribution of the cloud-lines composited based on the arrival time of SBF at KKP (5a) and BPL (5b and 5c). Grey lines indicate the cloud-lines for each case in the "match" and "delay" group. The darker color shows the density of the overlapped lines. And the red line depicts the mean spatial distribution of the cloud-lines and the line density was treated as the weight. The grey (black) arrows in 5b and 5c depict the 00 UTC mean wind of radiosonde (ERA-Interim re-analysis) data at 700 hPa (3 km). (After Ferdiansyah et al., 2020)

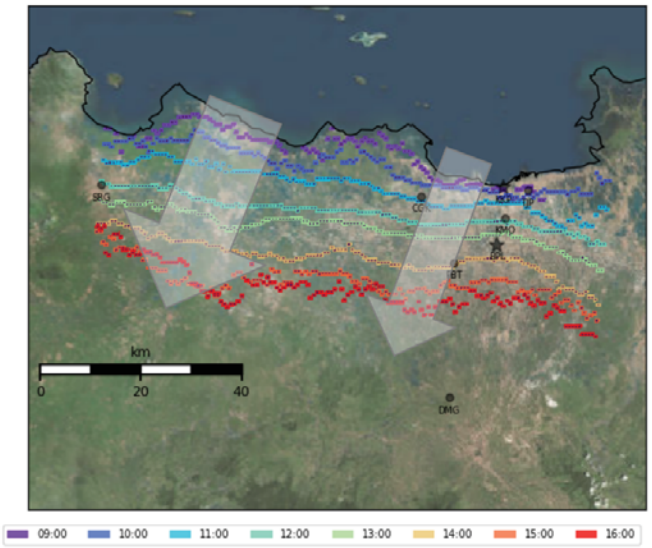

(a) "match" cases

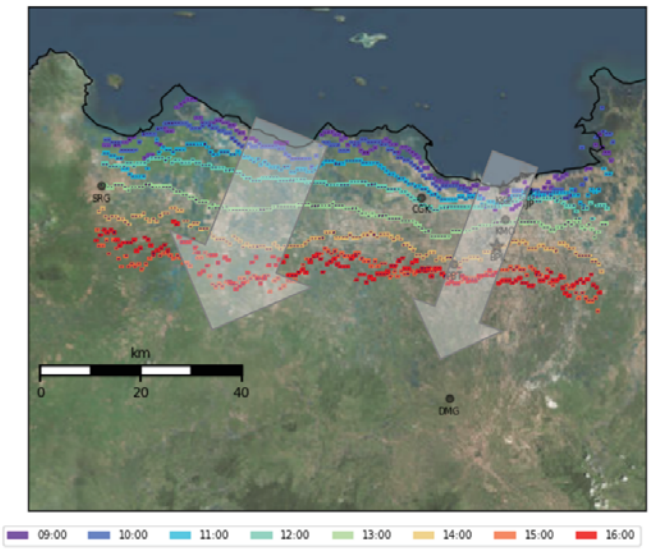

(b) "delay" cases

Figure 4.19: Mean arrival time of SBF derived from the composite of cloud-line passage. Arrows depict the mean wind direction from the meteorological station and point observation data. The larger (smaller) arrow indicates the faster (slower) inland penetration speed. (After Ferdiansyah et al., 2020)

less than 3 km (24 cases, "match" group) and with the bias time of 20 minutes. In some cases, the cloud-line tends to be located behind the SBF. The lag time exists between dissipation of the cumulus cloud and the penetration of the SBF (the cycle is initiated by surface warming, updraft, cooling, cloud formation, updraft decaying due to SBF penetration, and then cloud dissipation) can be considered as the reason for this later passage time of the cloud-line. And there are cases in which the cloud-lines were located behind the SBF location more than 5 km (25 cases, "delay" group). The different synoptic conditions between the two groups likely influenced the propagation of the cloud-line.

In addition, while in the mesoscale perspective, the certain synoptic wind at upper ABL could cause the cloud-line to slower propagate, we also found that there was a continuously existing cloud, particularly at the city center. What does cause the cloud to not dissipate (due to decaying updraft by SBF penetration) in such a particular location? One possibility is that there is another micro-scale mechanism which depends on the surface condition and induces the local thermal convection. The clouds keep existing because of the continuous updraft due to heating from the urban surface (UHI). This UHI circulation likely enhanced the local updraft regime at such a location. This heating source and moisture supplied by the sea breeze provide a favorable environment for the low cloud such as cumulus to form. Thus, the cloud was likely to continuously exist and the cloud-line seemed to be stagnant around the city.

When we use the cumulus cloud-line for estimating the propagation of sea-breeze front, the slower dissipation of cumulus cloud may indicate the slower propagation or stagnation of sea-breeze front. The cloud-propagation speed is somehow more influenced by the ambient synoptic condition which has larger scale than the local-convection scale. According to (Fujita et.al., 1975) the cumulus and stratocumulus type do not always continuously propagate, but the large scale of these cloud-types are able to be traced and very useful to estimate the low-level flow over the land. So in the context of the mesoscale event such as sea-breeze and the associated cloudiness may interact among them. The micro-scale will influence the cloud formation/dissipation while the synoptic scale will influence the cloud movement in general.

4.4.2 Possible mechanisms for the long-lasting cumulus

Figure 4.20 shows the surface roughness height over Jakarta City. The roughness height at the city center is around 2 to 5 m. Thermal and roughness are two main impacts of the urbanized area that have been reported for the delayed penetration of SBF (Freitas et al. (2007); Thompson et al. (2007); Varquez et al. (2015); Kusaka et al. (2019)). For instance, numerical simulation by Varquez et al. (2015) reported that the sea-breeze penetration was delayed over the urbanized

area due to increasing surface drag of high surface roughness over urban. This causes decreasing the heat advection to the downwind area, enhancing turbulent mixing due to convection, and increasing the ABL height. However, in our study, the observation site that has sufficient temporal resolution to detect the arrival time of SBF in the non-urbanized area was not available. The delayed penetration of SBF over the urbanized area can not be evaluated comparatively in this study. From Darmanto et al. (2017) study the surface roughness length (z0) over the city center of Jakarta was estimated at around 2 to 5 m. This value is somehow smaller than the z0 over the megacity, such as Tokyo (Kanda et al. (2013); Darmanto et al. (2017)), where the evidence of slower penetration speed was reported (e.g.,Yoshikado (1994); Varquez et al. (2015)). And it is also reported by Thielen et al. (2000); Kusaka et al. (2019) that rather than surface roughness, the sensible heat flux is more significant to the convergence mechanism. Thus, even though we did not obtain sufficient evidence of the roughness effect, we hypothesize that the thermal impact of the urbanized area is more dominant to influence the cloudiness associated with the SBF penetration over the Jakarta region.

Since the later passage of the cloud-line than the arrival time of SBF mentioned above cannot directly explain the urban effect to the penetration speed of SBF, we evaluated the spatial distribution of the inland penetration distance from the map of arrival time. We found that at the same arrival time (at 12:00), SBF penetrated more in the western part outside of Jakarta (e.g., SRG, 10.6 km from the coastline) than in the Jakarta city (e.g., KMO, 6.26 km from the coastline). This indicated that from the derived two-dimensional SBF arrival from the cloud-line, we can obtain information about the spatial characteristic over the different surface conditions. Similar information cannot be obtained through the limited point observation data. The findings of this study reveal the close interaction between sea-breeze and UHI circulation. Moreover, this study indicates the UHI circulation potentially caused the delayed of cloud-line propagation in certain prevailing wind conditions. Therefore, this study contributes significantly to the previous sea-breeze studies over coastal-urban regions.

4.5 Summary

In this chapter, we present the results of cloud-line detection using the morphological snake algorithm. The detected cumulus cloud-line is reasonably able to represent the location of SBF. The detection and tracing by using satellite images can assist to provide the spatial information for inland penetration of sea-breeze front. In this study, the results show that the cloud-line was reasonably able to represent the arrival time of the SBF with a bias time of 20 minutes and within a distance of 3 km. The mean penetration speed obtained from the cloud-lines pas-

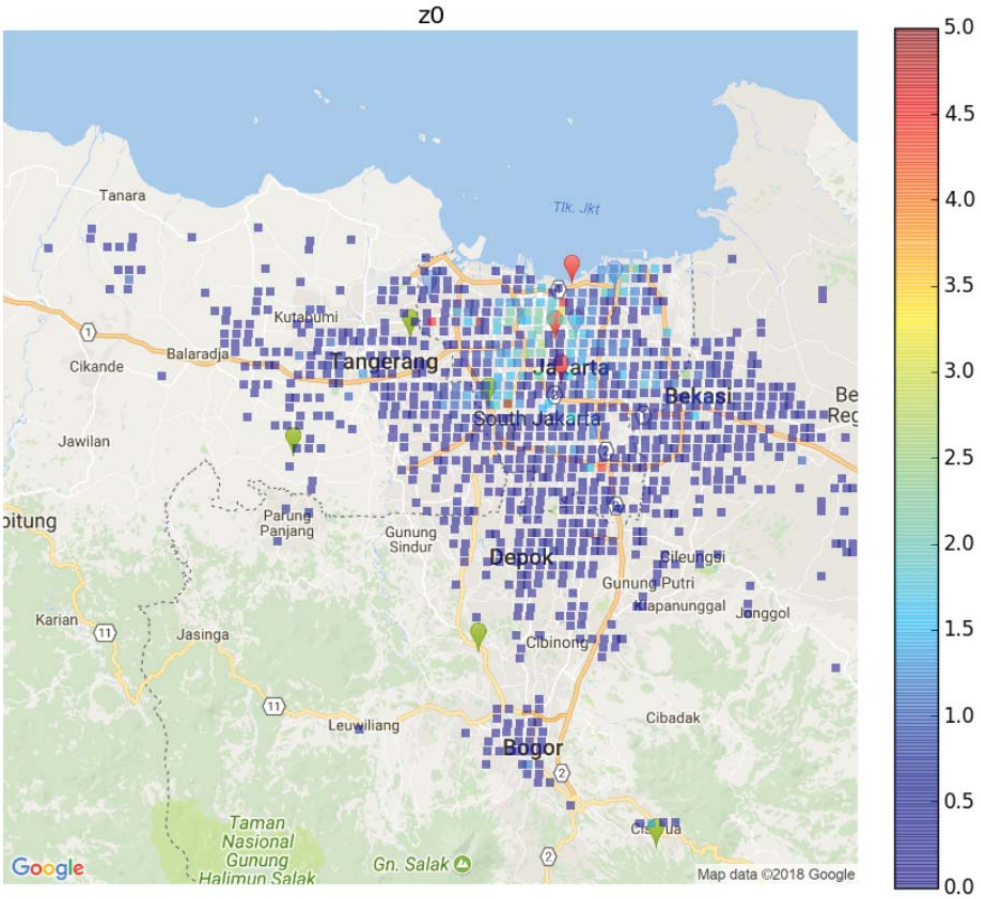

Figure 4.20: The surface roughness height of 1 km grid (z0, unit in [m]) over Jakarta City. (Data source: Darmanto et al., 2017, after Ferdiansyah et al., 2020))

sage was slightly slower than that estimated from the arrival time of SBF (1.4 ms^{-1} and 1.5 ms^{-1}, respectively). In certain cases, the cloud-lines passage was found to be behind the SBF more than 5 km, particularly in the city center. This indicated that the enhanced updraft due to urban-heat-island circulation might potentially cause the long-lasting of cloud-line in certain prevailing wind condition.

Chapter 5

Application to another coastal urban region (Tokyo, Japan)

This chapter presents the application of the proposed framework (described in Chapter 3 and Chapter 4) to another coastal urban, in order to provide spatial inland-penetration of sea-breeze front (SBF).

5.1 Introduction

Tokyo as mid-latitude and Jakarta as tropic region, the comparison between two different climate regimes raises attention. Even both cities are located in the plain area and surrounded by the mountainous area, the direction of the prevailing wind and coastline orientation of Jakarta and Tokyo is different. In Jakarta, the prevailing wind is opposing the direction of sea-breeze penetration, while in Tokyo in the same direction. With those similarities and differences, such as topography, coastline orientation, climate and the background synoptic condition, there can be some common characteristics and features in term of physical phenomena of the sea-breeze which accompanied with the cumulus cloud-line that are worth to be compared.

The results described in the previous chapter (Chapter 4) revealed that the cloud-line passage has negative bias time and distance about 20 minutes (later) and 3 km (behind), respectively. However, in Jakarta case, the arrival-time validation was limited to only the observation sites located in urbanized area (due to the observation data source limitation). It is necessary to validate also the arrival time of the sea-breeze front and the passage time of the cloud-line in less-urbanized area.

The coverage of meteorological observation in Tokyo area includes some sites which are located in urbanized and less-urbanized area. The arrival time of sea-

breeze front can be validated for both areas. Moreover, in Tokyo, the behaviour of two sea-breeze systems that blowing from the Sagami Bay and that from the Tokyo Bay can also be observed.

Therefore, the objective of the work described in this chapter is mainly to evaluate the global applicability of the proposed framework. The procedure was divided into three steps. The first step is to analyze the typical cloudiness pattern during sea-breeze days (SBDs). The second step is to validate the spatial distribution of the arrival time of SBF represented by the passage of the cloud-lines. And finally, is to quantify how is the penetration speed over the urbanized area and that over the less-urbanized area from the derived spatial penetration of sea-breeze front.

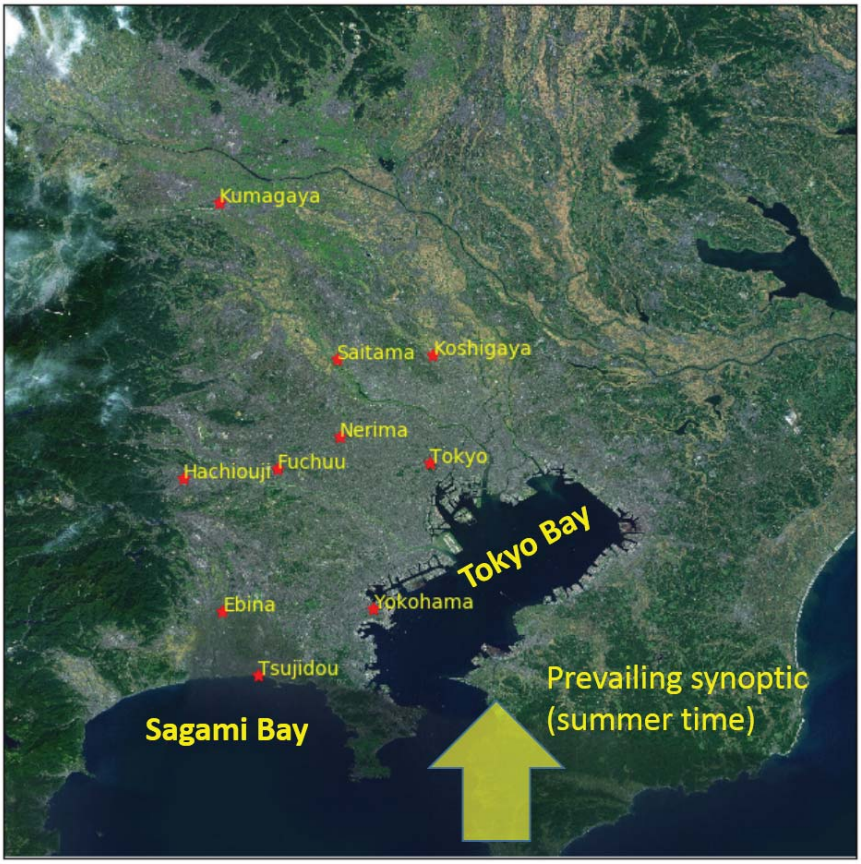

Figure 5.1: The study area, Tokyo is located in the Kanto Plain of Japan. Red stars depict the location of the observation points of the AMeDAS. Yellow arrow indicates the typical prevailing wind in summer time. The high-pressure system is usually located in Pacific Ocean.

5.2 Study Area

Tokyo is located in Kanto Plain area, the largest plain in Japan. Tokyo has sub-tropic climate. Compared to the tropics region, various horizontal pressure-gradient provides more dynamic synoptic disturbance which may influence the sea breeze development. And the onset time of sea breeze will also have seasonality according to solar radiation timing. Tokyo region is also surrounded by mountainous area in its northern and western. And bordered by the Tokyo Bay in its southeastern and Sagami Bay in its southern (Figure 5.1). The typical wind during summer in Tokyo is southerlies as the high-pressure system is located over Pacific Ocean. The condition of warm summer-season and weak synoptic-wind provide favorable environment for the thermal local-circulation such as sea breeze to develop (e.g., Yoshikado and Kondo (1989).

5.3 Materials and method

5.3.1 Observation Data

For screening the SBD and estimating the arrival time of the SBF, the 10 minutes observation data of the Automated Meteorological Data Acquisition System (AMeDAS) operated by Japan Meteorological Agency (JMA) (Table 5.1) was utilized. The parameters are temperature, wind, precipitation, and solar-radiation. The period for analysis was summer season (July August September, JAS) from 2015 to 2018.

Table 5.1: The list of AMeDAS stations

Station	Distance from coastline [km]	Longitude	Latitude
Tsujidou	0.69	139.448	35.314
Ebina	13.204	139.385	35.314
Fuchuu	24.6	139.75	35.642
Hachiouji	36.503	139.644	35.475
Yokohama	0.143	139.651	35.437
Tokyo	3.758	139.778	35.667
Nerima	17.468	139.756	35.655
Koshigaya	24.041	139.778	35.667
Saitama	28.788	139.767	35.661
Kumagaya	64.52	139.778	35.667

5.3.2 Satellite Data

To analyze the cloudiness feature the visible band (B03) of Himawari-8 is used. This band has highest spatial resolution (500 m) among 16 bands of Himawari-8. The temporal resolution is every 10 minute for full-disk scanning (10 sections) (Bessho et al., 2016). Tokyo is section 2. Original projection is geostationary projection. The selected area is cut as the final array of 220 x 320 grid with about 0.005 deg resolution. The raw data (digital counts) was converted to radiance value then it was converted to albedo value. As pre-processing step for albedo, the albedo value was normalized using a method proposed by Zhuge et al. (2012) to reduce the solar time dependent. And to identify cloud object, the threshold of albedo value 0.3 was selected (Zhuge et al., 2012; Taniguchi et al., 2001). The pre-processing procedure and threshold selection was conducted as same as for Jakarta case.

Similar to Jakarta analysis, the XY-position of the pixels in the original image (geostationary coordinate) was used in the processing rather than use the projected latitude-longitude grid Cartesian coordinate. This way is commonly used for tracking algorithm using satellite images (private correspondence with researchers at Japan Meteorological Agency who develop the Atmospheric Wind Vector) to minimize the location error for different projected resolution of the images. Since the projected Cartesian coordinate for Jakarta is different with Tokyo.

5.3.3 Additional data

In addition to the above-mentioned data, the wind and humidity parameter of ERA-interim re-analysis (spatial resolution 0.75 deg, Dee et al. (2011)) were utilized to obtain the synoptic condition for each case study. And the elevation data provided by the US Geological Survey was utilized for land-sea masking. The elevation data was also used to construct the coastline dataset which has been adjusted to match the pixels of satellite images (which were projected into geostationary projection). This dataset was used to define the distance of the sea-breeze front from the coastline.

5.3.4 The identification of sea-breeze day

In the first step of the screening process, we selected only the days when the mode change of wind direction, from land-breeze to sea-breeze mode is exist. Each mode should be stably flow at least for four consecutive hours during early morning and afternoon for land-breeze and sea-breeze, respectively (the method is summarized in Table 5.2). In addition, the following criteria to define the sea-breeze day (SBD) was used: no precipitation in the day and the previous day, the wind direction

Table 5.2: Summary of the method

Observation data	B03 satellite data
(1a) Sea-breeze day selection • Wind mode change (from land breeze to sea-breeze mode) • The sea-breeze flows steady at least for consecutive two hours (1b) Composite for SBD and non-SBD cases	(3a) Check the typical cloudiness pattern • Cloudlines (parallel to coastline) • Rolls (parallel to wind flow) • Irregular (including convective clouds) • Clear-sky (3b) Composite for each pattern
(2a) SBF arrival-time estimation • Decreasing of air temperature increasing rate (by finding local maxima) • Significant increasing of specific humidity (by finding local maxima) • Increasing of the wind speed (2b) Composite based on the SBF arrival time	(4a) Cloud-lines detection using Morphological Snakes algorithm for SBF cases that accompanied with the cloudlines (4b) Quality check of the detected cloud-lines (4c) Composite based on each time

of sea-breeze mode persists for at least two consecutive hours, and radiation time more than 7 hours. This additional screening criteria aims to filter out the typhoon and rainy days and very strong synoptic disturbances. For this screening process the point observation Tokyo (Figure 5.1) was chosen as the reference station.

In the second step, the arrival time of sea breeze front (SBF) was estimated using temperature and wind observation data at AMeDas stations as shown in Figure 5.1. The arrival time was defined as the time when the increasing rate of temperature is to stop or to decrease, the significant increase of wind speed and a stable landward wind direction to blow. There are several approaches for estimating the arrival time of SBF, depends on the weather parameters of the available data (e.g., wind, humidity, air and land-sea surface temperature), topography and background climate of the region (e.g., moist, dry). For instance, in warm region Sergipe, Brazil, Anjos and Lopes (2018) reported that the SBD mostly happened in the hot days. And the increasing of solar radiation during SBD can not be compensated by the cooling from sea-breeze. And in dry region, Jordan, Naor et al. (2017) reported that the humidity increase as the penetration signal for SBF arrival was not well identified. However, for both mentioned regions, the significant increasing of wind speed and direction change are more prominent as the arrival signal of SBF.

In the third step, the procedure for cloud-line detection was similar to the procedure of Jakarta case. The verification with the observation was carried out by detecting the passage time of the cloud-line within radius of 2 km (9 by 9 pixels) around the AMeDAS station where the arrival time of SBF was estimated. For this, the data at Tsujidou, Ebina, Hachiouji and Fuchuu were utilized to validate the sea breeze arrival from sagami Bay and at Yokohama, Tokyo, Nerima, Saitama, Koshigaya and Kumagaya for sea breeze from Tokyo Bay (Figure 5.1). The composite analysis was conducted based on SBD with cloud-line and SBD without cloud-line, as well as based on the arrival time of SBF to know the condition before and after the sea-breeze arrival.

5.3.5 Cloudiness associated with sea breeze

Sea breeze circulation is a local circulation and a kind of meso-scale cold-front type. This such discontinuity that is formed at the convergence zone between the sea-breeze flow and the off-shore synoptic wind, it is called also the sea-breeze front (SBF). The relationship of sea breeze and off-shore synoptic scale flow is that sea breeze mainly occurs in the weak synoptic condition, clear skies and intense solar radiation (Miller et al., 2003). However, sea breeze can also trigger the cloud formation at the sea breeze convergence zone (Miller et al., 2003; Azorin-Molina et al., 2009b). For Tokyo case, the cloudiness pattern during SBD was categorized into four patterns. Cloud-line (formed in parallel to the coastline), roll-structure

(formed in parallel with the breeze direction), irregular (mostly convective clouds and dense cirrus), and clear-sky.

One of the typical features among above patterns is the formation of cumulus cloud-line in parallel to the coastline. The cloudline can exhibit the location of the SBF. We can treat this cloud-line as the traceable feature to detect inland penetration of SBF. By tracing time evolution of the inland penetration of the SBF, the penetration speed over various surface condition (such as over the urbanized area and that over the less-urbanized area) was quantified.

5.4 Results

5.4.1 Sea-breeze day and cloudiness

Sea breeze day can be identified using wind shift di. Untuk tokyo, sea breeze day dapat didentifikasikan dengan adanya steady northerlies pada malam dan souterlies pada siang hari, clear sky with defined threshold of solar radiation time(i.e., Yoshikado 2013).

Figure 5.2 (all days: JAS season) and Figure 5.3 (sea-breeze days: 81 SBD) show the dominant wind direction during July, August and September (2015 to 2018) of the AMeDAS statios (ten stations). In summer period, the high-pressure system is located in the Pacific Ocean. As a result, in the daytime the southerly wind is blowing over the Tokyo area while nearly calm wind during nighttime.

In this period, 184 days of SBD-candidates were screened based on the wind-direction criteria. Among those, 81 days (from now on is referred as SBD cases) were selected based on the precipitation and radiation criteria. Figure 5.4 depicts the amount of cloudiness pattern during SBD cases. The cloud-line pattern occurrence was more than 30 percent, the largest among four patterns.

Figure 5.5 and Figure 5.6 show the percentage of cloud occurrence around Tokyo at 10 AM and 2 PM, respectively. The percentage was calculated from the composite of the cloudy pixels for each cloudiness pattern in 81 SBD cases. Compared to other patterns, the pattern of cloud-line exhibited the clear inland penetration between morning and afternoon. This also exhibited the inland penetration of SBF.

After screening the SBD cases, we selected the cloud-line cases (33 cases) among 81 SBD cases. We estimated the arrival time of SBF among the AMeDAS stations. Figure 5.7 shows the composite of temperature and wind speed at Tsujidou, Ebina, Tokyo and Nerima. As can be seen, that the temperature decreased and wind speed increased after SBF arrival.

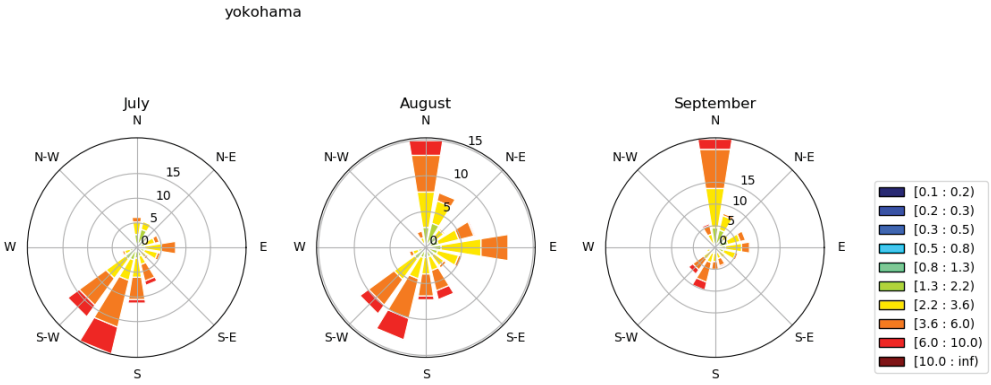

(a) Yokohama

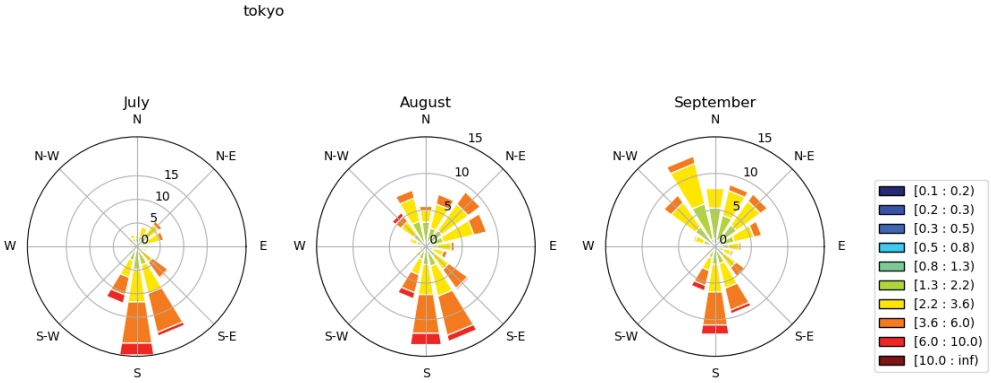

(b) Tokyo

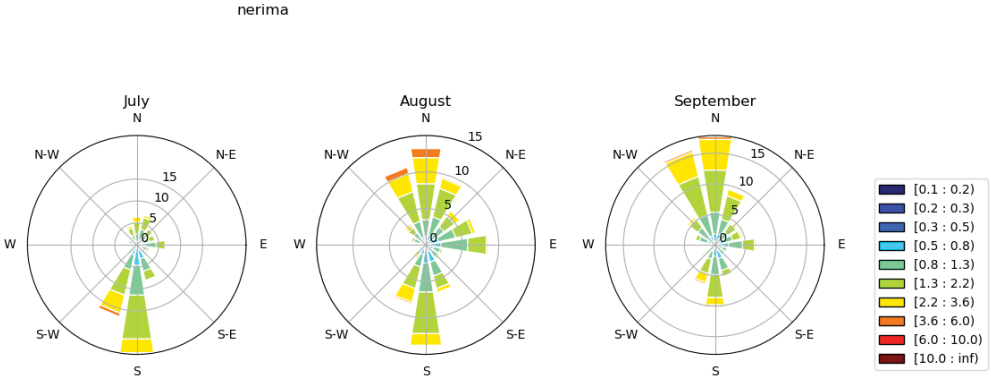

(c) Nerima

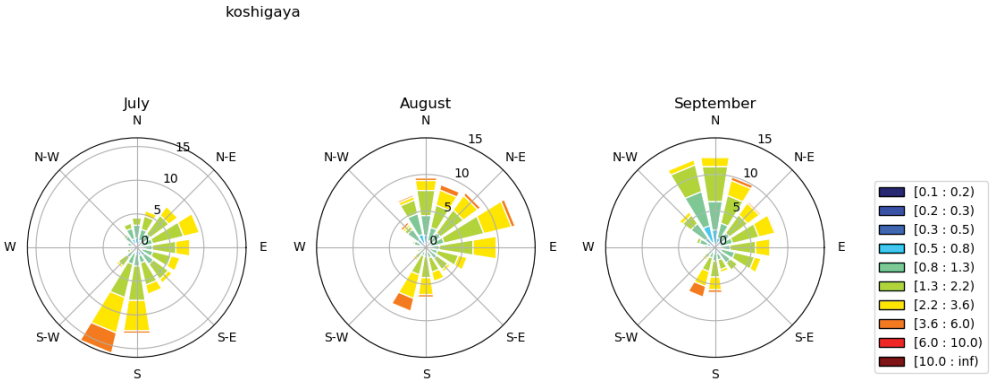

(d) Koshigaya

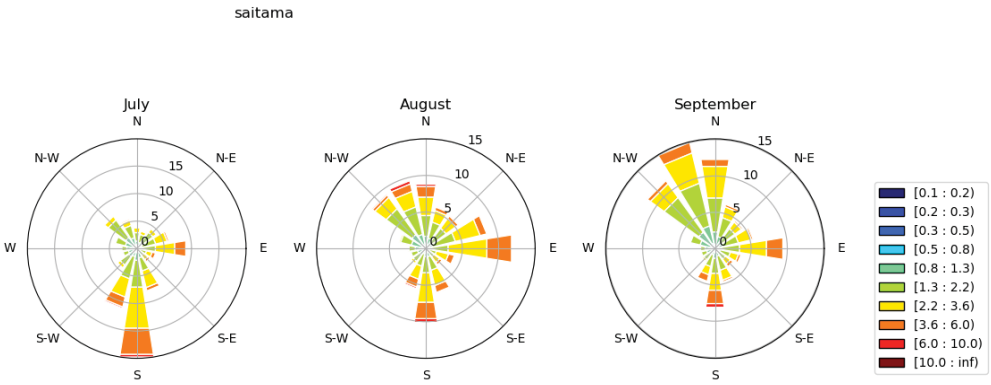

(e) Saitama

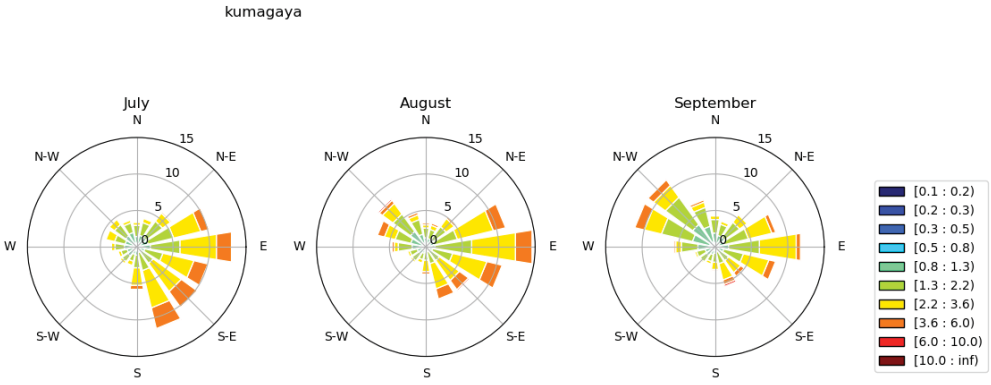

(f) Kumagaya

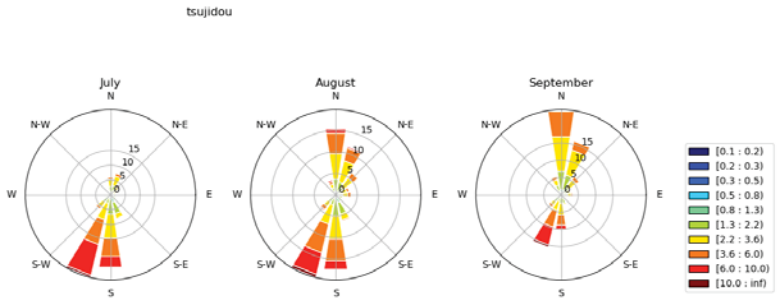

(g) Tsujidou

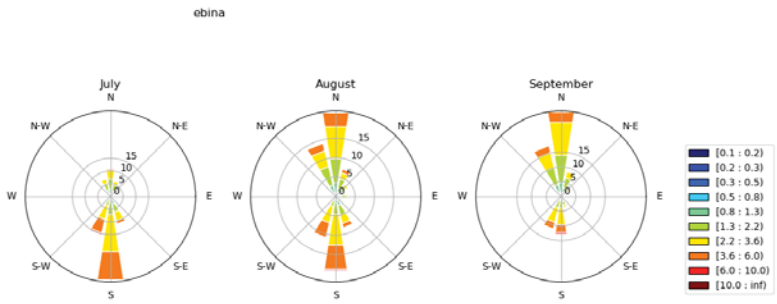

(h) Ebina

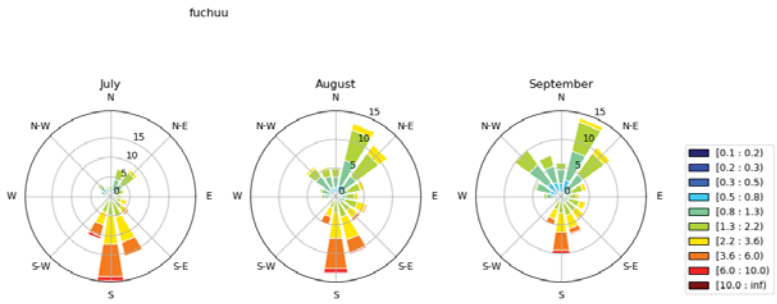

(i) Fuchuu

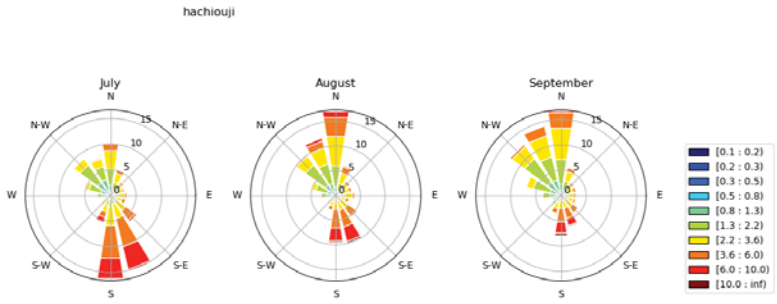

(j) Hachiouji

Figure 5.2: Windrose diagram for July-August-Sept (JAS) months. Colors indicate wind speed in m/s.

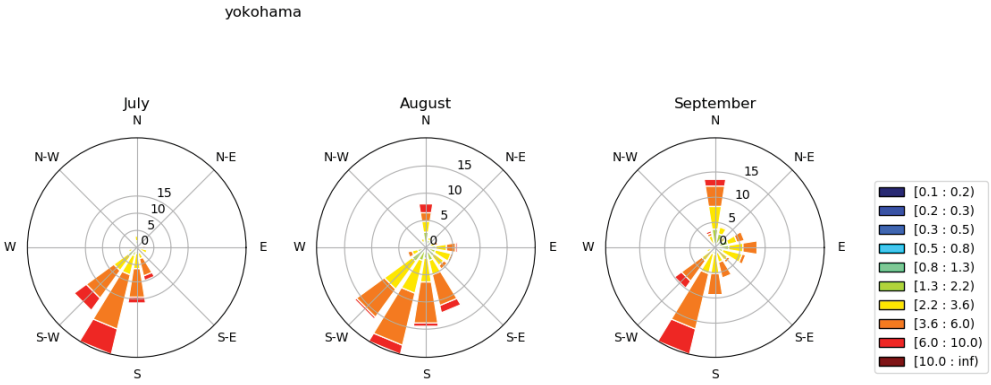

(a) Yokohama

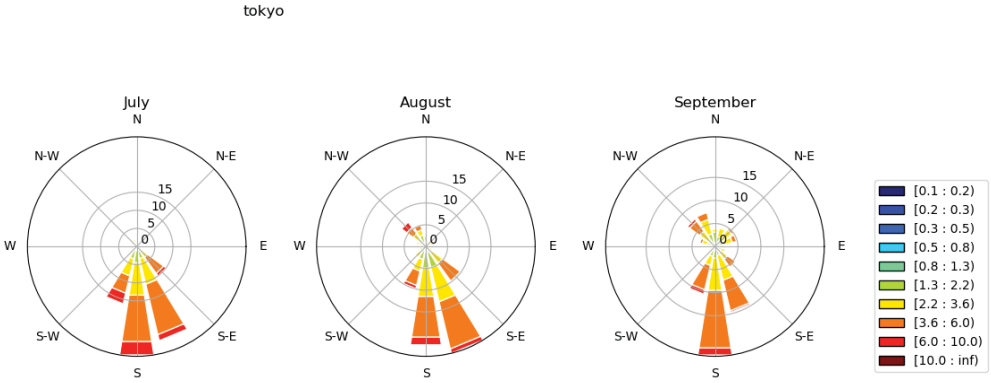

(b) Tokyo

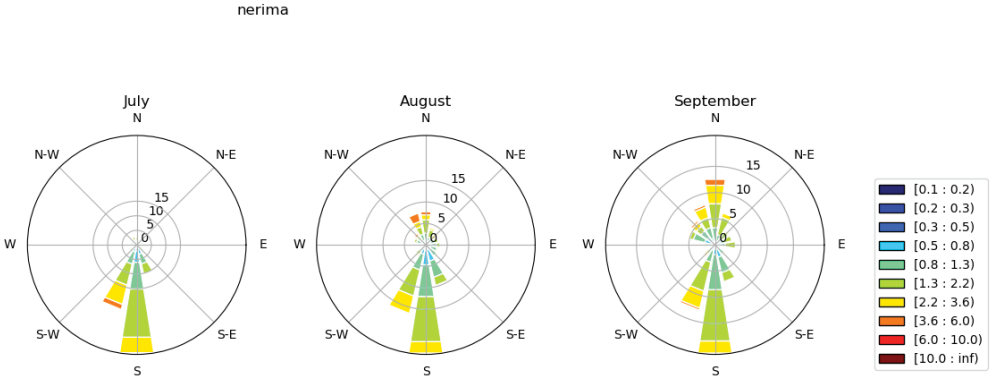

(c) Nerima

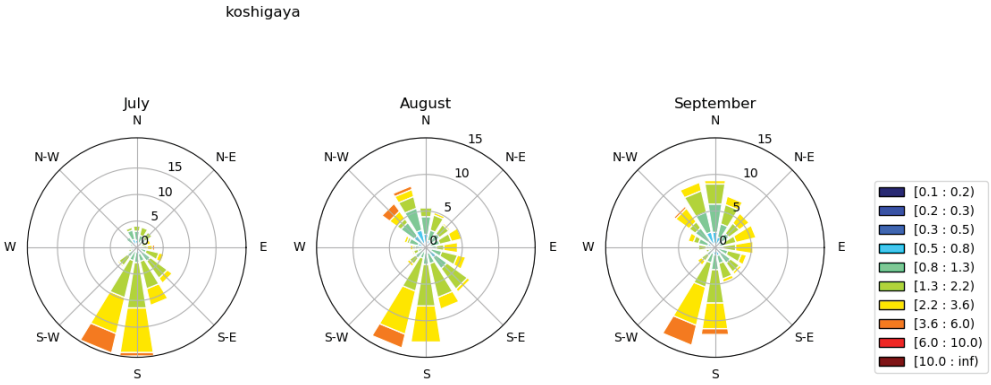

(d) Koshigaya

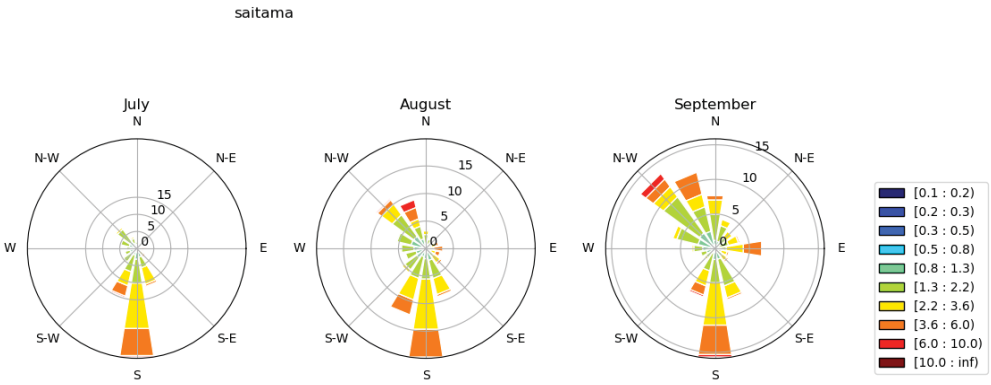

(e) Saitama

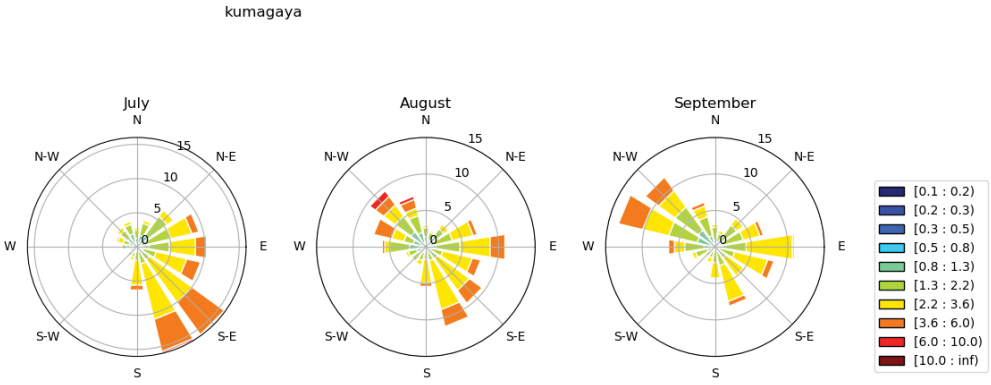

(f) Kumagaya

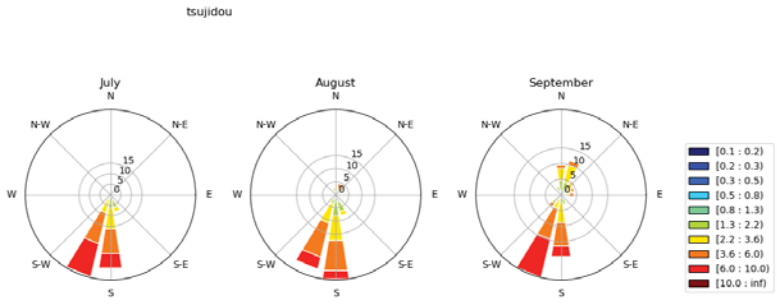

(g) Tsujidou

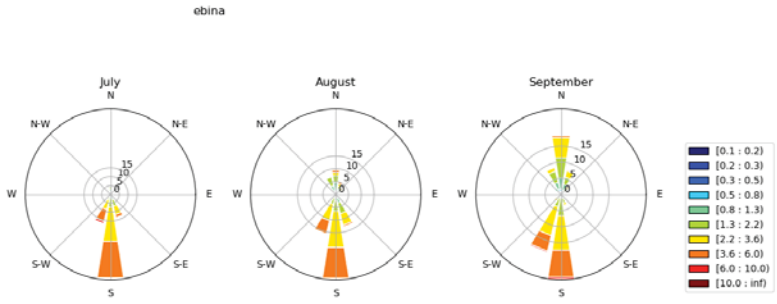

(h) Ebina

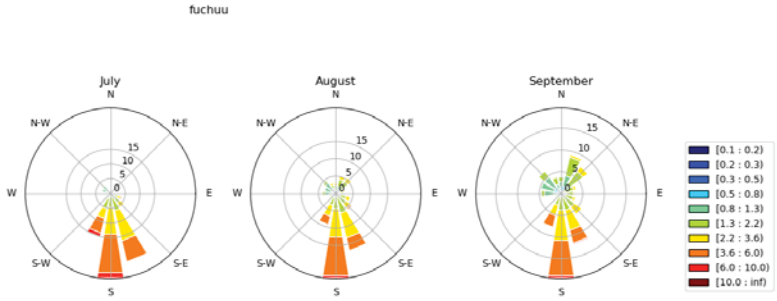

(i) Fuchuu

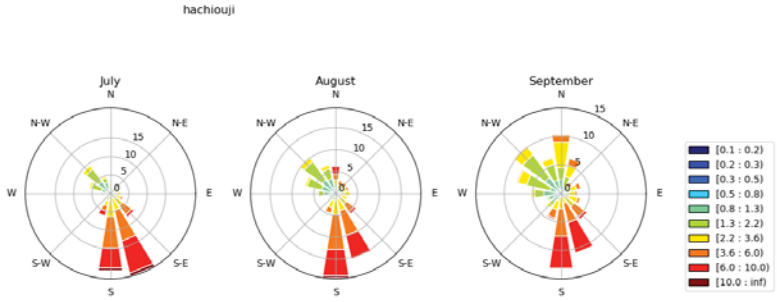

(j) Hachiouji

Figure 5.3: Windrose diagram for JAS during sea-breeze days. Colors indicate wind speed in m/s.

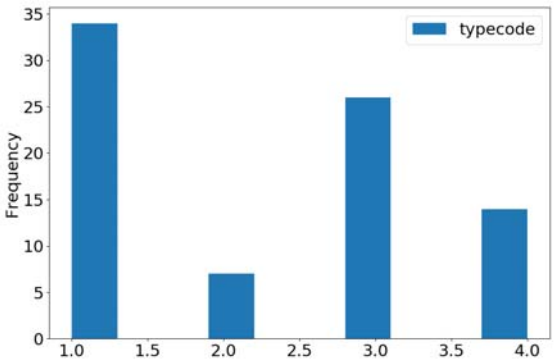

Figure 5.4: Histogram of the cloudiness pattern during sea-breeze days (SBD). Frequency is in percentage from total 81 selected SBD cases. The cloudiness patterns are grouped as; 1: Cloud-line, 2: Roll, 3: Irregular, and 4: Clear.

5.4.2 The cloud-line detection

We then verified the arrival time of SBF obtained from observation data with the passage time of the detected cloud-lines. The results are shown in Figure 5.8. For all stations, the arrival time agreed with the passage time within bias time obout 20 minutes. In general, similar to Jakarta case, the cloud-lines tended to be behind the SBF (later passage time). And in particular cases, the delayed passage times were more than 30 minutes. However, for Tsujidou and Yokohama, the cloud-line passage was not so often detected since both stations are located near the coastline. As a result, the delayed trend of the passage time could not clearly observed as the other inland stations.

In general cases, the cloud-line can be used as the tracer for penetration of SBF. However, in particular cases, such as over urbanized area, the dissipation of cumulus cloud takes longer time. In the local-scale perspective, there are two possible reasons. Due to intense heating from surface and due to polluted aerosol. In this case the propagation of cloud-line not representing the penetration of SBF. The long-lasting cloudiness was especially observed when the convergence lines were formed in the confluence area between sea-breeze from Tokyo Bay and Sagami Bay. But, it is also possible that the SBF can be delayed due thermal and roughness impact from the surface. Especially for the rougher urban such as Tokyo. Nevertheless, the spatial pattern of cloud-line can distinguish which one due to SBF and which one due to UHI, rather than tracking only single or individual cloud. Since the lifetime of cumulus is also short.

Using the arrival time and the passage time estimated above, we calculated the penetration speed for sea-breeze from Tokyo Bay and Sagami Bay by dividing the distance between two reference stations by the arrival time/passage time difference.

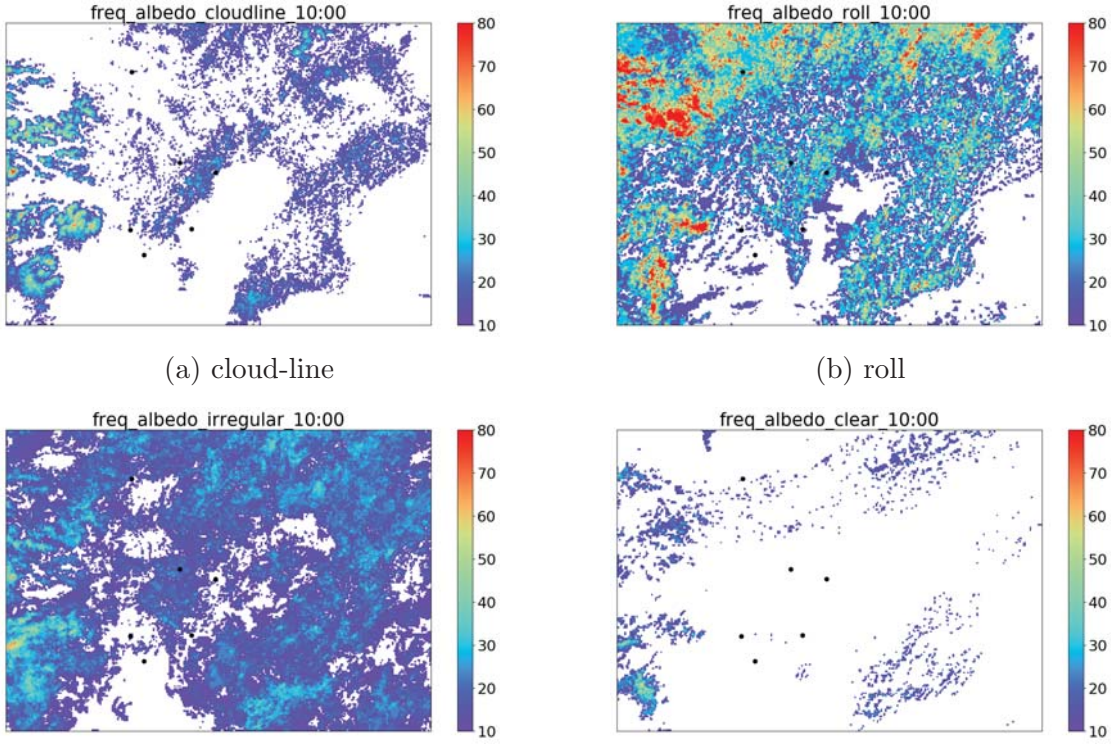

(a) cloud-line (b) roll

(c) irregular (d) clear

Figure 5.5: The frequency (in percentage) of cloudiness during daytime (10 AM local time) at around Tokyo region. The cloudy pixels are defined as the pixels which are larger than 0.3 of albedo value. The composite was calculated for each cloudiness pattern of 81 SBD cases.

The reference station for sea-breeze from Sagami Bay are Ebina and Hachiouji, and for sea breeze from Tokyo Bay are Tokyo and Saitama. These stations were selected according to the nearest-perpendicular orientation to the coastline. The result is shown in Figure 5.9. The sea-breeze from Sagami Bay penetrated within 1.8 to 4.2 m/s (mean speed: 2.8) and the sea breeze from Tokyo Bay was slower within 1 to 2.9 m/s (mean speed: 1.8 m/s).

5.4.3 Spatial distribution of the SBF inland penetration

Finally, from the time evolution the cloud-line, we derived spatial distribution of SBF inland penetration (Figure 5.10, Figure 5.11, and Figure 5.12). In current study, maximum penetration distance can not be estimated properly due to the disappearing of cumulus cloud-lines or can not maintain their shape longer at around 3PM to 4 PM local time (such as due to orographic wind, etc). At 3 PM,

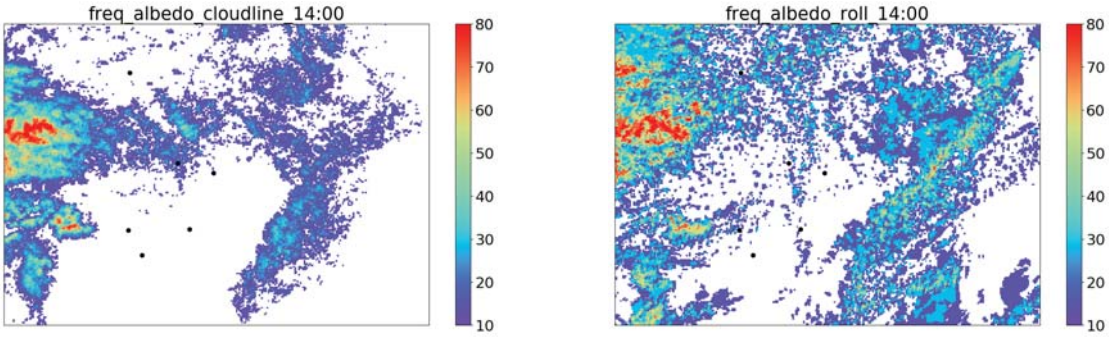

(a) cloud-line (b) roll

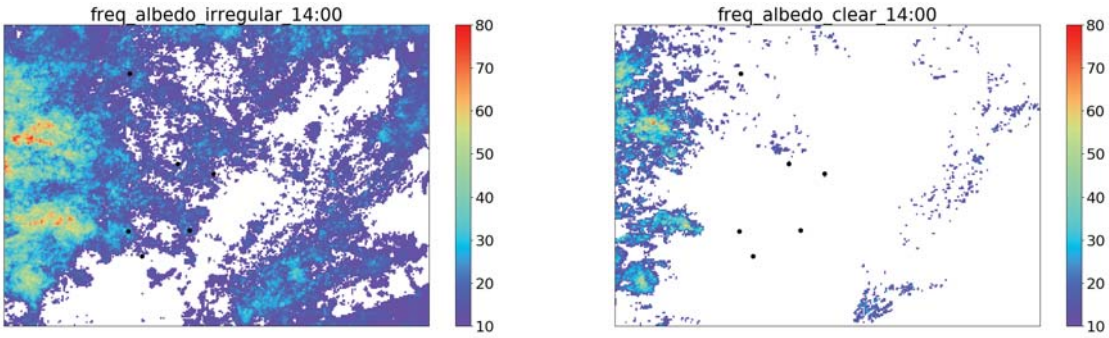

(c) irregular (d) clear

Figure 5.6: As same as Figure 5.5 except for 14:00.

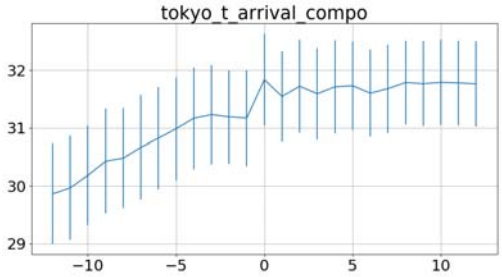

(a) Tokyo Temperature [deg C]

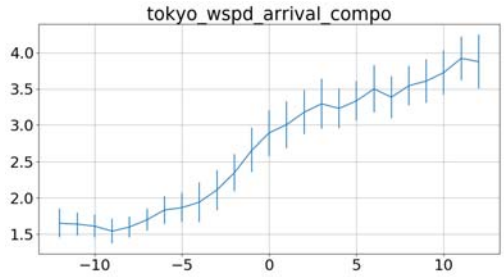

(b) Tokyo Wind speed [ms^{-1}]

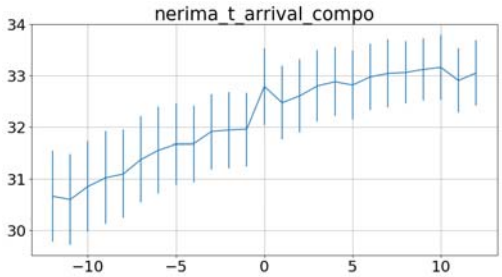

(c) Nerima Temperature [deg C]

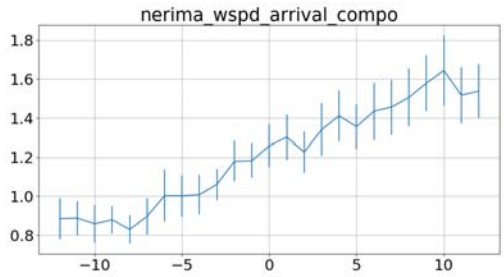

(d) Nerima Wind speed [ms^{-1}]

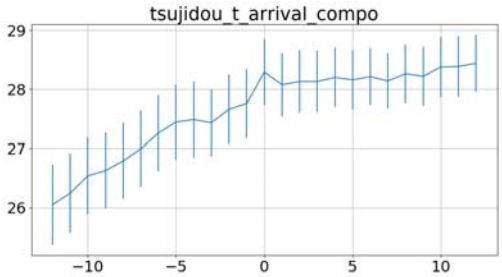

(e) Tsujidou Temperature [deg C]

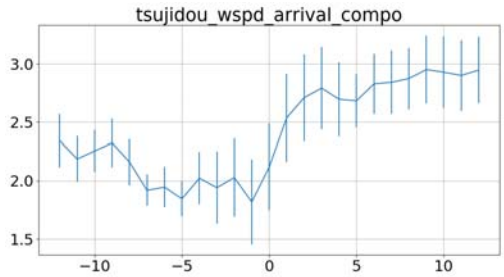

(f) Tsujidou Wind speed [ms^{-1}]

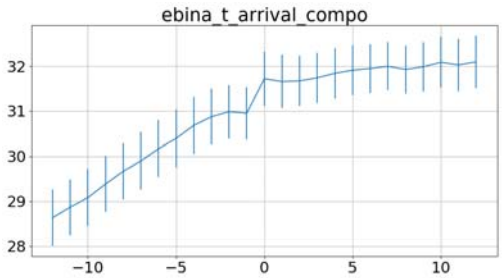

(g) Ebina Temperature [deg C]

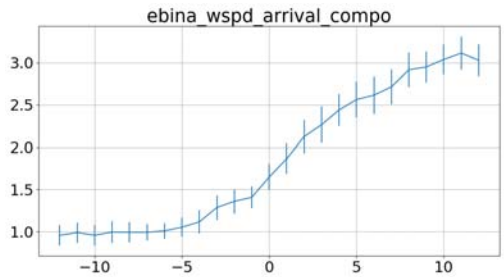

(h) Ebina Wind speed [ms^{-1}]

Figure 5.7: Composite of temperature and wind speed at four references stations, two hours before and two hours after arrival of SBF. The time=0 is the estimated arrival time of SBF at those sites.

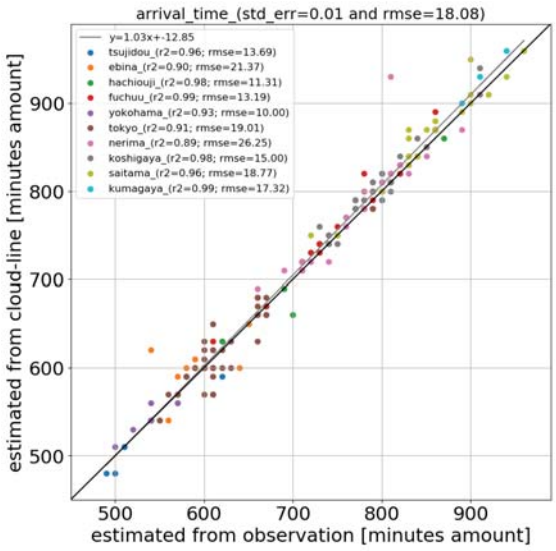

Figure 5.8: Comparison between arrival time of SBF and the passage time of cloud-line. The numbers in x and y-axis show the amount of minute for the arrival time (e.g., 10:10 is 10x60 + 10 = 610 minutes). The y=x line is drawn as the black solid line.

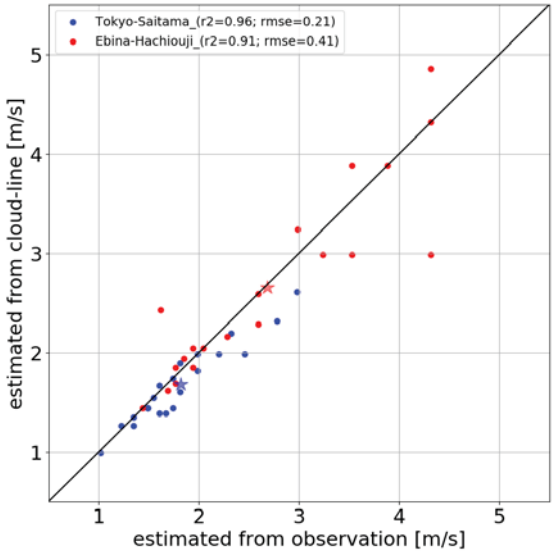

Figure 5.9: Comparison between penetration speed of SBF estimated from observation and satellite. The blue and red color depict the represent observation point for sea-breeze from Tokyo Bay and that from Sagami Bay, respectively. The star marks show the average speed. The y=x line is drawn as the black solid line.

SBF penetrated 45km at less urbanized area (sea breeze from Sagami Bay) and 28 km at more-urbanized area (sea breeze from Tokyo Bay).

From the mean arrival time, and mean penetration distance, the result indicated the different penetration speed between sea breeze coming from Sagami Bay and Tokyo Bay. As can be seen clearly in a case study on August 4, 2015 (Figure 5.13). To explore the reason for this, some possible mechanism can be considered as following.

- Synoptic prevailing wind (incld. atmospheric stability)(Porson etal 2007, Chiba etal 1999, Simpson 1994, Estoque 1962)
- The orientation of the coastline and curvature (Chiba etal 1999, Simpson 1994, Estoque 1962)
- Sea surface temperature (incld. bay depth) (Misra etal 2011, Oda and Kanda 2004)
- Sensible heat flux from the surface (Thielen etal 2000, Kusaka et al 2019)
- Surface drag due to surface roughness (Yoshikado 1994, Varquez etal 2015)

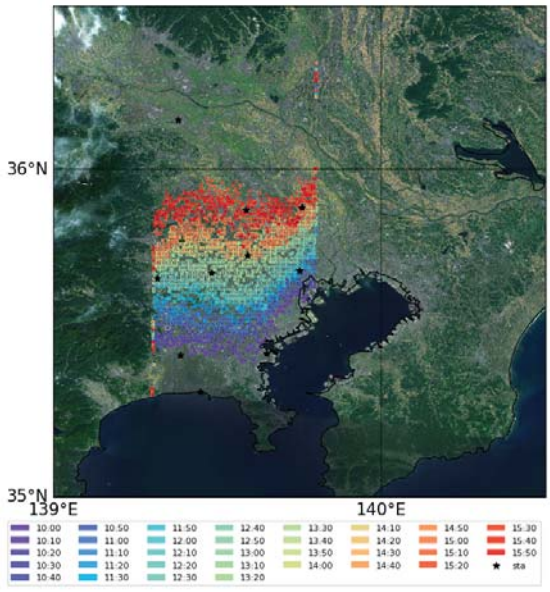

Figure 5.10: Composite of SBF arrival time (every 10 minutes)

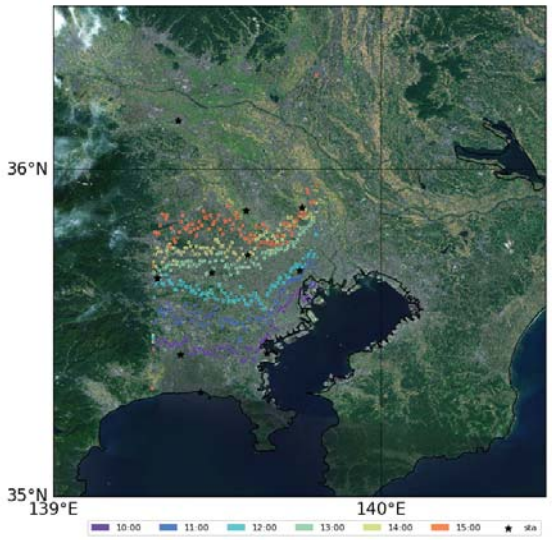

Figure 5.11: Composite of SBF arrival time (every 1 hour)

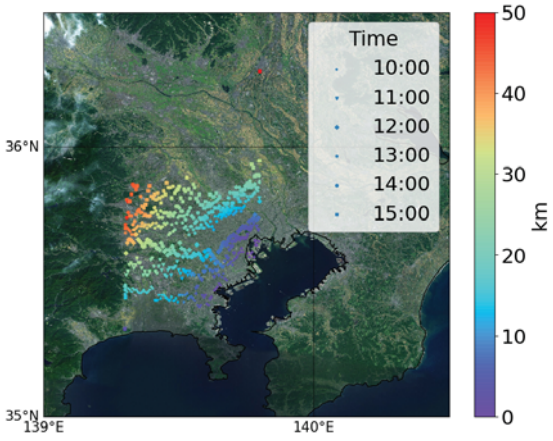

Figure 5.12: Mean penetration distance (in km)

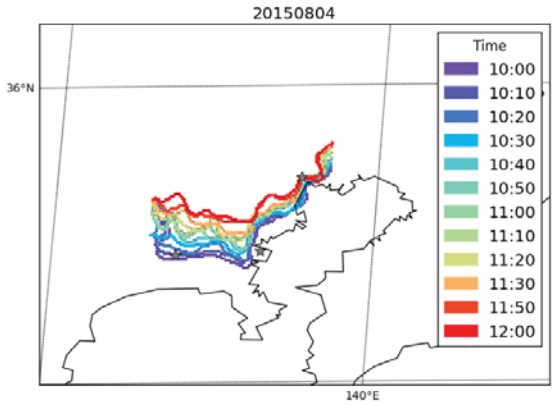

Figure 5.13: Sea-breeze front arrival time. The gray-scaled plot is the urban-surface roughness length (z0).

5.4.4 Synoptic wind during sea breeze

As a case per case, three typical modes of the sea-breeze were found in this study based on the orientation of the cloudline to the direction of the wind speed for the sea-breeze over Tokyo. The sea-breeze mode that is dominant from Tokyo Bay (T-mode, Figure 5.15), from Sagami Bay (S-mode, Figure 5.14) and the mode when both sea-breezes are dominant (ST-mode, Figure 5.16). Based on the typical sea-breeze modes, the orientation of the cloud-lines are representing the surface wind direction for each mode (the corresponding prevailing synoptic wind from ERA-Interim re-analysis data are shown in (c) panel of each figure).

In addition to the above synoptic wind pattern, the case study shown in Figure 5.17, indicated that the opposing synoptic wind might prevent the large scale inland penetration of sea breeze. This similar result was also found for Jakarta case. The synoptic wind was likely to affect the large scale penetration, both for sea breeze blowing from Sagami Bay and that from Tokyo Bay.

From previous studies, it has been reported that the cumulus cloudline can be formed during sea breeze event, particularly in weak synoptic condition and sufficient moisture within ABL (Simpson, 1994; Borne et al., 1998; Azorin-Molina et al., 2009b; Miller et al., 2003). Figure 5.18 to Figure 5.21 show the composite of synoptic condition for cloudline cases (33 cases) and non cloudline cases (48 cases). For geostrophic wind (at near surface, 1000hPa level), there was almost no significant different in both cases (Figure 5.18), about 4 to 5 m/s. But for humidity (at near surface, 1000hPa level), the cloudline case was more humid (Figure 5.19) than the non cloudline cases by 0.002 kg/kg.

Similarly with geostrophic wind, no significant different was found between cloudline and non cloudline cases for wind at lower part of ABL (1000hPa) as can

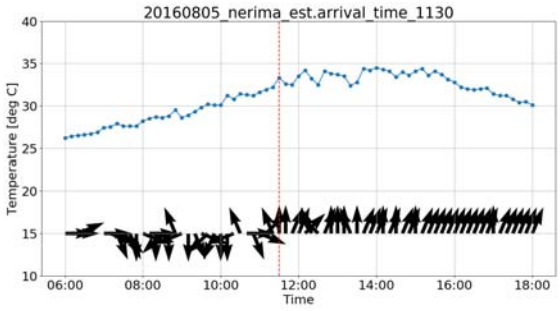

(a) Arrival time of SBF

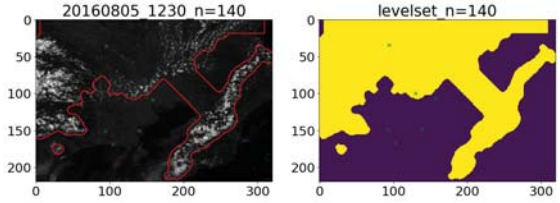

(b) Passage time of the cloud-line

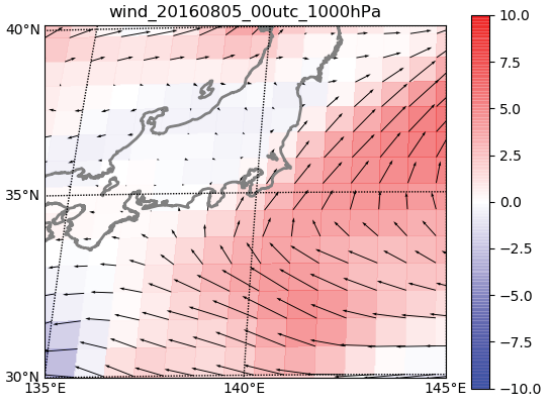

(c) 1000hPa wind at 00UTC

Figure 5.14: Arrival at Nerima. S mode of sea breeze

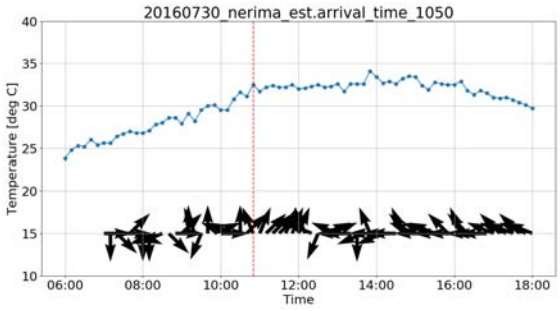

(a) Arrival time of SBF

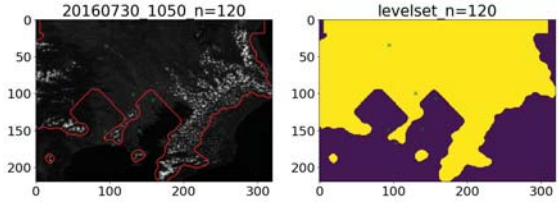

(b) Passage time of the cloud-line

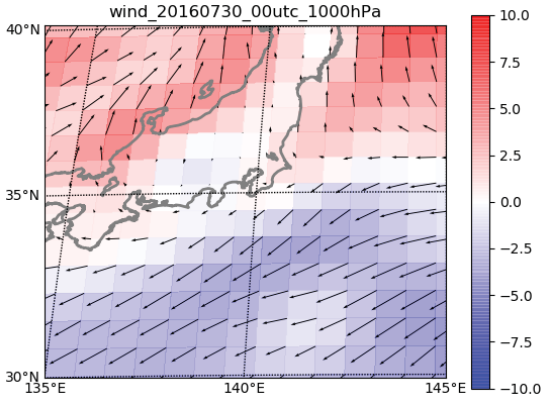

(c) 1000hPa wind at 00UTC

Figure 5.15: Arrival at Nerima. T-mode of sea breeze

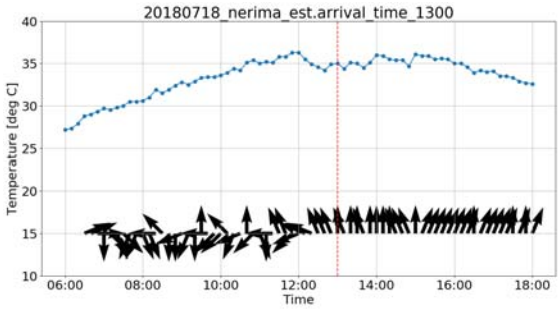

(a) Arrival time of SBF

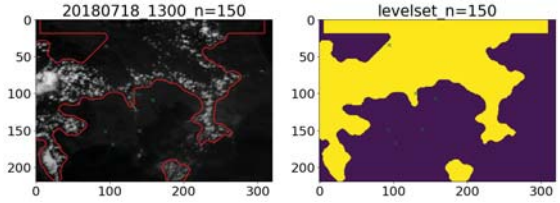

(b) Passage time of the cloud-line

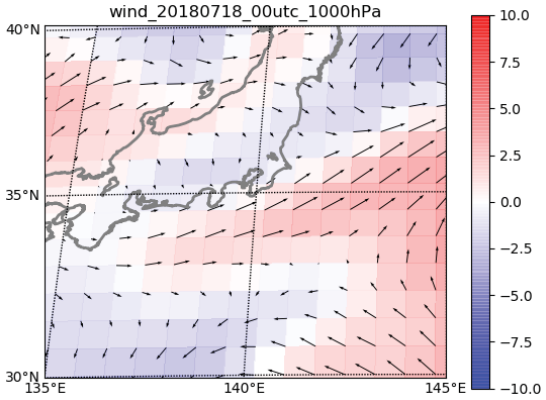

(c) 1000hPa wind at 00UTC

Figure 5.16: Arrival at Nerima. ST-mode of sea breeze

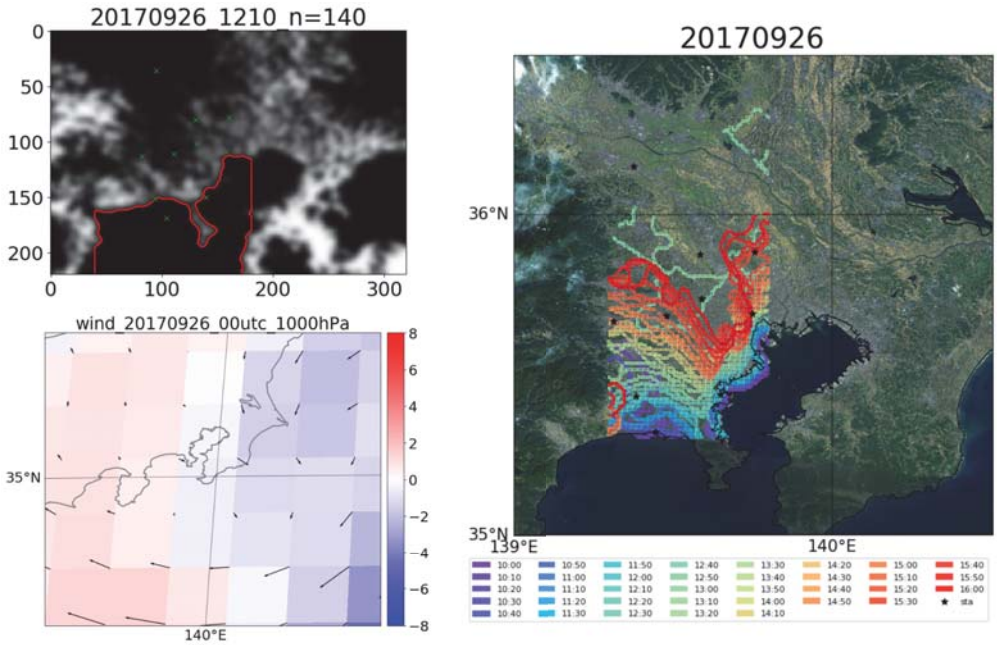

Figure 5.17: Case study of sea-breeze event under opposing synoptic wind (Back-door type of sea breeze for sea breeze blowing from Tokyo Bay). The SBF at 3 PM less penetrated to inland for both sea breeze from Sagami Bay and Tokyo Bay.

be seen in Figure 5.20. But for upper part of ABL (850hPa), the wind for cloudline cases is slightly weaker than the non cloudline cases (Figure 5.21).

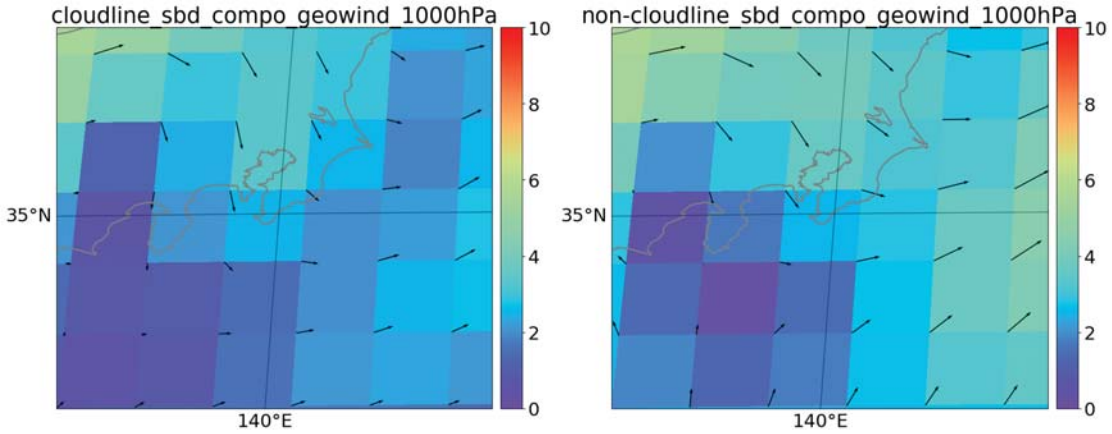

(a) Cloudline cases (b) Non-cloudline cases

Figure 5.18: Composite of geostrophic wind at 1000hPa (ERA-interim). Shaded color indicates the wind speed. Unit is m/s.

Next is to compare the synoptic condition for sea breeze from Sagami Bay and that from Tokyo Bay. Figure 5.22 to Figure 5.26 show the comparison between the synoptic condition (at 9AM and 3PM) for sea breeze blowing from Sagami Bay and that from Tokyo Bay. Ebina and Tokyo site were selected as the reference affected site for each sea breeze.

As can be seen in Figure 5.22, the 1000hPa level of geostrophic wind (at 3PM) for Ebina is slightly stronger than at Tokyo by ∼2 m/s while no significant different for geostrophic wind at 9AM. This indicated that the stronger synoptic wind at Ebina somehow contributed the stronger SBF penetration speed for sea breeze blowing from Sagami Bay (Figure 5.23). This larger portion of the synoptic wind can also be confirmed in vertical profile within ABL (1000hPa to 700hPa level) that shown in Figure 5.24 to Figure 5.26.

5.4.5 SBF speed and wind speed evaluation

As can be seen in the composite map (mean arrival) of the SBF lines (Figure 5.10, Figure 5.11 and Figure 5.12), the final output of the SBF lines were visually represented as the grid or dots, not as the line. The line that detected in this study was quality controlled by considering the exist of cloud pixels in the surrounding. If no cloud in the surrounding, the pixels of those SBF lines were neglected.

The limitation of the method in this study is that "the cloudlines" were not evaluated quantitatively as the "the SBF lines". So it is difficult to derive the pen-

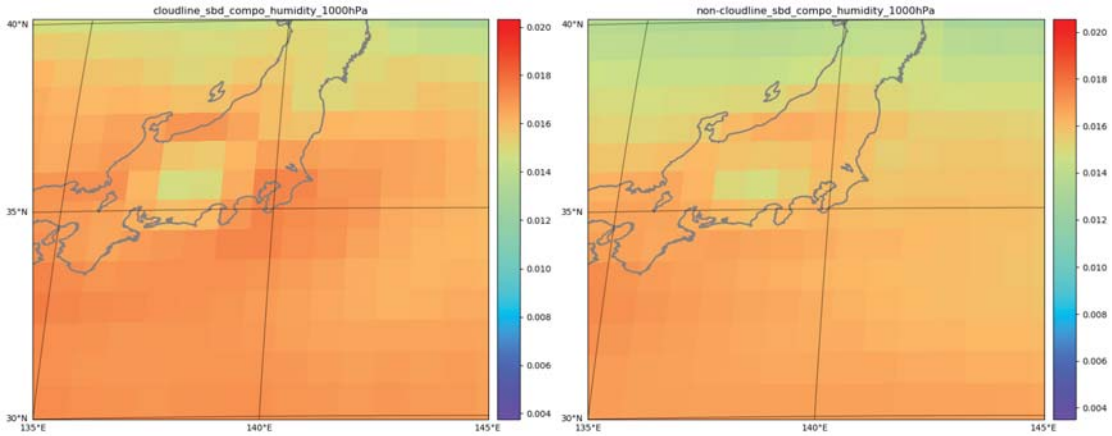

(a) Cloudline cases (b) Non-cloudline cases

Figure 5.19: Composite of humidity at 1000hPa (ERA-interim). Unit=kg/kg

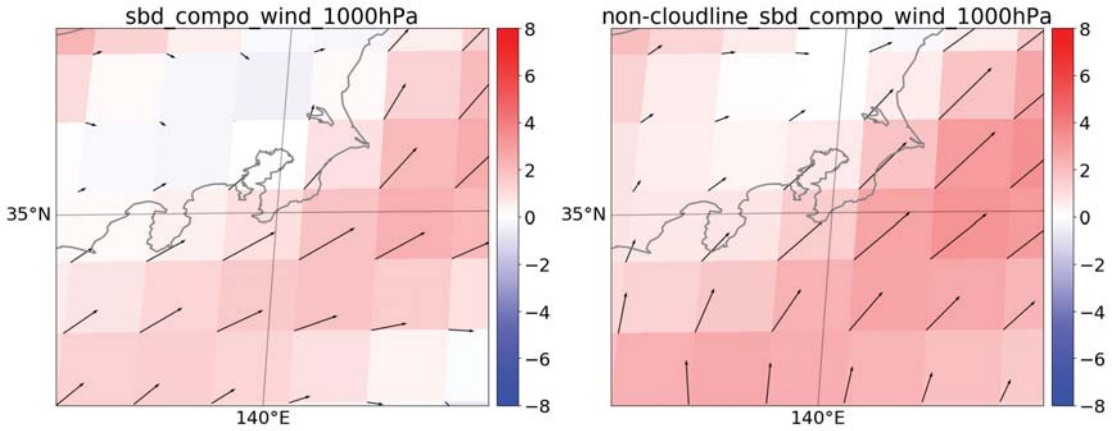

(a) Cloudline cases (b) Non-cloudline cases

Figure 5.20: Composite of the ERA interim wind at lower ABL (1000 hPa). Shaded color depicts the v component. Unit is m/s.

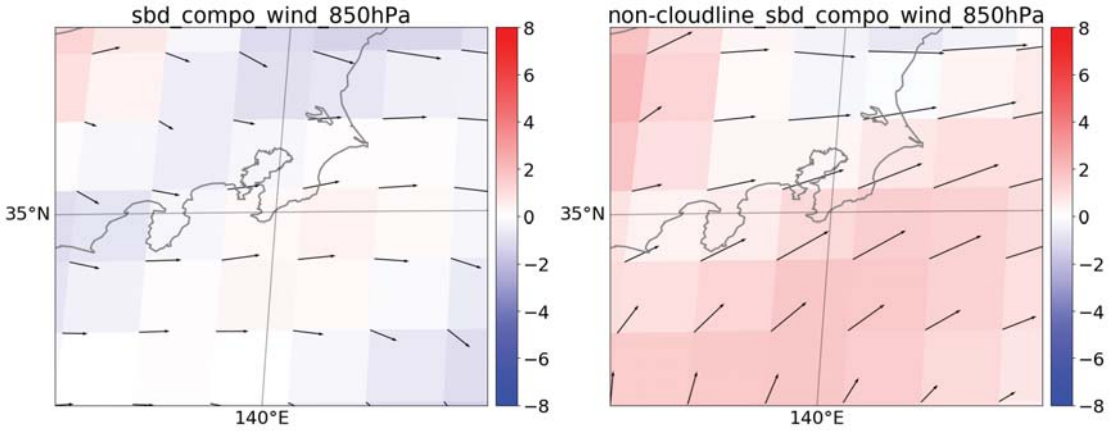

(a) Cloudline cases (b) Non-cloudline cases

Figure 5.21: Composite of the ERA interim wind at upper ABL (850 hPa). Shaded color depicts the v component. Unit is m/s.

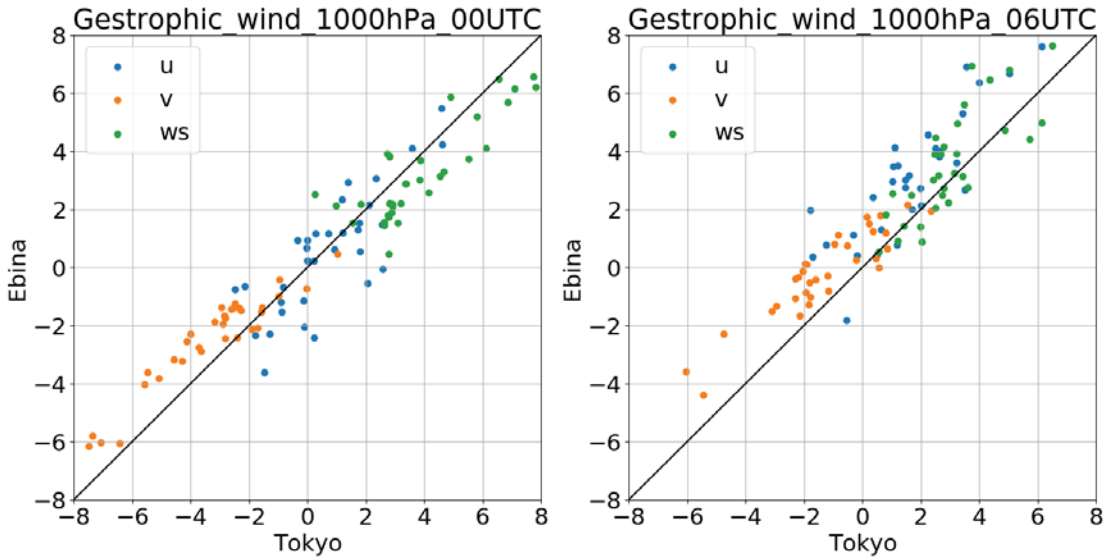

(a) 00UTC (9AM localtime) (b) 06UTC (3PM localtime)

Figure 5.22: Scatter plot of geostrophic wind between Ebina and Tokyo. Unit is in m/s.

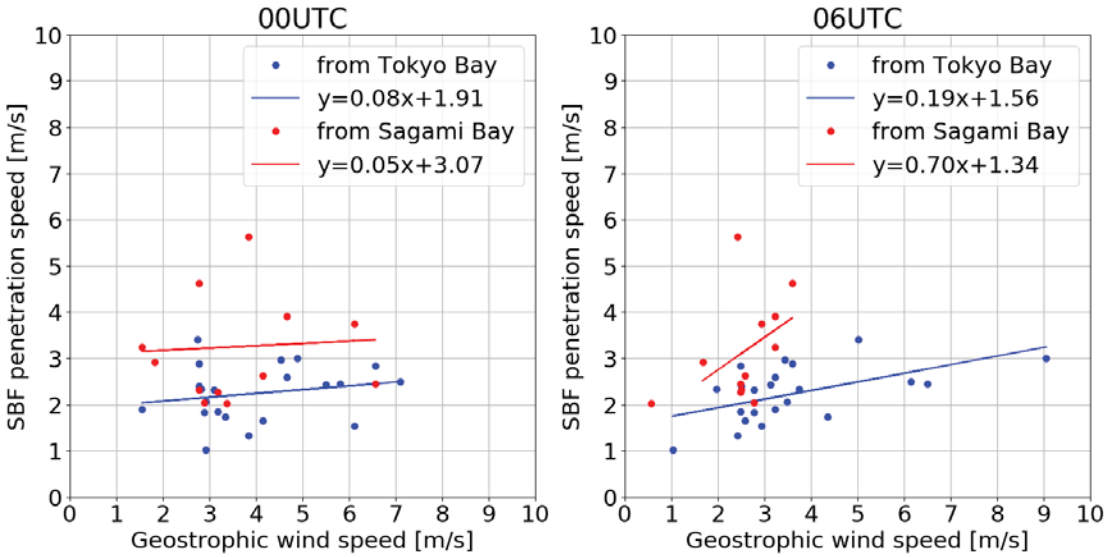

(a) 00UTC (b) 06UTC

Figure 5.23: Comparison between the geostrophic wind speed and SBF penetration speed (for sea breeze blowing from Sagami Bay and Tokyo Bay). Wind speed unit is in m/s. Red (blue) depicts the sea breeze blowing from Sagami Bay (Tokyo Bay).

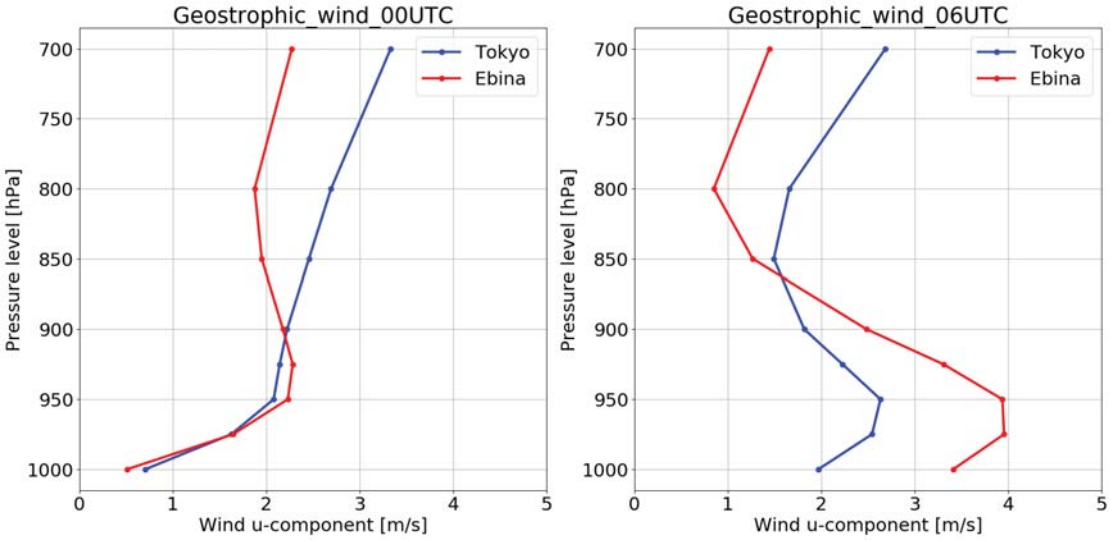

(a) 00UTC (b) 06UTC

Figure 5.24: Vertical u-component of geostrophic wind at Ebina and Tokyo. Unit is in m/s. Red (blue) depicts the sea breeze blowing from Sagami Bay (Tokyo Bay).

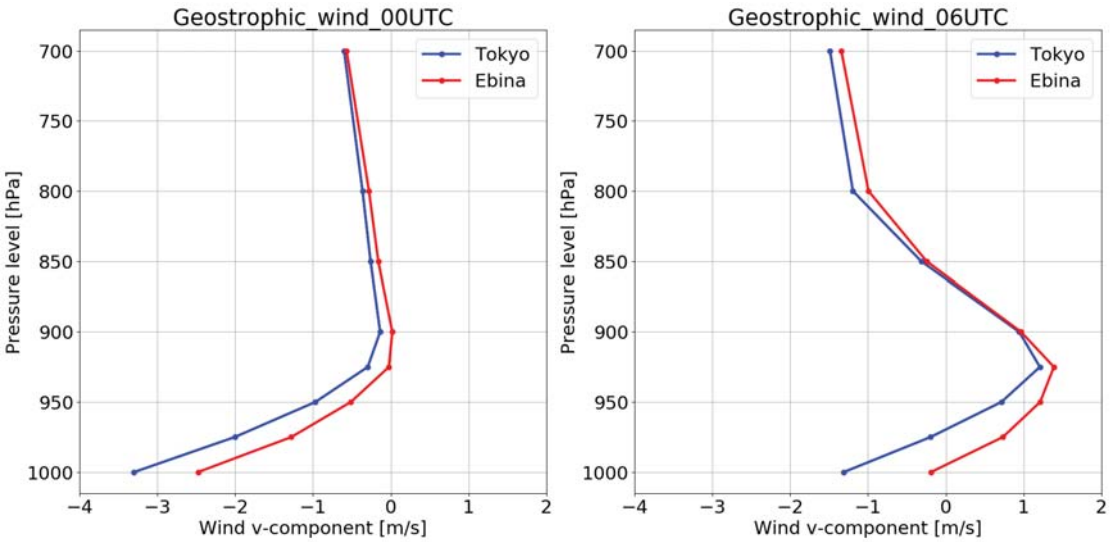

(a) 00UTC (b) 06UTC

Figure 5.25: As same as Figure 5.24 but for v-component.

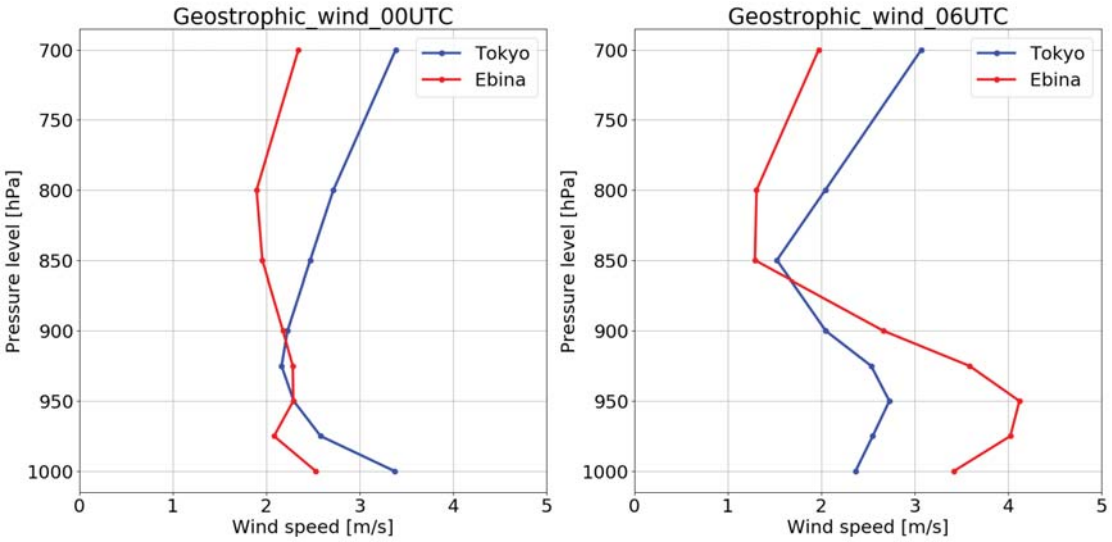

(a) 00UTC (b) 06UTC

Figure 5.26: As same as Figure 5.24 but for wind speed.

etration speed using the propagation speed of the "lines" objectively and directly from the "lines pixels". Further mathematical treatment is needed to be conducted to estimate the front penetration speed from the propagation of lines, or in other word, to evaluate the representative of the line as the front line quantitatively. Nevertheless, it is possible to evaluate objectively the estimated front speed from the arrival time (and cloud passage time) at the observation sites with the wind speed when the sea breeze arrived at those sites. For this, the Ebina and Nerima sites were selected as the reference sites for sea breeze blowing from Sagami Bay and Tokyo Bay, respectively.

Regarding the relationship between SBF penetration speed and the wind speed inside the marine air-mass (i.e., after sea breeze arrival), a review by Miller et al. (2003) described the empirical equations as following.

The laboratory experiment by Keulegan (1957) :

$$|U| = k\sqrt{\frac{\Delta\rho}{\rho}gd} \tag{5.1}$$

where k: 0.87; $|U|$: denser fluid penetration speed into the less-dense; d: the height of the front.

And also in the laboratory experiment by Simpson and Britter (1980), they determined that the propagation speed is slowed by $\sim$3/5 of the opposing prevailing wind:

$$|U| = k\sqrt{\frac{\Delta T}{T}g\bar{d}} - 0.59u_g \tag{5.2}$$

where k: 0.62; $\bar{d}$: mean SB head; u_g: cross-shore geostrophic wind.

Regarding the wind speed of sea breeze, Mathews (1982) proposed the forecast rule using the regression relationship between wind speed of sea breeze (U) and the land-sea temperature difference (ΔT):

$$|U| = \frac{1}{2}\sqrt{\Delta T} \tag{5.3}$$

Simpson (1969) adapted the above forecast into the atmospheric front and Simpson and Britter (1980) modified the equation into:

$$u_{front} \approx 0.87u_{SB} - 0.59u_g \tag{5.4}$$

As can be confirmed from Equation 5.4 that the SBF will penetrate faster when wind speed (see breeze) increases. And the opposing flow of the prevailing wind will slow the front penetration.

Figure 5.27 shows the scatter plot of the wind speed at Ebina (a reference site for sea breeze from Sagami Bay) and Tokyo (a reference site for sea breeze

from Tokyo Bay) with the sea breeze penetration speed derived from cloudline (Figure 5.27a) and that from the observation (Figure 5.27b), respectively. The front speed and the wind speed have the positive relationship as predicted in the Eq. 5.4. In addition, the different gradient between sea breeze from Tokyo Bay and Sagami Bay indicated that there might be other factors which may cause why SBF penetrated slower for SB from Tokyo Bay rather than only the factor of the wind speed.

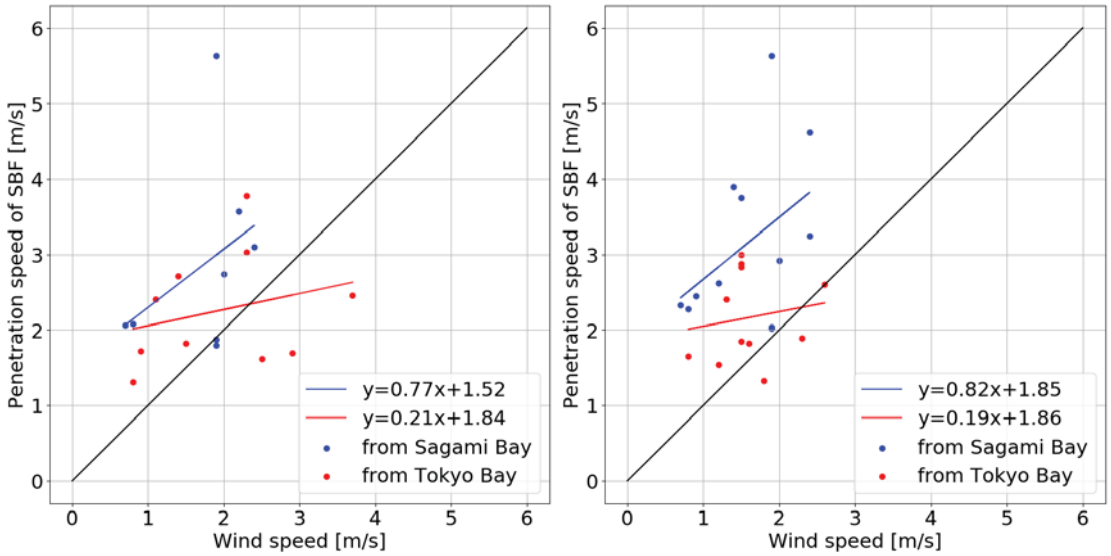

(a) Front speed derived from cloudline (b) Front speed derived from observation

Figure 5.27: Comparison of SBF penetration speed and the wind speed. Blue (red) depicts the wind speed at Ebina (Tokyo) as the reference site for sea breeze arrival from Sagami Bay (Tokyo Bay).

5.5 Discussion

Similar to Jakarta case, the results of Tokyo case also revealed that the detected cumulus cloudlines were able to represent the location of the SBF. The passage time of the cloudline and the arrival time of SBF have bias +/- 20 minutes within 3 km distance. The composite of the time evolution of the detected cloudlines provided spatial inland penetration of the SBF for two sea breeze systems in Tokyo region (blowing from Sagami Bay and that from Tokyo Bay). The mean penetration distance at 3PM was 45 km and 28 km for sea breeze from Sagami Bay and Tokyo Bay, respectively. And the mean penetration speed was estimated to be 2.8 ms^{-1} and 1.8 ms^{-1}, respectively. The reason for this different penetration distance

and speed for both sea breezes may be attributed to several possible mechanisms relating to the large scale and the local scale perspective.

In the large scale perspective, is the direction of the background prevailing wind and the coastline orientation of Sagami Bay and Tokyo Bay. Based on the prevailing wind and coastline orientation, there are three types of sea breeze, namely pure, corkscrew and backdoor sea breeze (Adams, 1997; Miller et al., 2003). In pure sea breeze type the synoptic scale pressure gradient force (PGF) and thermal PGF are in the same dimension. The calm condition is the typical signal during onset time of sea breeze circulation in the pure sea breeze. In the corkscrew and backdoor sea breeze, the prevailing wind has along-coast and cross-coast component. For Tokyo Bay, when the prevailing wind is dominant from northwest (southwest), the sea breeze is backdoor (corkscrew) type (by considering that the coast is located in the northern hemisphere). The corkscrew sea breeze is able to penetrate more than backdoor type even with the small thermal PGF. Compared to the corkscrew sea breeze, the backdoor sea breeze is much weaker and arrives later in the day over inland (Adams, 1997; Miller et al., 2003).

In the local scale perspective, is the heat released from the surface. Sea breeze is a local circulation which induced by the thermal gradient between land and sea. The excess amount of heating (e.g., as sensible heat) over the land surface might impact the inland penetration of sea breeze (e.g. urban heat island (UHI), Yoshikado and Kondo, 1989; Kanda et al., 2001). The sensible heat flux is more produced over urban surface. The sea surface temperature is also one factor that influence the air temperature over urban area in Tokyo as studied by e.g., Oda and Kanda (2009). The deep analysis of quantifying the urban impact is out of the scope of the current study. However, the numerical simulation by changing the land surface of area around Sagami Bay from less-urbanized into intense urbanized area (vice versa for area affected by sea breeze from Tokyo Bay) may give insights to prove this hypothesis.

Regarding the urban impact, in addition to the thermal, the mechanical effect such as due to the surface roughness might cause the slower penetration speed of the SBF (e.g.,Yoshikado (1994); Varquez et al. (2015)). And it is also reported by Thielen et al. (2000); Kusaka et al. (2019) that rather than surface roughness, the sensible heat flux is more significant to the convergence mechanism. These findings suggest the contribution portion (of the urban impact) between the large scale and local scale phenomena.

The composite of the inland penetration revealed the different penetration distance and speed between sea breeze from Sagami Bay and Tokyo Bay. And the spatial different was also seen for area affected by sea breeze from Tokyo Bay. However, some few cases also showed the no significant different between the area that generally affected by sea breeze from Sagami Bay and that from Tokyo Bay or

between urbanized and less-urbanized (which more to local scale area, especially for area affected by sea breeze from Tokyo Bay). This may suggests the two stage of the scale interaction (Yoshikado, 2013) in the spatial characteristic of inland penetration of the sea breeze front with the various scale from synoptic to local scale mechanisms.

5.6 Summary

This chapter presents the application of the proposed framework to provide sea breeze information for Tokyo region. In Tokyo, two sea-breeze systems were detected, one coming from Sagami Bay (in the south side) and another from Tokyo Bay (in the southeast side). When sea breeze from both sides dominates, a convergence zone was formed over Miura peninsula and it penetrated northward. The average inland penetration speed of SBF for sea-breeze from Sagami Bay and Tokyo Bay were estimated to be 2.8 ms^{-1} and 1.8 ms^{-1}, respectively. The current results support previous findings regarding the impact of synoptic-regional wind, UHI, and surface roughness to the inland penetration of sea breeze and the associated cloud formation.

Chapter 6

Concluding remarks

6.1 Introduction

This chapter aims to summarize all the works described in previous chapters.

The general motivation of this study is to utilize the potential benefit of the new generation of geostationary satellite measurement for monitoring the Atmospheric Boundary Layer (ABL) scale phenomena. As the lowest part of the atmosphere, many factors of the earth's surface beneath influenced the ABL. It is necessary to monitor the ABL process to understand the condition of the ABL since many meteorological processes occur within this layer. In remote sensing approaches, monitoring by satellite is commonly used due to its wide spatial coverage. The scale of the phenomena that can be observed is the synoptic to mesoscale. One of them is the propagation and time evolution of the fronts. The satellite observes the cloudiness feature associated with those fronts. The sea-breeze front (SBF) is the smaller mesoscale front type which is usually formed when sea breeze penetrates to the inland. Sea breeze occurs in the almost coastal region over the world. Since most of the megacities are located near a coastal region, the sea breeze event is closely related to the human living environment such as thermal comfort and air ventilation.

As the new generation of a geostationary satellite, the Himawari-8 satellite has higher spatial and temporal resolution than its predecessor, from 1 km to 0.5 km and from hourly to every 10-min, respectively. This is very potential to be explored for observing ABL scale phenomena such as sea breeze. The general objective of this study is to construct a framework for investigating the spatial characteristic of the SBF inland-penetration distance and speed over coastal urban regions. The SBF is identified by the cumulus cloud-line which is detected from the visible band images of the Himawari-8 geostationary satellite. The framework includes the application of morphological snakes algorithm for automated detection of the

cloud-line. And to examine the representatives of the cloud-lines as the SBF proxy, the validation was undertaken using the arrival time of SBF which is obtained from ground observation data.

This study also aims to address the automated detection and computation time for deriving the 2-D spatial distribution of inland penetration of the SBF. By using a 10-min visible band of satellite images, the simple, fast and stable calculation can be performed with near-real-time processing procedures. Moreover, the global applicability of the proposed framework is also expected in order to be able to be used for sea breeze studies at any coastal region in the world using various new generation of geostationary satellites that currently available.

6.2 Research findings

The major findings addressed in this study that have been mentioned in previous chapters, can be summarized as following.

1. The representation of cloud-lines to be used as a proxy for SBF locations was examined. For both Jakarta and Tokyo, the results show that the passage of cloud-lines could represent the arrival time of the SBF with a bias of 20 minutes and within 3 km distance.

2. For Jakarta case, the mean penetration speed obtained from the cloud-lines passage was slightly slower than that estimated from the arrival time of SBF (1.4 ms^{-1} and 1.5 ms^{-1}, respectively).

3. The mean penetration distance at 3 PM local time for Jakarta case were found to be 40 km and 25 km over less urbanized area and that over more urbanized area, respectively.

4. For Tokyo case, two sea-breeze systems were detected. The average sea-breeze inland penetration speed was estimated to be 2.8 m/s and 1.8 m/s for sea breeze from Sagami Bay and Tokyo Bay, respectively.

5. The mean penetration distance at 3 PM local time for Tokyo case were found to be 45 km and 28 km for sea breeze from Sagami Bay and that from Tokyo Bay, respectively.

6. Compared to Jakarta case, the overall inland penetration speed of SBF over Tokyo was slightly larger than Jakarta. The main reason for this, the magnitude of the mean wind and the orientation of the synoptic prevailing wind to the direction of the sea-breeze penetration can be considered.

7. However, similarly to Jakarta case, the long-lasting cumulus cloud appeared over urbanized area of Tokyo. Moreover, for Tokyo case, the different penetration speed of SBF over urbanized area and less-urbanized area can be verified from both the observation and the estimated passage time of the cloud-lines.

8. The current results support previous findings regarding the impact of synoptic regional wind, UHI, and urban roughness to the inland penetration of sea breeze and the associated cloud formation.

6.3 Recommendations for further research

The method in this study is only applicable to sea-breeze events accompanied by the cumulus cloud-lines appearance. This can be seen as the limitation of this study. Nevertheless, considering that sea breeze events with cloud-lines are frequently observed both in the tropics, mid and high latitude areas, the method might be applicable to explore the spatial characteristic of SBF inland penetration at any coastal regions over the world. Method development to analyze the sea breeze flow in the clear-sky condition using infrared band images of the geostationary satellite can also be an interesting topic to be explored.

The combination with the cloud classification algorithm, the cloudiness in the cloud lines can be further examined to predict the possibility of storm clouds (such as Cumulonimbus) formation. Thus, SBF detection can be related to the early warning of severe weather. Further vertical profile examination of the ABL condition, that is beyond the scope of this study, can be possible also be analyzed by combination with turbulence measurement (e.g., tower observation), aerosol and pollutant dispersion, and numerical simulation focused on sea breeze events. And not limited to the cloud line, the edge detection using the morphological snake algorithm can also be widely implemented in other meteorological satellite fields, such as to detect the edge of the smokes due to forest fire and the edge of the volcanic ash impacted area.

6.4 Summary

This study contributes to provide framework to derive inland penetration distance and speed of the sea-breeze front from geostationary satellite images. This is very useful to evaluate how their spatial distribution especially over coastal regions which have limited ground observation data. The author hopes that the method can be implemented not only for research but also for operational purpose such as for sea breeze monitoring in the weather services.

References

Adams, E. (1997). Four ways to win the sea breeze game. *Sailing World*, 3:44.

Anjos, M. and Lopes, A. (2018). Sea breeze front identification on the northeastern coast of brazil and its implications for meteorological conditions in the sergipe region. *Theoretical and Applied Climatology*, pages 1–15.

Arrillaga, J. A., Yagüe, C., Sastre, M., and Román-Cascón, C. (2016). A characterisation of sea-breeze events in the eastern cantabrian coast (spain) from observational data and wrf simulations. *Atmospheric Research*, 181:265–280.

Azorin-Molina, C., Connell, B. H., and Baena-Calatrava, R. (2009a). Sea-breeze convergence zones from avhrr over the iberian mediterranean area and the isle of mallorca, spain. *Journal of Applied Meteorology and Climatology*, 48(10):2069–2085.

Azorin-Molina, C., Sanchez-Lorenzo, A., and Calbo, J. (2009b). A climatological study of sea breeze clouds in the southeast of the iberian peninsula (alicante, spain). *Atmósfera*, 22(1):33–49.

Bessho, K., Date, K., Hayashi, M., Ikeda, A., Imai, T., Inoue, H., Kumagai, Y., Miyakawa, T., Murata, H., Ohno, T., et al. (2016). An introduction to himawari-8/9—japan's new-generation geostationary meteorological satellites. *Journal of the Meteorological Society of Japan. Ser. II*, 94(2):151–183.

Blake, A. and Isard, M. (2012). *Active contours: the application of techniques from graphics, vision, control theory and statistics to visual tracking of shapes in motion*. Springer Science & Business Media.

Borne, K., Chen, D., and Nunez, M. (1998). A method for finding sea breeze days under stable synoptic conditions and its application to the swedish west coast. *International Journal of Climatology*, 18(8):901–914.

Caselles, V., Kimmel, R., and Sapiro, G. (1997). Geodesic active contours. *International journal of computer vision*, 22(1):61–79.

Cenedese, A. and Monti, P. (2003). Interaction between an inland urban heat island and a sea-breeze flow: A laboratory study. *Journal of Applied Meteorology*, 42(11):1569–1583.

Chan, T. F. and Vese, L. A. (2001). Active contours without edges. *IEEE Transactions on image processing*, 10(2):266–277.

Chiba, O. (1993). The turbulent characteristics in the lowest part of the sea breeze front in the atmospheric surface layer. *Boundary-layer meteorology*, 65(1-2):181–195.

Clappier, A., Martilli, A., Grossi, P., Thunis, P., Pasi, F., Krueger, B. C., Calpini, B., Graziani, G., and van den Bergh, H. (2000). Effect of sea breeze on air pollution in the greater athens area. part i: numerical simulations and field observations. *Journal of Applied Meteorology*, 39(4):546–562.

Corpetti, T. and Planchon, O. (2011). Front detection on satellite images based on wavelet and evidence theory: Application to the sea breeze fronts. *Remote sensing of environment*, 115(2):306–324.

Damato, F., Planchon, O., and Dubreuil, V. (2003). A remote-sensing study of the inland penetration of sea-breeze fronts from the english channel. *Weather*, 58(6):219–226.

Darmanto, N. S., Varquez, A. C., and Kanda, M. (2017). Urban roughness parameters estimation from globally available datasets for mesoscale modeling in megacities. *Urban Climate*, 21:243–261.

Dee, D. P., Uppala, S., Simmons, A., Berrisford, P., Poli, P., Kobayashi, S., Andrae, U., Balmaseda, M., Balsamo, G., Bauer, d. P., et al. (2011). The era-interim reanalysis: Configuration and performance of the data assimilation system. *Quarterly Journal of the royal meteorological society*, 137(656):553–597.

Dixon, P. G. and Mote, T. L. (2003). Patterns and causes of atlanta's urban heat island–initiated precipitation. *Journal of Applied Meteorology*, 42(9):1273–1284.

Fan, J., Wang, Y., Rosenfeld, D., and Liu, X. (2016). Review of aerosol–cloud interactions: Mechanisms, significance, and challenges. *Journal of the Atmospheric Sciences*, 73(11):4221–4252.

Ferdiansyah, M. R., Inagaki, A., and Kanda, M. (2017). Thermal image velocimetry application to satellite images during sea-breeze event. *Journal of JSCE B1 (Hydrology)*, 73(4):I_463–I_468.

Ferdiansyah, M. R., Inagaki, A., and Kanda, M. (2020). Detection of sea-breeze inland penetration in the coastal-urban region using geostationary satellite images. *Urban Climate*, 31:100586.

Freitas, E., Rozoff Christopher, M., Cotton William, R., and Silva Dias Pedro, L. (2007). Interactions of an urban heat island and sea-breeze circulations during winter over the metropolitan area of são paulo, brazil. *Boundary-Layer Meteorol*, 122(1):43–65.

Fujita, T. T., Fearl, E. W., and Shenk, W. E. (1975). Satellite-tracked cumulus velocities. *Journal of Applied Meteorology*, 14(3):407–413.

Grossman, R. L. (1982). An analysis of vertical velocity spectra obtained in the bomex fair-weather, trade-wind boundary layer. *Boundary-Layer Meteorology*, 23(3):323–357.

Hadi, T. W., Horinouchi, T., Tsuda, T., Hashiguchi, H., and Fukao, S. (2002). Sea-breeze circulation over jakarta, indonesia: A climatology based on boundary layer radar observations. *Monthly Weather Review*, 130(9):2153–2166.

Hadi, T. W., Tsuda, T., Hashiguchi, H., and Fukao, S. (2000). Tropical sea-breeze circulation and related atmospheric phenomena observed with l-band boundary layer radar in indonesia. *Journal of the Meteorological Society of Japan. Ser. II*, 78(2):123–140.

Hai, S., Miao, Y., Sheng, L., Wei, L., and Chen, Q. (2018). Numerical study on the effect of urbanization and coastal change on sea breeze over qingdao, china. *Atmosphere*, 9(9):345.

Helmis, C., Asimakopoulos, D., Deligiorgi, D., and Lalas, D. (1987). Observations of sea-breeze fronts near the shoreline. *Boundary-layer meteorology*, 38(4):395–410.

Hu, X.-M. and Xue, M. (2016). Influence of synoptic sea-breeze fronts on the urban heat island intensity in dallas–fort worth, texas. *Monthly Weather Review*, 144(4):1487–1507.

Hughes, C. P. and Veron, D. E. (2018). A characterization of the delaware sea breeze using observations and modeling. *Journal of Applied Meteorology and Climatology*, 57(7):1405–1421.

Igel, A. L., Heever, S. C., and Johnson, J. S. (2018). Meteorological and land surface properties impacting sea breeze extent and aerosol distribution in a dry environment. *Journal of Geophysical Research: Atmospheres*, 123(1):22–37.

Inoue, T. and Kimura, F. (2004). Urban effects on low-level clouds around the tokyo metropolitan area on clear summer days. *Geophysical Research Letters*, 31(5).

Kanda, M., Inagaki, A., Miyamoto, T., Gryschka, M., and Raasch, S. (2013). A new aerodynamic parametrization for real urban surfaces. *Boundary-layer meteorology*, 148(2):357–377.

Kanda, M., Inoue, Y., and Uno, I. (2001). Numerical study on cloud lines over an urban street in tokyo. *Boundary-Layer Meteorology*, 98(2):251–273.

Kass, M., Witkin, A., and Terzopoulos, D. (1988). Snakes: Active contour models. *International journal of computer vision*, 1(4):321–331.

Keulegan, G. (1957). An experimental study of the motion of saline water from locks into fresh water channels. *Nat. Bur. Stand. Rept. Technical Report*, 5168.

Kusaka, H., Nishi, A., Mizunari, M., and Yokoyama, H. (2019). Urban impacts on the spatiotemporal pattern of short-duration convective precipitation in a coastal city adjacent to a mountain range. *Quarterly Journal of the Royal Meteorological Society*, 145(722):2237–2254.

Kusuda, M. and Alpert, P. (1983). Anti-clockwise rotation of the wind hodograph. part i: Theoretical study. *Journal of the atmospheric sciences*, 40(2):487–499.

Liu, G., Sun, J., and Jiang, W. (2009). Observational verification of urban surface roughness parameters derived from morphological models. *Meteorological Applications: A journal of forecasting, practical applications, training techniques and modelling*, 16(2):205–213.

Marquez-Neila, P., Baumela, L., and Alvarez, L. (2014). A morphological approach to curvature-based evolution of curves and surfaces. *IEEE Transactions on Pattern Analysis and Machine Intelligence*, 36(1):2–17.

Mathews, J. (1982). The sea-breeze—forecasting aspects. *Aust. Meteorol. Mag*, 30:205–209.

Miller, S., Keim, B., Talbot, R., and Mao, H. (2003). Sea breeze: Structure, forecasting, and impacts. *Reviews of geophysics*, 41(3).

Naor, R., Potchter, O., Shafir, H., and Alpert, P. (2017). An observational study of the summer mediterranean sea breeze front penetration into the complex topography of the jordan rift valley. *Theoretical and applied climatology*, 127(1-2):275–284.

Ng, E., Yuan, C., Chen, L., Ren, C., and Fung, J. C. (2011). Improving the wind environment in high-density cities by understanding urban morphology and surface roughness: a study in hong kong. *Landscape and Urban planning*, 101(1):59–74.

Oda, R. and Kanda, M. (2009). Observed sea surface temperature of tokyo bay and its impact on urban air temperature. *Journal of Applied Meteorology and Climatology*, 48(10):2054–2068.

Ogawa, S., Sha, W., Iwasaki, T., and Wang, Z. (2003). A numerical study on the interaction of a sea-breeze front with convective cells in the daytime boundary layer. *Journal of the Meteorological Society of Japan. Ser. II*, 81(4):635–651.

Oke, T. (1995). The heat island of the urban boundary layer: characteristics, causes and effects. *Wind Climate in Cities*, pages 81–107.

Osher, S. and Sethian, J. A. (1988). Fronts propagating with curvature-dependent speed: algorithms based on hamilton-jacobi formulations. *Journal of computational physics*, 79(1):12–49.

Ottenbacher, A., Tomassini, M., Holmlund, K., and Schmetz, J. (1997). Low-level cloud motion winds from meteosat high-resolution visible imagery. *Weather and Forecasting*, 12(1):175–184.

Papanastasiou, D. K., Melas, D., Bartzanas, T., and Kittas, C. (2010). Temperature, comfort and pollution levels during heat waves and the role of sea breeze. *International journal of biometeorology*, 54(3):307–317.

Planchon, O. and Cautenet, S. (1997). Rainfall and sea-breeze circulation over south-western france. *International journal of climatology*, 17(5):535–549.

Planchon, O., Damato, F., Dubreuil, V., and Gouéry, P. (2006). A method of identifying and locating sea-breeze fronts in north-eastern brazil by remote sensing. *Meteorological Applications*, 13(3):225–234.

Prtenjak, M. T., Pasarić, Z., Orlić, M., and Grisogono, B. (2008). Rotation of sea/land breezes along the northeastern adriatic coast. In *Annales Geophysicae*, volume 26, pages 1711–1724. Copernicus GmbH.

Ribeiro, F. N., de Oliveira, A. P., Soares, J., de Miranda, R. M., Barlage, M., and Chen, F. (2018). Effect of sea breeze propagation on the urban boundary layer of the metropolitan region of sao paulo, brazil. *Atmospheric research*, 214:174–188.

Sasaki, Y., Matsuo, K., Yokoyama, M., Sasaki, M., Tanaka, T., and Sadohara, S. (2018). Sea breeze effect mapping for mitigating summer urban warming: For making urban environmental climate map of yokohama and its surrounding area. *Urban climate*, 24:529–550.

Shepherd, J. M. and Burian, S. J. (2003). Detection of urban-induced rainfall anomalies in a major coastal city. *Earth Interactions*, 7(4):1–17.

Shiraki, M. (1986). Counterclockwise rotation of wind hodographs of sea and land breezes in the kanto plain. *Journal of the Meteorological Society of Japan. Ser. II*, 64(1):155–160.

Simpson, J. (1969). A comparison between laboratory and atmospheric density currents. *Quarterly Journal of the Royal Meteorological Society*, 95(406):758–765.

Simpson, J. and Britter, R. (1980). A laboratory model of an atmospheric mesofront. *Quarterly Journal of the Royal Meteorological Society*, 106(449):485–500.

Simpson, J. E. (1994). *Sea breeze and local winds*. Cambridge University Press.

Simpson, M., Warrior, H., Raman, S., Aswathanarayana, P., Mohanty, U., and Suresh, R. (2007). Sea-breeze-initiated rainfall over the east coast of india during the indian southwest monsoon. *Natural Hazards*, 42(2):401–413.

Stephan, K., Kraus, H., Ewenz, C., and Hacker, J. (1999). Sea-breeze front variations in space and time. *Meteorology and Atmospheric Physics*, 70(1-2):81–95.

Stull, R. B. (2012). *An introduction to boundary layer meteorology*, volume 13. Springer Science & Business Media.

Taniguchi, H., Otani, K., and Kurokawa, K. (2001). Hourly forecast of global irradiation using gms satellite images. *Solar energy materials and solar cells*, 67(1-4):551–557.

Teuling, A. J., Taylor, C. M., Meirink, J. F., Melsen, L. A., Miralles, D. G., Van Heerwaarden, C. C., Vautard, R., Stegehuis, A. I., Nabuurs, G.-J., and de Arellano, J. V.-G. (2017). Observational evidence for cloud cover enhancement over western european forests. *Nature communications*, 8:14065.

Theeuwes, N. E., Barlow, J. F., Teuling, A. J., Grimmond, C. S. B., and Kotthaus, S. (2019). Persistent cloud cover over mega-cities linked to surface heat release. *npj Climate and Atmospheric Science*, 2(1):15.

Thielen, J., Wobrock, W., Gadian, A., Mestayer, P., and Creutin, J.-D. (2000). The possible influence of urban surfaces on rainfall development: a sensitivity study in 2d in the meso-γ-scale. *Atmospheric Research*, 54(1):15–39.

Thompson, W. T., Holt, T., and Pullen, J. (2007). Investigation of a sea breeze front in an urban environment. *Quarterly Journal of the Royal Meteorological Society: A journal of the atmospheric sciences, applied meteorology and physical oceanography*, 133(624):579–594.

United-Nations (2018). World urbanization prospects. *Department of Economic and Social Affairs, United Nation, New York*.

Varquez, A. C. G., Nakayoshi, M., and Kanda, M. (2015). The effects of highly detailed urban roughness parameters on a sea-breeze numerical simulation. *Boundary-layer meteorology*, 154(3):449–469.

Wang, Y., Di Sabatino, S., Martilli, A., Li, Y., Wong, M., Gutiérrez, E., and Chan, P. (2017). Impact of land surface heterogeneity on urban heat island circulation and sea-land breeze circulation in hong kong. *Journal of Geophysical Research: Atmospheres*, 122(8):4332–4352.

Yagi, A., Inagaki, A., Kanda, M., Fujiwara, C., and Fujiyoshi, Y. (2017). Nature of streaky structures observed with a doppler lidar. *Boundary-layer meteorology*, 163(1):19–40.

Yoshikado, H. (1994). Interaction of the sea breeze with urban heat islands of different sizes and locations. *Journal of the Meteorological Society of Japan. Ser. II*, 72(1):139–143.

Yoshikado, H. (2013). Intense summer heat in tokyo and its suburban areas related with variation in the synoptic-scale pressure field: A statistical analysis. *Journal of applied meteorology and climatology*, 52(9):2065–2074.

Yoshikado, H. and Kondo, H. (1989). Inland penetration of the sea breeze over the suburban area of tokyo. *Boundary-Layer Meteorology*, 48(4):389–407.

Zhou, Y., Guan, H., Huang, C., Fan, L., Gharib, S., Batelaan, O., and Simmons, C. (2019). Sea breeze cooling capacity and its influencing factors in a coastal city. *Building and Environment*, 166:106408.

Zhuge, X.-y., Yu, F., and Wang, Y. (2012). A new visible albedo normalization method: quasi-lambertian surface adjustment. *Journal of Atmospheric and Oceanic Technology*, 29(4):589–596.

Appendix A

Python Scripts

A.1 SBD screening

The following code is for SBD screening:

```
import pandas as pd
import datetime
import matplotlib.pyplot as plt
import numpy as np
import os
from scipy.signal import argrelextrema
from matplotlib.dates import HourLocator, MinuteLocator,
    DateFormatter
from pandas.plotting import register_matplotlib_converters

register_matplotlib_converters()
plt.rcParams.update({'font.size': 22})

def read_timeseries(fn):
    df = pd.read_csv(fn)
    df['localtime'] = pd.to_datetime(df['localtime'],format='%Y-%m
    -%d %H:%M:%S')
    df = df.set_index('localtime')
    return df

def screening_wd(df):
    df['wd_flag'] = np.where(((df['wd']>=315) | (df['wd']<=45)),1,
    np.nan)
    labels = (df['wd_flag'].diff().ne(0) | df.id.diff().ne(0)).
    cumsum()
    df['flag'] = (labels.map(labels.value_counts()) >= 12).astype(
    int) #12 : at least sustain for two hour
    df['flag'] = np.where(df['flag']==0,np.nan,df['flag'])
    return df
```

```
25
26 def outlist_sbd(df0,sta = 'BPL'):
27     a1 = datetime.datetime(2017,7,1)
28     a2 = datetime.datetime(2018,9,30)
29     dt = pd.date_range(start=a1,end=a2,freq='1D')
30
31     sbd = []
32     non_sbd = []
33     for i in xrange(len(dt)):
34         a = dt[i]
35         if a.month <7 or a.month>9:continue
36         df = df0.loc[a.strftime('%Y-%m-%d 09:00'):a.strftime('%Y-%
    m-%d 15:00')]
37         df = screening_wd(df)
38         if df['flag'].sum()==0 : non_sbd.append(a)
39         if df['flag'].sum()!=0 : sbd.append(a)
40
41     print len(sbd),len(non_sbd)
42
43     sbd = pd.DataFrame(data=sbd,columns=['localtime'])
44     hoge = sbd.to_csv('..\\input_txt\\'+sta+'_sbd.csv',index=None,
    header=True)
45     non_sbd = pd.DataFrame(data=non_sbd,columns=['localtime'])
46     hoge = non_sbd.to_csv('..\\input_txt\\'+sta+'_non_sbd.csv',
    index=None,header=True)
47     return sbd, non_sbd
48
49 def compo_eachtime(df1,df2,cols_name='SBD'):
50     df = df1[df1['date'].isin(df2.index.date)]
51     df = df.drop('date',axis=1)
52
53     ave = df.groupby([df.index.hour,df.index.minute],axis=0).mean
    ()
54     ave.columns = [cols_name]
55
56     return  ave
57
58 def main01():
59     dd = '..\\data_txt'
60     fn = os.path.join(dd,'kkp_jas_latest.csv')
61     df1 = read_timeseries(fn)
62     fn = os.path.join(dd,'bpl_jas_latest.csv')
63     df2 = read_timeseries(fn)
64
65     sbd1, non_sbd1 = outlist_sbd(df1,sta = 'KKP')
66     sbd2, non_sbd2 = outlist_sbd(df2,sta = 'BPL')
67
68     sbd1['kkp'] = 1
69     sbd1 = sbd1.set_index('localtime')
```

```
70      sbd2['bpl'] = 1
71      sbd2 = sbd2.set_index('localtime')
72
73      df = pd.concat([sbd1,sbd2],axis=1)
74      df = df.dropna()
75      df = df.reset_index()
76      df = df.drop(['kkp','bpl'],axis=1)
77      hoge = df.to_csv('..\\input_txt\\KKP_BPL_sbd_list.csv',index=
        None,header=True)
78      print len(df.index)
79
80      non_sbd1['kkp'] = 0
81      non_sbd1 = non_sbd1.set_index('localtime')
82      non_sbd2['bpl'] = 0
83      non_sbd2 = non_sbd2.set_index('localtime')
84
85      df = pd.concat([non_sbd1,non_sbd2],axis=1)
86      df = df.dropna()
87      df = df.reset_index()
88      df = df.drop(['kkp','bpl'],axis=1)
89      hoge = df.to_csv('..\\input_txt\\KKP_BPL_nonsbd_list.csv',
        index=None,header=True)
90      print len(df.index)
91
92      return
93
94  def main02():
95      sta = 'KKP'
96      dd = '..\\data_txt'
97      fn = os.path.join(dd,sta+'_jas_latest.csv')
98      df1 = read_timeseries(fn)
99
100     dd = '..\\input_txt'
101     fn = os.path.join(dd,'KKP_BPL_sbd_list.csv')
102     df2 = read_timeseries(fn)
103
104     dd = '..\\input_txt'
105     fn = os.path.join(dd,'KKP_BPL_nonsbd_list.csv')
106     df3 = read_timeseries(fn)
107
108     df1 = df1['t'].to_frame('t')
109     df1['date'] = df1.index.date
110     print len(df1)
111
112     ave1 = compo_eachtime(df1,df2,cols_name='SBD')
113     ave2 = compo_eachtime(df1,df3,cols_name='Non-SBD')
114
115     fig, ax = plt.subplots(figsize=(20,8))
116     ave1.plot(ax=ax)
```

```
117     ave2.plot(ax=ax)
118     ax.grid()
119     plt.title(sta,fontsize=24)
120     plt.xlabel('Time (hour, minute)', fontsize=24)
121     plt.ylabel('Air temperature (deg C)', fontsize=24)
122     fig.savefig(sta+'_compo_sbd_non.png',bbox_inches='tight')
123     return
124 
125 def plot_single(df,stamp,sta='KKP'):
126     fig, ax = plt.subplots(figsize=(15,6))
127     ax.plot(df['e_sp'],'o-')
128     ax.set_title(stamp)
129     #ax.set_ylim(26,36)
130     ax.set_ylim(10,20)
131     ax.grid()
132     ax.xaxis.set_major_locator(HourLocator(interval=1)) # tick
    every one hours
133     ax.xaxis.set_minor_locator(MinuteLocator(interval=10)) # tick
    every ten minutes
134     ax.xaxis.set_major_formatter(DateFormatter('%H:%M'))
135     fout = os.path.join('..\\output_png',stamp+'.png')
136     fig.savefig(fout,bbox_inches='tight')
137     plt.close(fig)
138     return
139 
140 def plot_t_esp(df,stamp,sta='KKP'):
141     fig, ax = plt.subplots(figsize=(15,6))
142     ax1 = df['t'].plot(marker='o',color='r',grid=True)
143     ax2 = df['e_sp'].plot(marker='o',color='b',secondary_y=True,
    grid=True)
144     h1, l1 = ax1.get_legend_handles_labels()
145     h2, l2 = ax2.get_legend_handles_labels()
146     ax.legend(h1+h2, l1+l2, loc=2)
147     ax1.set_ylim(26,36)
148     ax2.set_ylim(10,20)
149     ax1.set_ylabel('Air temperature [deg C]')
150     ax2.set_ylabel('Specific humidity [g/kg]')
151     plt.title(sta+'_'+stamp)
152     fout = os.path.join('..\\output_png',sta+'_'+stamp+'.png')
153     fig.savefig(fout,bbox_inches='tight')
154     plt.close(fig)
155     return
156 
157 def plot_uv(df,stamp,sta='KKP'):
158     fig, ax = plt.subplots(figsize=(15,6))
159     ax1 = df['u'].plot(marker='o',color='r',grid=True)
160     ax2 = df['v'].plot(marker='o',color='b',secondary_y=True,grid=
    True)
161     h1, l1 = ax1.get_legend_handles_labels()
```

```
    h2, l2 = ax2.get_legend_handles_labels()
    ax.legend(h1+h2, l1+l2, loc=2)
    ax1.set_ylim(-3,3)
    ax2.set_ylim(-6,6)
    ax1.set_ylabel('u wind component [m/s]')
    ax2.set_ylabel('v wind component [m/s]')
    plt.title(sta+'_'+stamp)
    fout = os.path.join('..\\output_png',sta+'_'+stamp+'.png')
    fig.savefig(fout,bbox_inches='tight')
    plt.close(fig)
    return

def main():
    sta = 'BPL'
    dd = '..\\data_txt'
    fn = os.path.join(dd,sta+'_jas_latest.csv')
    df1 = read_timeseries(fn)
    df1 = df1[(df1.index.hour>=9) & (df1.index.hour<=15)]
    df1['date'] = df1.index.date

    dd = '..\\input_txt'
    fn = os.path.join(dd,'KKP_BPL_sbd_list.csv')
    df2 = read_timeseries(fn)
    dt = df2.index.date
    #print len(dt)

    df0 = df1[df1['date'].isin(dt)]
    #print df0.head()

    for a in dt[0:]:
        stamp = a.strftime('%Y%m%d')
        df = df0[df0['date']==a]
        #if df['e_sp'].sum(axis=0) <=0 : continue
        df = df[['t','e_sp','u','v']]
        #hoge = plot_t_esp(df,stamp,sta=sta)
        hoge = plot_uv(df,stamp,sta=sta)

    return

if __name__ == '__main__':
    main()
```

Listing A.1: Code for SBD screening

A.2 SBF arrival time

The following code is to estimate arrival time of SBF:

```
import pandas as pd
import os
from scipy.signal import argrelextrema
import numpy as np
import matplotlib.pyplot as plt
from pandas.plotting import register_matplotlib_converters

register_matplotlib_converters()
plt.rcParams.update({'font.size': 22})

def read_timeseries(fn):
    df = pd.read_csv(fn)
    df['localtime'] = pd.to_datetime(df['localtime'],format='%Y-%m-%d %H:%M:%S')
    df = df.set_index('localtime')
    return df

##-----------------------------------------------##
####caution: subroutine ini masih harus diperbaiki!!!!
def screening_mentahan(df):
    # Find local peaks
    n=1 # number of points to be checked before and after
    df['t_max'] = df.iloc[argrelextrema(df['t'].values, np.greater_equal, order=n)[0]]['t']
    df['ws_max'] = df.iloc[argrelextrema(df['ws'].values, np.greater_equal, order=n)[0]]['ws']
    if df['e_sp'].mean()>0 :
        df['esp_pct'] = df['e_sp'].pct_change(periods=1)
        df['esp_pct_max'] = df.iloc[argrelextrema(df['esp_pct'].values, np.greater_equal, order=n)[0]]['esp_pct']
        #df['esp_pct_max'] = df['esp_pct_max']*df['flag']

        idx = df['esp_pct_max'].argmax()  - datetime.timedelta(minutes=10)
        tmax_idx = df[df['t_max'].notnull()].index
        idx0 = tmax_idx[tmax_idx.get_loc(idx, method='nearest')]
        if df['t_max'].loc[idx]!= df['t_max'].loc[idx0]  : idx0 = idx0+ datetime.timedelta(minutes=10)

        return idx0
    else:
        print df.index[0].date(), ': NO specific humidity!!!!!!'
        return


```

```
40 def find_arrival(df):
41     n=1 # number of points to be checked before and after
42     df['t_max'] = df.iloc[argrelextrema(df['t'].values, np.
       greater_equal, order=n)[0]]['t']
43     if df['e_sp'].mean()>0 :
44         df['esp_pct'] = df['e_sp'].pct_change(periods=1)
45         df['esp_pct_max'] = df.iloc[argrelextrema(df['esp_pct'].
       values,
46                                                   np.greater_equal
       , order=n)[0]]['esp_pct']
47         df['esp_peak'] = np.nan
48         idx = df['esp_pct_max'].idxmax()
49         df['esp_peak'].loc[idx] = df['e_sp'].loc[idx]
50 
51         tmax_idx = df[df['t_max'].notnull()].index
52         try:
53             idx0 = tmax_idx[tmax_idx.get_loc(idx, method='pad')]
54         except KeyError:
55             idx0 = idx
56     return df,idx0
57 
58 def plot_plot(df,a,sta='KKP'):
59     fig, ax = plt.subplots(figsize=(15,6))
60     ax1 = df['t'].plot(grid=True)
61     ax = df['t_max'].plot(marker='o',grid=True)
62     ax2 = df['e_sp'].plot(secondary_y=True,grid=True)
63     ax = df['esp_peak'].plot(marker='o',secondary_y=True,grid=True
       )
64     h1, l1 = ax1.get_legend_handles_labels()
65     h2, l2 = ax2.get_legend_handles_labels()
66     #ax.legend(h1+h2, l1+l2, loc=2)
67     ax1.set_ylim(26,36)
68     ax2.set_ylim(10,20)
69     ax.axvline(a, color='k', linestyle='--')
70     plt.title(a.strftime(sta+'_%Y-%m-%d_%H:%M'))
71     fout = os.path.join('..\\output_png',a.strftime(sta+'_%Y%m%
       d_arrival.png'))
72     fig.savefig(fout,bbox_inches='tight')
73     plt.close(fig)
74     return
75 
76 def main():
77     sta = 'KKP'
78     dd = '..\\data_txt'
79     fn = os.path.join(dd,sta+'_jas_latest.csv')
80     df1 = read_timeseries(fn)
81     df1 = df1[(df1.index.hour>=9) & (df1.index.hour<=15)]
82     df1['date'] = df1.index.date
83 
```

```
    dd = '..\\input_txt'
    fn = os.path.join(dd,'KKP_BPL_sbd_list.csv')
    df2 = read_timeseries(fn)
    df2.index = df2.index.date
    df2.index.names = ['date']
    df2[sta] = np.nan
    dt = df2.index
    df0 = df1[df1['date'].isin(dt)]

    for a in dt[0:]:
        stamp = a.strftime('%Y%m%d')
        df = df0[df0['date']==a]
        if df['e_sp'].sum(axis=0) <=0 : continue
        df = df[['t','e_sp']]
        df,idx = find_arrival(df)
        df2[sta].loc[a] = idx
        hoge = plot_plot(df,idx,sta=sta)

    sta = 'BPL'
    dd = '..\\data_txt'
    fn = os.path.join(dd,sta+'_jas_latest.csv')
    df1 = read_timeseries(fn)
    df1 = df1[(df1.index.hour>=9) & (df1.index.hour<=15)]
    df1['date'] = df1.index.date

    df0 = df1[df1['date'].isin(dt)]

    df2[sta] = np.nan

    for a in dt[0:]:
        stamp = a.strftime('%Y%m%d')
        df = df0[df0['date']==a]
        if df['e_sp'].sum(axis=0) <=0 : continue
        df = df[['t','e_sp']]
        df,idx = find_arrival(df)
        df2[sta].loc[a] = idx
        hoge = plot_plot(df,idx,sta=sta)

    print df2.head()
    hoge = df2.to_csv('..\\arrival_result_01.csv',index=True,
   header=True)

    return

if __name__ == '__main__':
    main()
```

Listing A.2: Code for SBF arrival time

A.3 Compositing based on SBF arrival time

The following code is to composite:

```
import pandas as pd
import os
import numpy as np
import datetime
import matplotlib.pyplot as plt
from pandas.plotting import register_matplotlib_converters

register_matplotlib_converters()
plt.rcParams.update({'font.size': 22})

def read_timeseries(fn):
    df = pd.read_csv(fn)
    df['localtime'] = pd.to_datetime(df['localtime'],format='%Y-%m-%d %H:%M:%S')
    df = df.set_index('localtime')
    return df

def calc_compo_01(dt,df,sta='KKP',par='t'):
    tmp = pd.DataFrame()
    for a in dt:
        a1=a-datetime.timedelta(minutes=120) #compo 2 hours before and after
        a2=a+datetime.timedelta(minutes=120)
        hoge = df[par].loc[a1:a2].reset_index(drop=True)
        tmp[a] = hoge

    print len(tmp.columns)
    compo = pd.DataFrame()
    compo[par+'_mean'] = tmp.mean(axis=1)
    compo[par+'_std'] = tmp.std(axis=1)

    fig, ax = plt.subplots(figsize=(12,6))
    xs = compo.index - (len(compo.index)/2)
    ax.errorbar(xs,compo[par+'_mean'],yerr=0.25*compo[par+'_std'])
    ax.grid()
    judul = sta+'_'+par+'_arrival_compo'
    plt.title(judul)
    fout = os.path.join('..\\output_png',judul+'.png')
    fig.savefig(fout,bbox_inches='tight')
    plt.close(fig)
    return

def calc_compo(dt,df,sta='KKP',par='t'):
    tmp = pd.DataFrame()
    for a in dt:
```

```
44          a1=a-datetime.timedelta(minutes=60*3) #compo 2 hours
    before and after
45          a2=a+datetime.timedelta(minutes=60*3)
46          hoge = df[par].loc[a1:a2].reset_index(drop=True)
47          tmp[a] = hoge
48      print len(tmp.columns)
49      compo = pd.DataFrame()
50      compo[sta+'_'+par+'_mean'] = tmp.mean(axis=1)
51      compo[sta+'_'+par+'_std'] = tmp.std(axis=1)
52      return compo
53
54  def plot_compo(compo,par='t'):
55      fig, ax = plt.subplots(figsize=(12,8))
56      xs = compo.index - (len(compo.index)/2)
57      sta='KKP'
58      ax.errorbar(xs,compo[sta+'_'+par+'_mean'],yerr=0.25*compo[sta+
    '_'+par+'_std'],color='b',label=sta)
59      sta='BPL'
60      ax.errorbar(xs,compo[sta+'_'+par+'_mean'],yerr=0.25*compo[sta+
    '_'+par+'_std'],color='r',label=sta)
61      ax.grid()
62      ax.legend()
63      judul = par+'_arrival_compo'
64      plt.title(judul)
65      fout = os.path.join('..\\output_png',judul+'.png')
66      fig.savefig(fout,bbox_inches='tight')
67      plt.close(fig)
68      return
69
70  def main01():
71      dd = '..\\output_txt'
72      fn = os.path.join(dd,'arrival_result_01.csv')
73      df = pd.read_csv(fn)
74      df = df.dropna()
75      df['KKP'] = pd.to_datetime(df['KKP'],format='%Y-%m-%d %H:%M:%S
    ')
76      df['BPL'] = pd.to_datetime(df['BPL'],format='%Y-%m-%d %H:%M:%S
    ')
77
78      df['diff'] = np.where(df['KKP'] > df['BPL'],np.nan,1)
79      df = df.dropna()
80      df['diff'] = df['BPL']-df['KKP']
81      df = df[['date','KKP','BPL']]
82      hoge = df.to_csv('..\\arrival_result_02.csv',index=None,header
    =True)
83      return
84
85  def main02():
86      dd = '..\\output_txt'
```

```
87      fn = os.path.join(dd,'arrival_result_02.csv')
88      df = pd.read_csv(fn)
89
90      df['KKP'] = pd.to_datetime(df['KKP'],format='%Y-%m-%d %H:%M:%S
        ')
91      df['BPL'] = pd.to_datetime(df['BPL'],format='%Y-%m-%d %H:%M:%S
        ')
92
93      sta='KKP'
94      dt = df[sta]
95      fn = os.path.join('..\\data_txt',sta+'_jas_latest.csv')
96      df_obs = read_timeseries(fn)
97      print df_obs.head()
98      hoge = calc_compo_01(dt,df_obs,sta=sta,par='t')
99      hoge = calc_compo_01(dt,df_obs,sta=sta,par='e_sp')
100     hoge = calc_compo_01(dt,df_obs,sta=sta,par='ws')
101     hoge = calc_compo_01(dt,df_obs,sta=sta,par='u')
102     hoge = calc_compo_01(dt,df_obs,sta=sta,par='v')
103
104     sta='BPL'
105     dt = df[sta]
106     fn = os.path.join('..\\data_txt',sta+'_jas_latest.csv')
107     df_obs = read_timeseries(fn)
108     print df_obs.head()
109     hoge = calc_compo_01(dt,df_obs,sta=sta,par='t')
110     hoge = calc_compo_01(dt,df_obs,sta=sta,par='e_sp')
111     hoge = calc_compo_01(dt,df_obs,sta=sta,par='ws')
112     hoge = calc_compo_01(dt,df_obs,sta=sta,par='u')
113     hoge = calc_compo_01(dt,df_obs,sta=sta,par='v')
114     return
115
116 def main():
117     dd = '..\\output_txt'
118     fn = os.path.join(dd,'arrival_result_02.csv')
119     df = pd.read_csv(fn)
120
121     df['KKP'] = pd.to_datetime(df['KKP'],format='%Y-%m-%d %H:%M:%S
        ')
122     df['BPL'] = pd.to_datetime(df['BPL'],format='%Y-%m-%d %H:%M:%S
        ')
123
124     par = 't'
125     sta='KKP'
126     dt = df[sta]
127     fn = os.path.join('..\\data_txt',sta+'_jas_latest.csv')
128     df_obs1 = read_timeseries(fn)
129     compo1 = calc_compo(dt,df_obs1,sta=sta,par=par)
130
131     sta='BPL'
```

```
132     dt = df[sta]
133     fn = os.path.join('..\\data_txt',sta+'_jas_latest.csv')
134     df_obs2 = read_timeseries(fn)
135     compo2 = calc_compo(dt,df_obs2,sta=sta,par=par)
136 
137     compo = pd.concat([compo1,compo2],axis=1)
138     hoge = plot_compo(compo,par=par)
139     return
140 
141 if __name__ == '__main__':
142     main()
```

Listing A.3: Code for composite based on SBF arrival time

A.4 Plotting B03 to check

The following code is to plot the array:

```
import pandas as pd
import os
import matplotlib.pyplot as plt
import numpy as np
import datetime
from pandas.plotting import register_matplotlib_converters

register_matplotlib_converters()
plt.rcParams.update({'font.size': 22})

def df2array(df):
    df = df.unstack().transpose()
    img = df.values
    return img

def get_vis_Bxx(a,ch='B03'):
    dd='D:\\111_TXT_HIMA08\\S0610'
    fn=os.path.join(dd,ch,a.strftime('%Y%m%d'),a.strftime(ch+'_%Y%
   m%d_%H%M.csv'))
    df = pd.read_csv(fn,header=None)
    df = df.set_index([0,1])
    df = df[2].to_frame(ch)
    return df

def plot_png(a,img):
    fig, ax = plt.subplots(figsize=(8,6))
    ax.pcolor(img,cmap='bwr')
    judul = a.strftime('%Y%m%d_%H%M')
    plt.title(judul)
    fout = os.path.join('..\\output_png',judul+'.png')
    fig.savefig(fout,bbox_inches='tight')
    plt.close(fig)
    return

def main():
    fn = os.path.join('..\\input_txt','arrival_result_02.csv')
    df = pd.read_csv(fn)
    dt = pd.to_datetime(df['BPL'],format='%Y-%m-%d %H:%M:%S')
    print len(dt)
    for a in dt[0:]:
        df = get_vis_Bxx(a,ch='B03')
        img = df2array(df)
        hoge = plot_png(a,img)

    return
```

```
45
46 if __name__ == '__main__':
47     main()
```

Listing A.4: Code to check B03 cloud appearence in SBD cases

A.5 Obtaining levelset

The following code is to obtain the levelset array:

```
# -*- coding: utf-8 -*-

#--morphsnakes part--
#------------------------------start
    --------------------------------
from itertools import cycle
import numpy as np
from scipy import ndimage
from scipy.ndimage import binary_dilation, binary_erosion, \
                          gaussian_filter,
    gaussian_gradient_magnitude

class fcycle(object):
    def __init__(self, iterable):
        """Call functions from the iterable each time it is called
    ."""
        self.funcs = cycle(iterable)
    def __call__(self, *args, **kwargs):
        f = next(self.funcs)
        return f(*args, **kwargs)

# SI and IS operators for 2D.
_P2 = [np.eye(3), np.array([[0,1,0]]*3), np.flipud(np.eye(3)), np.
    rot90([[0,1,0]]*3)]

_aux = np.zeros((0))
def SI(u):
    """SI operator."""
    global _aux
    if np.ndim(u) == 2:
        P = _P2
    elif np.ndim(u) == 3:
        P = _P3
    else:
        raise ValueError("u has an invalid number of dimensions (
    should be 2 or 3)")
    if u.shape != _aux.shape[1:]:
        _aux = np.zeros((len(P),) + u.shape)
    for _aux_i, P_i in zip(_aux, P):
        _aux_i[:] = binary_erosion(u, P_i)
    return _aux.max(0)

def IS(u):
    """IS operator."""
    global _aux
```

```
    if np.ndim(u) == 2:
        P = _P2
    elif np.ndim(u) == 3:
        P = _P3
    else:
        raise ValueError("u has an invalid number of dimensions (should be 2 or 3)")
    if u.shape != _aux.shape[1:]:
        _aux = np.zeros((len(P),) + u.shape)
    for _aux_i, P_i in zip(_aux, P):
        _aux_i[:] = binary_dilation(u, P_i)
    return _aux.min(0)

# SIoIS operator.
SIoIS = lambda u: SI(IS(u))
ISoSI = lambda u: IS(SI(u))
curvop = fcycle([SIoIS, ISoSI])

class MorphACWE(object):
    """Morphological ACWE based on the Chan-Vese energy functional."""
    def __init__(self, levelset, data, smoothing=1, lambda1=1, lambda2=1):
        self.levelset = levelset
        self.smoothing = smoothing
        self.lambda1 = lambda1
        self.lambda2 = lambda2
        self.data = data

    def set_levelset(self, u):
        self._u = np.double(u)
        self._u[u>0] = 1
        self._u[u<=0] = 0

    levelset = property(lambda self: self._u,
                        set_levelset,
                        doc="The level set embedding function (u).")

    def step(self):
        """Perform a single step of the morphological Chan-Vese evolution."""
        # Assign attributes to local variables for convenience.
        u = self._u

        if u is None:
            raise ValueError("the levelset function is not set (use set_levelset)")

```

```
        data = self.data

        # Determine c0 and c1.
        inside = u>0
        outside = u<=0
        c0 = data[outside].sum() / float(outside.sum())
        c1 = data[inside].sum() / float(inside.sum())

        # Image attachment.
        dres = np.array(np.gradient(u))
        abs_dres = np.abs(dres).sum(0)
        #aux = abs_dres * (c0 - c1) * (c0 + c1 - 2*data)
        aux = abs_dres * (self.lambda1*(data - c1)**2 - self.
    lambda2*(data - c0)**2)

        res = np.copy(u)
        res[aux < 0] = 1
        res[aux > 0] = 0

        # Smoothing.
        for i in range(self.smoothing):
            res = curvop(res)

        self._u = res

    def run(self, iterations):
        """Run several iterations of the morphological Chan-Vese
    method."""
        for i in range(iterations):
            self.step()


def evolve_visual(a,mask, msnake, levelset=None, num_iters=20,
    background=None):
    import matplotlib.pyplot as plt
    plt.rcParams.update({'font.size': 22})

    ik,jk = 159,96
    ib, jb = 159, 118

    if levelset is not None:
        msnake.levelset = levelset

    # Prepare the visual environment.
    fig = plt.figure(figsize=(16,8))
    fig.clf()
    ax1 = fig.add_subplot(1,2,1)
    if background is None:
        img = np.flipud(msnake.data)
```

```
130         p=ax1.imshow(img, cmap=plt.cm.gray)
131         ax1.plot(ik, jk,'gx')
132         ax1.plot(ib, jb,'bx')
133     else:
134         p =ax1.imshow(background, cmap=plt.cm.gray)
135     ax1.contour(msnake.levelset, [0.5], colors='r')
136     ax2 = fig.add_subplot(1,2,2)
137     ax_u = ax2.imshow(msnake.levelset)
138     ax2.plot(ik, jk,'gx')
139     ax2.plot(ib, jb,'bx')
140     #plt.pause(0.0001)
141 
142     judul = a.strftime('%Y%m%d_%H%M')
143 
144     # Iterate.
145     for i in range(num_iters):
146         # Evolve.
147         msnake.step()
148         # Update figure.
149         del ax1.collections[0]
150         msnake.levelset[mask] = 1
151         img = np.flipud(msnake.levelset)
152         ax1.contour(img, [0.5], colors='r')
153         ax_u = ax2.imshow(img)
154         judul_hoge = judul+'_n='+str(i+1).zfill(3)
155         ax1.set_title(judul_hoge)
156         ax2.set_title('levelset_n='+str(i+1).zfill(3))
157         #plt.pause(0.0001)
158         fout = '..\\'+judul_hoge+'.png'
159         fig.savefig(fout,bbox_inches='tight')
160 
161     #fout = '..\\'+judul+'.png'
162     #fig.savefig(fout,bbox_inches='tight')
163     plt.close(fig)
164 
165     # Return the last levelset.
166     return msnake.levelset
167 
168 #--------------------------------end
    ---------------------------------
169 import pandas as pd
170 import datetime
171 import os
172 import matplotlib.pyplot as plt
173 from scipy import interpolate
174 
175 dd='D:\\111_TXT_HIMA08\\S0610'
176 
177 def get_vis_Bxx(a,ch):
```

```
178     fn=os.path.join(dd,ch,a.strftime('%Y%m%d'),a.strftime(ch+'_%Y%
    m%d_%H%M.csv'))
179     df = pd.read_csv(fn,header=None)
180     df = df.set_index([0,1])
181     df = df[2].to_frame('ref')
182     return df
183 
184 def df2array(df):
185     df = df.unstack().transpose()
186     img = df.as_matrix()
187     return img
188 
189 def array2df(array):
190     array = np.transpose(np.flipud(array))  #periksa harus di
    flipud atau tidak
191     df = pd.DataFrame(array)
192     df.index = df.index+1
193     df.columns = df.columns + 1
194     df = df.stack()
195     return df
196 
197 def save_levelset(a,levelset,th=0.3):
198     df = array2df(np.flipud(levelset))
199 
200     dd = a.strftime('..\\levelset_th'+str(th)+'\\%Y%m%d')
201     if not os.path.exists(dd) : os.makedirs(dd)
202     fn = os.path.join(dd,a.strftime('B03_%Y%m%d_%H%M.csv'))
203     hoge = df.to_csv(fn,index=True, header=False)
204     return
205 
206 def apply_morphsnakes(a,img_ori,n,levelset=None,th=0.3):
207     #th=0.27  #without enhance, norm_ref=0.2, with enhance=0.5
208     img = np.copy(img_ori)
209 
210     img[img<th] = 0.0
211     img[img>=th] = 1.0
212     img = ndimage.gaussian_filter(img,1)
213 
214     if levelset is None:
215         levelset = np.zeros(img.shape)
216         levelset[0:180, 0:320] = 1
217     macwe = MorphACWE(levelset,img, smoothing=3, lambda1=1,
    lambda2=3)
218 
219     mask = create_mask(img.shape)
220 
221     # Visual evolution.
222     #plt.figure()
223     #levelset = evolve_visual(a,mask, macwe, num_iters=n)
```

```
224
225     for _ in range(n):
226         macwe.step()
227         levelset = macwe.levelset
228         levelset[mask] = 1
229         macwe.set_levelset(levelset)
230     print 'levelset size:',levelset.shape
231
232     return levelset
233
234 def create_mask(shape):
235     x, y = np.mgrid[:shape[0], :shape[1]]
236     #mask = (x + y - 300) <= 0
237     mask = (y<40) | (y>200)
238     return mask
239
240 def main():
241     fn = os.path.join('..\\input_txt\\','arrival_result_02.csv')
242     df = pd.read_csv(fn)
243     dt = pd.to_datetime(df['BPL'],format='%Y-%m-%d %H:%M:%S')
244     n=150
245     for a in dt[0:]:
246         try:
247             b03 = df2array(get_vis_Bxx(a,'B03'))
248             print b03.shape
249
250             levelset = apply_morphsnakes(a,b03,n,th=0.21)
251             hoge = save_levelset(a,levelset,th=0.21)
252
253             levelset = apply_morphsnakes(a,b03,n,th=0.22)
254             hoge = save_levelset(a,levelset,th=0.22)
255
256             levelset = apply_morphsnakes(a,b03,n,th=0.23)
257             hoge = save_levelset(a,levelset,th=0.23)
258
259             levelset = apply_morphsnakes(a,b03,n,th=0.24)
260             hoge = save_levelset(a,levelset,th=0.24)
261
262             print 'was reading:',a
263         except IOError:
264             print 'tidak ada:',a
265             continue
266         except ValueError:
267             print 'value error:',a
268             continue
269
270
271 if __name__ == '__main__':
```

```
272     main()
```

Listing A.5: Code to check B03 cloud appearence in SBD cases

A.6 Calculating distance of snake

The following code is to calculate distance of snake:

```
import pandas as pd
import os
import numpy as np
import matplotlib.pyplot as plt
from mpl_toolkits.basemap import Basemap
from scipy import ndimage

plt.rcParams.update({'font.size': 22})

def sta_info(sta_name):
    sta_id = {
        'KKP':[106.846,-6.124],'CHL':[106.829,-6.181],
        'BPL':[106.835,-6.226],'TJP':[106.89,-6.13],
        'KMO':[106.85, -6.18],'CGK':[106.70,-6.14],'SRG'
    :[106.13,-6.12],
        'PBT':[106.759, -6.259],'DMG':[106.75, -6.5],
        'SRP':[106.66,-6.3]
              }
    sta_lon,sta_lat = sta_id[sta_name]
    return (sta_lon, sta_lat)

def get_Bxx(ch,a):
    dd='D:\\111_TXT_HIMA08\\S0610'
    fn=os.path.join(dd,ch,a.strftime('%Y%m%d'),a.strftime(ch+'_%Y%
    m%d_%H%M.csv'))
    df = pd.read_csv(fn,header=None)
    df = df.set_index([0,1])
    df = df[2].to_frame(ch)
    return df

def get_levelset(a):
    dd = 'D:\\00_PhD_WORKS\\01_snake_jakarta\\step03\\levelset_th0
    .3'
    fn = os.path.join(dd,a.strftime('%Y%m%d'),a.strftime('B03_%Y%m
    %d_%H%M.csv'))
    df = pd.read_csv(fn,header=None)
    df = df.set_index([0,1])
    df = df[2].to_frame('levelset')
    return df

def df2array(df):
    df = df.unstack().transpose()
    img = df.values
    return img

```

```
42 def get_distance():
43     fn = '..\\input_txt\\b03_jakarta_distance.csv'
44     df = pd.read_csv(fn,header=None)
45     df = df.set_index([0,1])
46     df.columns = ['lon','lat','d']
47     return df
48 
49 def create_mask(shape):
50     y, x = np.mgrid[:shape[0], :shape[1]]
51     x0,y0 = 158,95 #BPL: 158,95 KKP:158,117
52     mask = ((x-x0)**2 + (y-y0)**2) > 900
53     return mask
54 
55 def draw_map():
56     #lon0,lon1,lat0,lat1 = 105.9,107.4,-6.7,-5.7
57     lon0,lon1,lat0,lat1 = 106.6,107.1,-6.5,-6.
58     m = Basemap(llcrnrlon=lon0,llcrnrlat=lat0,urcrnrlon=lon1,
59                 urcrnrlat=lat1,resolution='h', projection='geos',
60                 lon_0=140.7,epsg=3395)
61     m.drawcoastlines()
62     parallels = np.arange(-90.,91.,0.1)
63     # Label the meridians and parallels
64     m.drawparallels(parallels,labels=[True,True,True,True],color='
    grey')
65     # Draw Meridians and Labels
66     meridians = np.arange(-180.,181.,0.1)
67     m.drawmeridians(meridians,labels=[True,False,False,True],color
    ='grey')
68     return m
69 
70 def plot_png(im,s,a, dmin):
71     s = np.where(s==0, np.nan,s)
72     lon = df2array(get_distance()['lon'])
73     lat = df2array(get_distance()['lat'])
74 
75     mask = create_mask(im.shape)
76     im[mask] = np.nan
77     s[mask] = np.nan
78 
79     fig,ax = plt.subplots(figsize=(12,10))
80     im = np.where(im<0.3, np.nan,im)
81     m = draw_map()
82     lons,lats = m(lon,lat)
83 
84     m.pcolor(lons,lats,im,cmap='rainbow',vmin=0.3,vmax=1)
85     m.pcolor(lons,lats,s,color='r')
86 
87     sta_lon, sta_lat = sta_info('KKP')
88     x,y = m(sta_lon,sta_lat)
```

```
89      m.plot(x,y,color='k',marker='*',markersize=20,alpha=0.6)
90      sta_lon, sta_lat = sta_info('BPL')
91      x,y = m(sta_lon,sta_lat)
92      m.plot(x,y,color='k',marker='*',markersize=20,alpha=0.6)
93
94      judul = a.strftime('%Y%m%d_%H%M')
95      ax.set_title(judul+'_(d:{:.2f}km)'.format(dmin))
96      fout = os.path.join('..\\',judul+'.png')
97      fig.savefig(fout,bbox_inches='tight')
98      plt.close(fig)
99      return
100
101 def calc_distance(s,sta='BPL'):
102     import geopy.distance
103     lon = df2array(get_distance()['lon'])
104     lat = df2array(get_distance()['lat'])
105     sta_lon, sta_lat = sta_info(sta)
106     mask = create_mask(s.shape)
107     s[mask] = 0
108     idx = np.nonzero(s)
109     print len(idx[0]),len(idx[1])
110     ds = []
111     for i in xrange(len(idx[0])):
112         iy,ix = idx[0][i],idx[1][i]
113         coor1 = (lat[iy,ix], lon[iy, ix])
114         coor2 = (sta_lat, sta_lon)
115         d = geopy.distance.vincenty(coor1, coor2).km
116         ds.append(d)
117
118     dmin = np.min(ds)
119     return dmin
120
121 def get_contour(im,levelset):
122     levelset = clear_small_cluster(levelset)
123     cs = plt.contour(levelset,[0],cmap='rainbow')
124     lines = []
125     for line in cs.collections[0].get_paths():
126         lines.append(line.vertices)
127     x_line, y_line = lines[0][:,0], lines[0][:,1]
128
129     im = np.where(im<0.3,0,1)
130     s = np.zeros(shape=im.shape)
131     k = np.ones((9,9))
132     hoge = ndimage.convolve(im,k)
133     for i in xrange(len(x_line)):
134         ix,iy = x_line[i].astype(np.int), y_line[i].astype(np.int)
135         s[iy,ix] = hoge[iy,ix]
136
137     s = np.where(s==0,0,1)
```

```
138     ss = array2df(s).to_frame('snake')
139     land = get_land()
140     ss['lon'] = land['lon']
141     ss['lat'] = land['lat']
142     ss = cut_boxed_df(ss,'snake')
143     ss = ss['boxed']
144     return ss
145 
146 def array2df(array):
147     array = np.transpose(array)
148     df = pd.DataFrame(array)
149     df.index = df.index+1
150     df.columns = df.columns + 1
151     df = df.stack()
152     return df
153 
154 def cut_boxed_df(df,par):
155     lat0,lat1,lon0,lon1 = -6.6,-5.9,106.1,107.5
156     df['boxed'] = df[par]
157     df['boxed'] = np.where(df['lat']<lat0,0,df['boxed'])
158     df['boxed'] = np.where(df['lat']>lat1,0,df['boxed'])
159     df['boxed'] = np.where(df['lon']<lon0,0,df['boxed'])
160     df['boxed'] = np.where(df['lon']>lon1,0,df['boxed'])
161     return df
162 
163 def get_land():
164     fn = '..\\input_txt\\b03_jakarta_landmask.csv'
165     df = pd.read_csv(fn,header=None)
166     df = df.set_index([0,1])
167     df.columns = ['lon','lat','flag']
168     return df
169 
170 def clear_small_cluster(img):
171     blobs = img == 1
172     labels, nlabels = ndimage.label(blobs)
173     areas = np.array(ndimage.sum(blobs, labels, np.arange(labels.
    max()+1)))
174     mask = areas < 1000
175     remove_small = mask[labels.ravel()].reshape(labels.shape)
176     img[remove_small]=0.0
177     return img
178 
179 def main():
180     fn = os.path.join('..\\input_txt\\','arrival_result_02.csv')
181     df = pd.read_csv(fn)
182     sta_name = 'BPL'
183     dt = pd.to_datetime(df[sta_name],format='%Y-%m-%d %H:%M:%S')
184     rows = []
185     for a in dt[0:]:
```

```
186         try:
187             print a
188             im = df2array(get_Bxx('B03',a)['B03'])
189             levelset = df2array(get_levelset(a)['levelset'])
190             s = df2array(get_contour(im,levelset))
191             dmin = calc_distance(s,sta=sta_name)
192             #hoge = plot_png(im,s,a,dmin)
193             row = a, np.round(dmin,2)
194             rows.append(row)
195         except IndexError:
196             row = a, 999.
197             rows.append(row)
198         except ValueError:
199             row = a, 999.
200             rows.append(row)
201         except IOError:
202             row = a, 999.
203             rows.append(row)
204 
205     df = pd.DataFrame(data=rows,columns=['date','dmin'])
206     hoge = df.to_csv('dist_th0.3_'+sta_name+'.csv',index=None,
    header=True)
207     return
208 
209 if __name__ == '__main__':
210     main()
```

Listing A.6: Code to check B03 cloud appearence in SBD cases

Table A.1: Sea breeze arrival time (Jakarta).

	date	KKP	BPL
1	2017-07-17	2017-07-17 10:50:00	2017-07-17 12:10:00
2	2017-07-19	2017-07-19 10:00:00	2017-07-19 12:00:00
3	2017-07-21	2017-07-21 10:10:00	2017-07-21 13:00:00
4	2017-07-25	2017-07-25 10:30:00	2017-07-25 13:40:00
5	2017-07-27	2017-07-27 10:10:00	2017-07-27 12:30:00
6	2017-07-28	2017-07-28 11:40:00	2017-07-28 13:00:00
7	2017-08-01	2017-08-01 14:20:00	2017-08-01 15:00:00
8	2017-08-03	2017-08-03 10:20:00	2017-08-03 12:30:00
9	2017-08-05	2017-08-05 09:40:00	2017-08-05 12:00:00
10	2017-08-06	2017-08-06 09:10:00	2017-08-06 15:30:00
11	2017-08-08	2017-08-08 10:30:00	2017-08-08 12:00:00
12	2017-08-09	2017-08-09 10:30:00	2017-08-09 12:40:00
13	2017-08-11	2017-08-11 09:20:00	2017-08-11 11:50:00
14	2017-08-15	2017-08-15 10:10:00	2017-08-15 12:10:00
15	2017-08-16	2017-08-16 10:30:00	2017-08-16 13:40:00
16	2017-08-17	2017-08-17 09:30:00	2017-08-17 11:30:00
17	2017-08-29	2017-08-29 09:20:00	2017-08-29 10:30:00
18	2017-08-30	2017-08-30 10:50:00	2017-08-30 11:20:00
19	2017-08-31	2017-08-31 10:20:00	2017-08-31 12:00:00
20	2017-09-01	2017-09-01 10:50:00	2017-09-01 13:00:00
21	2017-09-02	2017-09-02 12:20:00	2017-09-02 14:20:00
22	2017-09-04	2017-09-04 10:20:00	2017-09-04 12:00:00
23	2017-09-09	2017-09-09 09:00:00	2017-09-09 12:10:00
24	2017-09-10	2017-09-10 09:20:00	2017-09-10 12:40:00
25	2017-09-13	2017-09-13 09:10:00	2017-09-13 11:10:00
26	2017-09-15	2017-09-15 09:10:00	2017-09-15 11:20:00
27	2017-09-19	2017-09-19 13:30:00	2017-09-19 14:30:00
28	2017-09-20	2017-09-20 10:10:00	2017-09-20 13:50:00
29	2017-09-22	2017-09-22 10:10:00	2017-09-22 12:50:00
30	2017-09-23	2017-09-23 10:00:00	2017-09-23 11:40:00
31	2017-09-24	2017-09-24 09:10:00	2017-09-24 10:10:00
32	2017-09-25	2017-09-25 12:30:00	2017-09-25 13:30:00
33	2017-09-29	2017-09-29 11:40:00	2017-09-29 14:50:00
34	2017-09-30	2017-09-30 09:10:00	2017-09-30 11:40:00
35	2018-07-01	2018-07-01 12:00:00	2018-07-01 12:00:00
36	2018-07-04	2018-07-04 10:00:00	2018-07-04 12:50:00

37	2018-07-06	2018-07-06 10:30:00	2018-07-06 15:00:00
38	2018-07-08	2018-07-08 11:40:00	2018-07-08 13:30:00
39	2018-07-09	2018-07-09 10:50:00	2018-07-09 13:00:00
40	2018-07-13	2018-07-13 09:20:00	2018-07-13 12:30:00
41	2018-07-16	2018-07-16 09:50:00	2018-07-16 11:40:00
42	2018-07-21	2018-07-21 09:50:00	2018-07-21 14:20:00
43	2018-07-22	2018-07-22 11:30:00	2018-07-22 12:30:00
44	2018-07-23	2018-07-23 09:20:00	2018-07-23 11:30:00
45	2018-07-24	2018-07-24 09:00:00	2018-07-24 12:00:00
46	2018-07-25	2018-07-25 10:20:00	2018-07-25 12:20:00
47	2018-07-26	2018-07-26 11:30:00	2018-07-26 13:20:00
48	2018-07-28	2018-07-28 10:00:00	2018-07-28 12:20:00
49	2018-07-30	2018-07-30 09:50:00	2018-07-30 11:10:00
50	2018-07-31	2018-07-31 10:30:00	2018-07-31 12:50:00
51	2018-08-05	2018-08-05 10:40:00	2018-08-05 13:00:00
52	2018-08-06	2018-08-06 10:40:00	2018-08-06 13:20:00
53	2018-08-07	2018-08-07 11:40:00	2018-08-07 14:40:00
54	2018-08-09	2018-08-09 09:50:00	2018-08-09 11:20:00
55	2018-08-10	2018-08-10 09:10:00	2018-08-10 12:20:00
56	2018-08-12	2018-08-12 09:20:00	2018-08-12 12:40:00
57	2018-08-13	2018-08-13 11:30:00	2018-08-13 14:00:00
58	2018-08-14	2018-08-14 11:50:00	2018-08-14 13:50:00
59	2018-08-16	2018-08-16 09:50:00	2018-08-16 12:10:00
60	2018-08-17	2018-08-17 09:20:00	2018-08-17 11:20:00
61	2018-08-29	2018-08-29 11:10:00	2018-08-29 12:30:00
62	2018-09-01	2018-09-01 10:40:00	2018-09-01 12:40:00
63	2018-09-02	2018-09-02 10:10:00	2018-09-02 11:20:00
64	2018-09-04	2018-09-04 11:20:00	2018-09-04 13:00:00
65	2018-09-08	2018-09-08 09:10:00	2018-09-08 15:20:00
66	2018-09-12	2018-09-12 09:30:00	2018-09-12 12:00:00
67	2018-09-13	2018-09-13 09:30:00	2018-09-13 11:00:00
68	2018-09-14	2018-09-14 10:40:00	2018-09-14 12:30:00
69	2018-09-22	2018-09-22 10:00:00	2018-09-22 11:40:00
70	2018-09-23	2018-09-23 09:10:00	2018-09-23 10:00:00
71	2018-09-24	2018-09-24 10:10:00	2018-09-24 14:10:00
72	2018-09-27	2018-09-27 09:00:00	2018-09-27 11:20:00
73	2018-09-29	2018-09-29 09:20:00	2018-09-29 12:40:00
74	2018-09-30	2018-09-30 10:50:00	2018-09-30 13:50:00